A DIRECT SEARCH FOR DARK MATTER WITH THE MAJORANA DEMONSTRATOR

Kristopher Reidar Vorren

A dissertation submitted to the faculty at the University of North Carolina at Chapel Hill in partial fulfillment of the requirements for the degree of Doctor of Philosophy in the Department of Physics.

Chapel Hill
2017

Approved by:

Reyco Henning

Chris Clemens

Jonathan Engel

Christian Iliadis

John F. Wilkerson

ABSTRACT

Kristopher Reidar Vorren: A Direct Search for Dark Matter with the Majorana Demonstrator
(Under the direction of Reyco Henning)

The Majorana Demonstrator is a neutrinoless double-beta decay experiment currently operating 4850 ft underground in the Sanford Underground Research Facility in Lead, SD. Sub-keV thresholds and excellent low-energy resolution are features of the p-type point-contact high-purity germanium detectors deployed by Majorana, making them ideal for use in direct dark matter searches when combined with Majorana's ultra-low backgrounds. An analysis of data from a 2015 commissioning run of the Demonstrator with 478 kg d of exposure was performed to search for mono-energetic lines in the detectors' energy-spectrum from bosonic dark matter absorption. No dark matter signature was found in the 5-100 keV range, and upper limits were placed on dark bosonic pseudoscalar and vector-electric couplings. The same analysis produced null results and upper limits for three additional rare-event searches: Pauli-Exclusion Principle violating decay, solar axions, and electron decay. Improvements made to Majorana since commissioning will result in increased sensitivity to rare-event searches in future analyses.

ACKNOWLEDGEMENTS

The work presented here was only possible because of the support provided by so many people over the last several years. My gratitude is not limited to those specifically acknowledged here–there are simply too many people that deserve thanks.

I want to first thank everyone on the MAJORANA collaboration. Despite the great stress that comes along with doing good science, the collaboration stayed focused and achieved significant milestones over the last several years. It has been a great pleasure to work with everyone involved, even when that work took place in a cleanroom, one mile underground. This dissertation would never have been written without the overwhelming support from my collaborators.

I am grateful to have been a part of the UNC community and especially the Experimental Nuclear and Astroparticle Physics (ENAP) group. Special thanks goes to my advisor, Reyco Henning, who helped me navigate my way through the unending obstacles that arose throughout graduate school. I have to thank John Wilkerson who always seemed to ask the tough questions that ultimately kept me on course for graduation. The other students and the postdocs that have come and gone also deserve thanks; their support and advice was extremely helpful.

My family has my gratitude for their support throughout all my years of education. The unconditional support from my mother on any endeavor has been invaluable. My step-dad, Chester, always impressed upon me the importance of critical thinking. The persistence and dedication of my brother Billy, who followed through on his childhood dream of becoming an airplane pilot, has been huge source of inspiration and motivation to get through school. I will never forget my dad who passed away in 2011: he was one of the most generous people I've ever known and valued education above everything. It's terribly regretful that he's not

here to read this.

Finally, to friends, extended family, all the amazing people I've met traveling for work, and everyone else: thank you. This has been a wild ride, but it's only the beginning of the beginning of the end of the beginning.

TABLE OF CONTENTS

LIST OF TABLES

LIST OF FIGURES

LIST OF ABBREVIATIONS AND SYMBOLS

$0\nu\beta\beta$	Neutrinoless Double-beta Decay
$2\nu\beta\beta$	Double-beta Decay
BEGe	Broad Energy Germanium
C.I.	Confidence Interval
CMB	Cosmic Microwave Background
DFSZ	Dine, Fischler, Srednicki, and Zhitnitsky Axion Model
DM	Dark Matter
GAT	Germanium Analysis Toolkit
HPGe	High Purity Germanium
KSVZ	Kim, Shifman, Vainstein, and Zakharov Axion Model
PDF	Probability Distribution Function
PEP	Pauli Exclusion Principle
PPC	P-type Point Contact
Q	End-point Energy
ROI	Region of Interest
SBC	Single Board Computer
SURF	Sanford Underground Research Laboratory
WIMP	Weakly Interacting Massive Particle
WMAP	Wilkinson Microwave Anisotropy Probe

CHAPTER 1: Introduction

Roughly 80% of the matter density in the universe is hypothesized to be non-baryonic 'dark matter.' While the evidence for dark matter is well-established, it's based upon indirect observation resulting from its gravitational interactions. The exact nature of dark matter remains unknown, though cosmologists tend to favor a cold, exotic, non-Standard Model particle as the dominant dark matter candidate. A direct discovery via a particle interaction would confirm its identity as a new type of particle and help elucidate its fuller complexion. Several experiments are currently attempting to directly detect dark matter interactions. This dissertation focuses on direct dark matter detection efforts with the MAJORANA DEMONSTRATOR.

Section 1.1: The Case for Dark Matter

The concept of dark matter is neither neither new nor astounding. In its earliest usage, 'dark matter' referred to any mass whose existence had been inferred, yet remained undetected by (traditionally optical) observation or experimentation. Examples included cold, non-luminous objects such as dead stars, planets, or clouds of gas. Towards the latter half of the 20^{th} century–as the field of astroparticle physics emerged–the term dark matter became more synonymous with exotic, extra-Standard Model mass. Since then, direct detection of particle dark matter has become an active field of research and the main focus of multiple experiments. While the constitution of dark matter is the subject of much debate, it's existence is well-established by virtue of the multitude of indirect evidence.

Isaac Newton's laws of motion and universal gravitation have provided a strong foundation for astronomers to study the mechanics of celestial bodies. Historically, examination

of gravitationally anomalous motion often provided clues of unobserved objects, leading to important discoveries in astrophysics. Notable examples include the discovery of a companion star orbiting Sirius (known as 'Sirius B') and the discovery of Neptune [1]. Almost two decades before Alvan Graham Clark first observed Sirius B, Friedrich Bessel deduced its presence based on its irregular motion, claiming that such motion would not be surprising if it were a double star system [2]. Similarly, John Galle first observed Neptune after Urbain Le Verrier precisely predicted its location based on observations of Uranus [3]. Historical examples like these coupled with modern observations of anomalous motion of galactic and larger scale structures motivate searches for dark matter.

To avoid being disingenuous, another case of unusual motion worthy of cognizance is the anomalous precession of Mercury's perihelion, with discovery credited to Le Verrier. The perihelion precesses roughly 43 arcseconds/century faster than predicted by Newtonian gravitational dynamics. The fast precession led astronomers to believe that a hypothetical protoplanet, named Vulcan, was perturbing the orbit. Numerous claims of the observation of Vulcan were made throughout the latter half of the 19^{th} century. With each claim, Le Verrier would attempt to correct Vulcan's orbital parameters to predict its next transit by the sun. Many in the astronomy community at the time doubted Vulcan's existence after Le Verrier's calculations did not correctly predict further sightings. The resolution to this conundrum had to wait until 1915 when Albert Einstein demonstrated that Mercury's precession could be explained within the framework of General Relativity.

The remarkable example of the extension of gravitational theory explaining away Vulcan has since motivated alternative gravity hypotheses, namely Modified Newtonian Dynamics (MOND), that compete with dark matter models. MOND theories do well to explain some phenomena that are usually attributed to dark matter, such as the flattening of galactic rotation curves, but they have compatibility issues with cosmological models such as the CMB anisotropy [4]. Alternative gravity is part of an additional paradigm of modifying foundational theories as an alternative to solving the missing mass problem and is outside

the scope of this dissertation.

The case for dark matter is built from indirect observational evidence and successful integration into the standard cosmological framework, i.e ΛCDM. Some well-known examples that lend credence to the dark matter hypothesis include:

- Unaccounted mass found via virial theorem audit
- Galaxy mass distributions inconsistent with rotational curves
- Gravitational lensing of distant galactic clusters
- X-ray observation of hot gas within clusters
- Cosmic microwave background anisotropy
- Deuterium abundance via primordial nucleosynthesis

Further discussion expanding on these considerations follows.

1.1.1: Indirect Observational Evidence

By the end of the 19^{th} century, searches for dark objects within the Milky Way were underway. Dynamical models were used as a tool to set upper limits on the amount of dark matter within the galaxy. Lord Kelvin conceptualized a uniformly dense gaseous model of stars in the galaxy with gravity acting as the inter-particle force mediator. Using variations of this model, Kelvin, Henri Poincaré, Ernst Öpik, Jacobus Kapteyn, and Jan Oort were able to estimate the total mass within the solar neighborhood, i.e. within roughly 3000 light years of the sun [1, 5–8]. Noting that the predicted velocity dispersion is similar to that of the observed matter, they concluded that the density of non-luminous matter within the neighborhood cannot exceed the luminous density.

Virial Theorem

The work of Oort and his predecessors was confined to intra-galactic volume scales. In 1933, Fritz Zwicky–one of the most cited names in the field of dark matter–published his

analysis of galaxy cluster observations made by Edwin Hubble and Milton Humason [9]. A galaxy cluster is large scale structure consisting of hundreds or thousands of galaxies that are gravitationally bound. The majority of baryonic mass in galaxy clusters is found in the intra-cluster medium, consisting of extremely hot, $\mathcal{O}(10^6$ K), gas. Zwicky particularly focused on the Coma cluster, noticing that galaxies within it exhibited large differences in velocity, upwards of 2000 km/s. With the measured velocity dispersions, he was able to apply the virial theorem to estimate the total mass of the cluster [10, 11].

The virial theorem provides an expression for the time averaged kinetic energy of a system of particles (entire galaxies in this case). If the intra-particle potential is of the form $V(r) = ar^n$, then the virial theorem can be stated as,

$$\langle T \rangle = n \langle V_{\text{tot}} \rangle \tag{1.1}$$

where T is kinetic energy, V_{tot} is the potential energy of the system, and $\langle \cdot \rangle$ denotes time averaging. Gravitation has a $1/r$ potential, so $n = -1$. Inserting the gravitational potential yields the result,

$$\sigma^2 \approx \frac{GM}{R} \tag{1.2}$$

where σ is the velocity dispersion, G is the universal gravitation constant, and M is the mass within a spherical volume of radius R.

Zwicky estimated the total mass of the Coma cluster to be the product of the roughly 1000 observed galaxies and the average galactic mass, about 10^9 $M_\odot$. The radius was estimated to be 10^6 light years, predicting a velocity dispersion of $\mathcal{O}(100$ km/s). This is roughly an order of magnitude less than the observed dispersion. From this result, Zwicky concluded that a substantial fraction of the mass in the Coma cluster was attributable to dark matter, e.g. cold stars, miscellaneous macroscopic bodies, and gas [1, 11]. Zwicky originally overestimated the amount of dark matter in the Coma cluster because of parameter uncertainties (e.g. the Hubble constant, necessary for measuring velocity dispersion) at the time. Precise

characterization of the distribution of dark matter in the Coma cluster and other galaxy clusters is ongoing [12, 13].

Galactic Rotation Curves

Galactic rotation curves describe the average rotational velocity[1] of visible objects as a function of distance from the galactic center. Typically, the center of a galaxy is its most luminous feature, motivating the conclusion that the central region encompasses a plurality of the galactic mass. From the density profile, it is possible to predict the rotational velocity of stars or gases in galaxies at varying distances. For many galaxies, the predicted rotation curves do not match the measured curves, particularly for large radii. Dark matter provides an explanation for the disparity amongst the measured and predicted galactic rotation curves.

Using a spectrogram, the rotation of a galaxy is measured by analyzing the doppler shift along its major axis. If the galaxy is rotating, light from the arm approaching the observer will be blue shifted while light from the receding arm will be red shifted. A transition signature would be noted at the galactic center. Figure 1.1 shows an example of the doppler shift for NGC 7531. Precursory spectrographic measurements of the Andromeda Galaxy (M31, NGC 224) taken in 1914 by Max Wolf and Vesto Slipher [1, 14] provided evidence of nebular rotation: a linear correlation between wavelength and position along the major axis was apparent.

Over the next few decades several additional rotational profiles for M31 were measured out to increasing distances as technology improved, e.g. [8, 16]. At the time, it was determined that the mass-to-light ratio of Andromeda agreed well with the solar-neighborhood M/L ratio. In the late 1930s, Horace Babcock [17] measured increasing rotational velocities up to distances of 1.5° from the galactic center, which suggests the existence of a large amount of mass at extreme distances. Extra mass affects the M/L ratio, but Babcock ar-

[1]For this discussion, the rotational velocity refers to the transverse orbital speed in dist/time, not the angular velocity, ang/time.

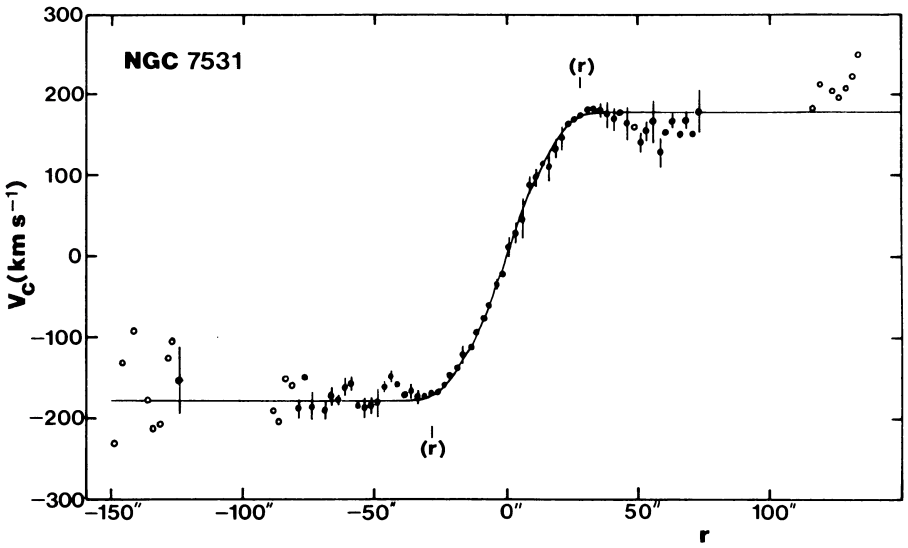

Figure 1.1: Effect of doppler shifting on the measured velocities as a function of distance (measured in arcseconds). The red shifted arm at positive angles shows above average velocities, while the blue shifted arm on the left exhibits below average velocities. Figure from [15].

gued that the ratio was biased due to intra-galactic light absorption. By the mid 1950s, larger telescopes had been deployed as the field of radio astronomy was becoming more prominent. These telescopes were capable of observing the 21 cm hydrogen-one (HI) line, facilitating an additional method of measuring galactic rotation curves that could probe very large distances. See for example, [18] and [19].

It wasn't until the 1970s that astronomers were convinced that rotation curves were alluding to the presence of large quantities of mass missing from galactic mass estimates. In 1970, Rubin and Ford [20] published their oft-cited paper that presented optical measurements of M31 rotation curves out to $\sim 2^\circ$ of arc using an image-tube spectrograph. They noted similarities between their measured rotation curves and previous M31 curves obtained from HI observations [18, 21]. It was the flattening of rotation curves far from the galactic center that was confounding to astronomers, see figures 1.1 and 1.2. By the late 1970s, many results from additional galaxies had been published with similar findings; see [1] and references therein.

Flat rotation curves are significant because they are not predicted from Keplerian orbital

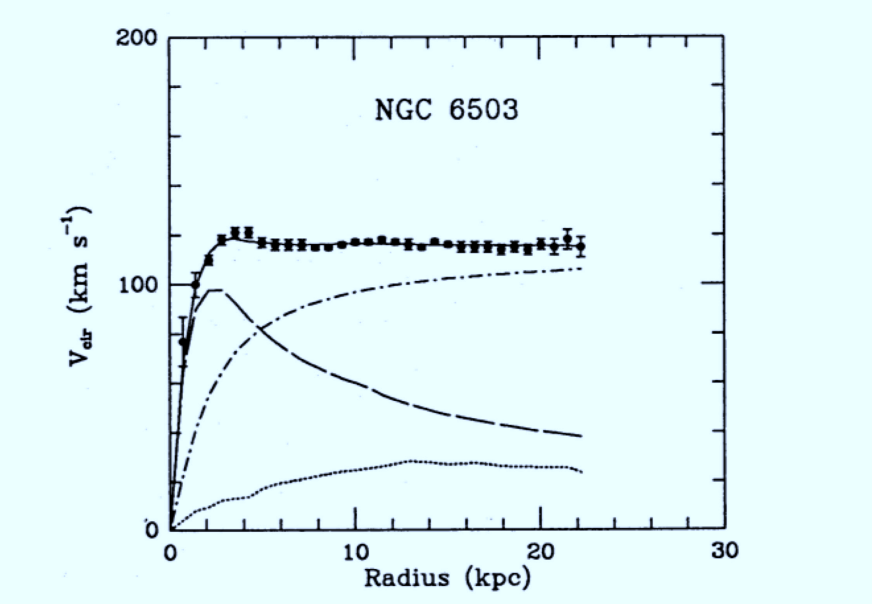

Figure 1.2: Rotation curve of NGC 6503. The dotted, dashed, and dash-dotted lines are the contributions from gas, disk (visible), and dark matter respectively. Figure from [22].

mechanics if a constant M/L ratio for the considered galaxy is assumed. At large distances, the expected rotational velocity, v, as a function of radius is roughly given by,

$$v(r) = \sqrt{\frac{GM(r)}{r}}, \tag{1.3}$$

where $M(r)$ is the total mass within a spherical radius r and G is the universal gravitational constant. From luminosity profiles, the expectation for spiral galaxies such as M31 is that most of the mass resides at the center, and so Eqn. 1.3 would predict that the velocity should fall off as $v \propto r^{-1/2}$. Rubin and Ford attempted to correct for the large quantity of hydrogen far from the center of M31, but determined that the gas only accounted for 4-8% of the mass at large radii. The non-luminous mass required to explain the flat rotation curves lays the groundwork for the 'missing mass problem.'

An example of a typical rotation curve is given in figure 1.2, showing the contribution by the mass constituents. The flattened profile curve can be explained if a dark matter halo,

with density given by the Navarro-Frenk-White profile [23], envelopes the galaxy:

$$\rho(r) = \frac{\rho_0}{\frac{r}{R_s}\left(1 + \frac{r}{R_s}\right)^2} \,. \tag{1.4}$$

Here ρ_0 is a normalization parameter, and R_s is a radial scale parameter that characterizes the halo. Note that evaluating the spherical volume integral to $\mathcal{O}(R_s)$ and dividing by the radius (as per equation 1.3) reproduces a dark matter velocity profile similar to the curve in figure 1.2. Navarro, Frenk, and White used n-body simulations to inspire the NFW profile, assuming a standard cold dark matter (CDM) cosmology. Section 1.1.2 will further discuss the ΛCDM model.

Gravitational Lensing & X-ray Observations of Galactic Clusters

Further evidence of dark matter can be inferred from gravitational lensing. General Relativity states that the presence of mass curves space-time [24], thereby altering the trajectory of nearby particles. This includes photons, meaning that nearby sources of mass can effectively refract light rays. Massive objects between an observer and a distant light source can thus produce a lensing effect. From the shear of the lensing field, it's possible to extract the distribution of the lensing mass. The effect is usually weak and typically requires that several distant sources are analyzed to determine their preferred distortion direction, from which one can determine the direction to the center of the lens. The invisible dark matter in galaxy clusters can often produce strong lensing effects that enhance the apparent ellipticity of luminous galaxies. The total mass estimate from the gravitational lens can be compared with luminous mass estimates to provide a lower limit of the dark matter content. Typical clusters are comprised of roughly 80% dark matter and 20% baryonic matter. For a comprehensive review of DM gravitational lensing see [25].

The presence of hot gas or plasma within the intra-cluster medium of galaxy clusters is yet another indicator of dark matter. Plasma temperatures are generally measured within

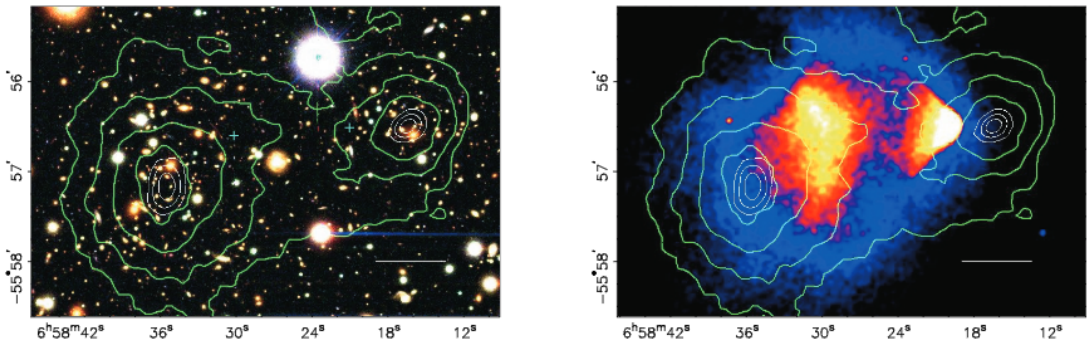

Figure 1.3: Left: Color image from the Magellan images of the merging cluster 1E 0657-558. The white bar indicates 200 kpc at the distance of the cluster. Right: Chandra x-ray image of the colliding clusters. The green contours in both panels represent weak gravitational lensing reconstructions of the distribution of mass. Figure from [28].

the 10-100 MegaKelvin range. Hot gas accounts for between 50-90% of the baryonic mass in most clusters, with larger fractions found in the more massive clusters. As hydrogen is the most abundant element in the universe, the intra-cluster plasma consists of mostly protons and electrons, however trace amounts of helium and other heavier nuclei are found in minuscule abundance. The gravitational potential due to stars and galaxies within a cluster is not strong enough to bind the hot gas to the system. Dark matter is required to ensure that the gas does not disperse away from the cluster [26]. Kravtsov and Borgani provide a review of galaxy cluster formation in [27].

Gravitational lensing and x-ray imaging of intra-cluster gas applied together provide a remarkable 'picture' of dark matter in the famous "Bullet Cluster," 1E 0657-558 [28]. The Bullet cluster formed after two smaller galaxy clusters collided and passed through one another. Figure 1.3 shows lensing measurements overlaid upon x-ray images of the cluster. The mass distribution inferred from gravitational lensing is strongly bimodal showing a significant degree of separation between the two sub clusters. X-ray observations show less separation of the two clusters' hot gas distributions. A noble, virtually non-interacting particle dark matter candidate (see section 1.2) can explain the figure. Because most of the clusters' mass consists of dark matter, the trajectory of the DM halos remained fairly constant since DM is only known to interact gravitationally. Electromagnetic interactions of the

baryonic gas particles from both clusters caused turbulence during the collision, effectively impeding the bulk momenta of the gas. The distribution of matter in the bullet cluster can be used to constrain the self interaction of dark matter particles [29, 30].

1.1.2: Cosmological Models with Dark Matter

Dark matter can explain many artifacts in models stemming from big bang cosmology [31]. The standard model of cosmology is the ΛCDM paradigm because it's the simplest model capable of accounting for observed cosmological phenomena. ΛCDM describes a universe undergoing accelerated expansion, described by a cosmological constant (Λ), and cold dark matter (CDM) [32, 33]. The standard cosmological model explains observations such as the anisotropy in the cosmic microwave background (CMB), the abundance of light elements synthesized in the nascent universe, and the formation of large scale structures, i.e galaxy distribution (discussed more in section 1.2). A dark matter component is required in each of these examples to explain their observed features. Universal expansion requires dark energy (see for example [34]), which is not discussed here.

Cosmic Microwave Background

Primordial radiation in the microwave region of the electromagnetic spectrum can be detected from all directions in the sky [35]. The cosmic microwave background (CMB) radiation is the oldest in the universe, dating back to the period of recombination[2] when the universe was roughly 380,000 years old. Prior to recombination, the temperature and the density of the early universe was much greater than it presently is. Baryonic matter existed in an opaque (blackbody) plasma state; Thompson scattering prevented photons from freely traveling through space. As the universe cooled, protons and electrons combined to form neutral atoms. The abundance of free charge in the universe dropped by many orders of

[2]The term recombination can be misleading since there were no neutral atoms prior to this epoch. The usage is historical and derives from plasma physics.

magnitude resulting in a transparent universe. This drop in the rate of photon scattering is called photon decoupling. Since decoupling, expansion of the universe (and thus photon wavelength) has cooled the CMB temperature to about 2.7 K. As the name implies, the relic CMB radiation now permeates the sky as an irreducible, highly isotropic microwave background.

Although the temperature of the CMB is mostly isotropic, well-documented $\mathcal{O}(10^{-5}$ K) thermal angular anisotropies have been measured. Since the accidental discovery of the CMB by radio astronomers Penzias and Wilson, increasingly advanced telescopes have sought to characterize the angular anisotropies. RELIKT-1 [36, 37], launched by the Soviet Union in 1983, was the first space based telescope to map the CMB. In 1989 the COBE [38, 39] satellite was launched by NASA. Both experiments reported their findings in 1992, confirming the blackbody frequency distribution and slight anisotropy of the background predicted by ΛCDM. Succeeding COBE was the WMAP [40] telescope, which provided improved angular resolution enabling the characterization of multiple peaks in the multipole power spectrum. WMAP was retired in 2010 after the launch of the current generation spacecraft, PLANCK [33, 41]. A map of the temperature anisotropy is shown in figure 1.4. The multipole power spectrum is also shown in figure 1.5.

Analyzing anisotropies in the CMB via the temperature power spectrum can help cosmologists infer important parameters such as the curvature of the universe, the expansion rate of free space, the abundance of baryonic and dark matter, and the sum of the neutrino masses. The most current cosmological parameters are fit from the PLANCK CMB survey and a subset of the parameters is shown in table 1.1.

A function including the parameters in table 1.1 is fit to the CMB power spectrum in figure 1.5. The power spectrum provides a measurement of the strength of acoustic modes in the hot plasma at the end of the recombination era, on the surface of last scattering. Gravity caused the plasma to compress while radiation pressure opposed the compression. Dark matter strengthened the gravitational compression without enhancing the radiation pressure.

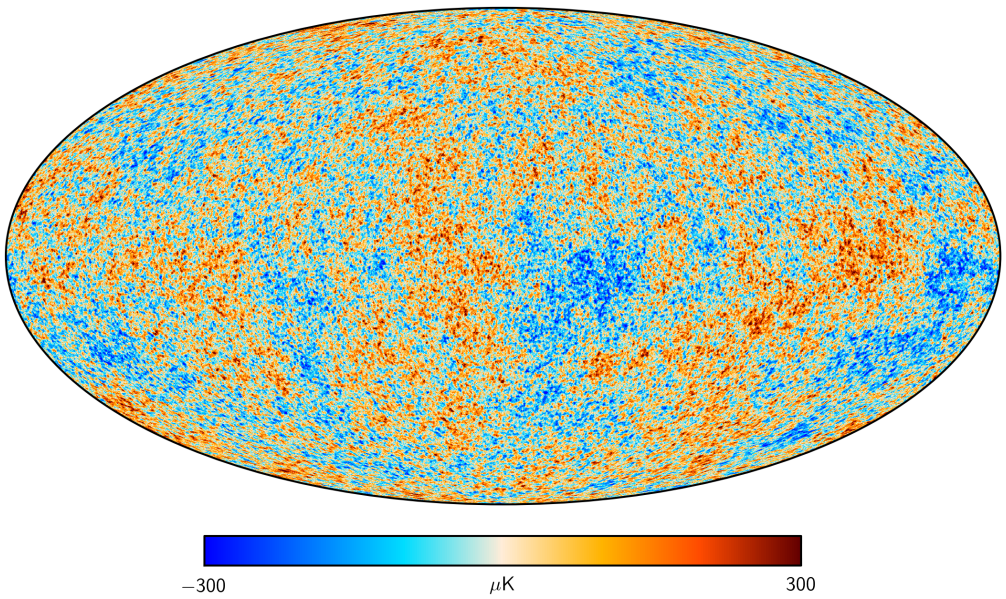

Figure 1.4: Map of the anisotropy in the cosmic microwave background. The CMB temperature is fairly uniform averaging 2.7260 K and varying by ∼600 μK. Figure from [42].

Space-time quantum fluctuations perturbed the plasma, generating acoustic oscillations. The peaks in the spectrum are the result of various phenomena: the location of the first peak in the multipole spectrum is impacted by space-time curvature, the second peak is evidence of plasma acoustics and gauges the abundance of baryonic matter. The prominence of the third peak, along with the dampening of peaks at higher multipoles, indicates the presence of non-baryonic dark (i.e electrically neutral) matter during recombination. For an accessible, qualitative overview of the CMB power spectrum by Wayne Hu, see [44].

Primordial Nucleosynthesis

The lightest metallic (i.e. not ^{1}H) isotopes in the universe were produced during primordial, or big bang nucleosynthesis (BBN). The duration of this epoch covers ∼10 s to ∼1 hour after the big bang. The abundances of ^{2}H, ^{3}He, ^{4}He, and ^{7}Li are characterized by the ratio of baryons to photons. BBN is capable of explaining the large abundance of ^{4}He in the universe, ∼25% of baryonic matter. While ^{4}He is produced in stars, stellar production cannot generate such quantities [45]. The density of light elements, determined from numerical

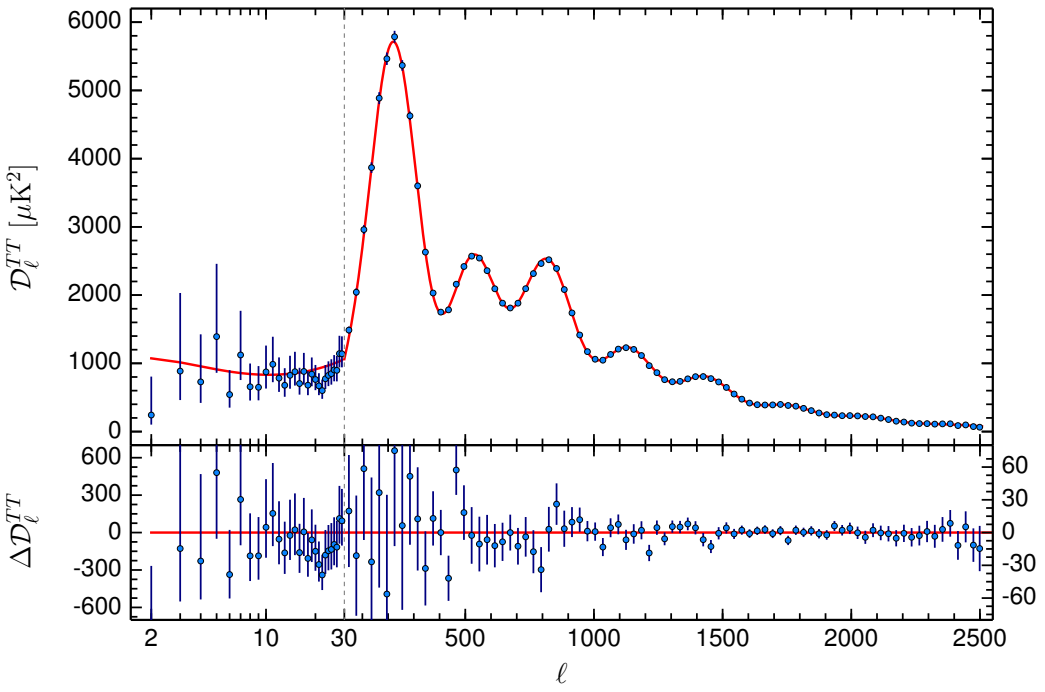

Figure 1.5: The CMB temperature power spectrum (TT). The red curve shows the best-fit when incorporating parameters from the λCDM model. Residuals are shown in the bottom plot. Error bars cover $\pm 1\sigma$ uncertainty. The parameter $\mathcal{D}_l^{TT} = l(l+1)C_l^{TT}/2\pi$, where C_l^{TT} is the expectation value of the spherical harmonic power coefficient as a function of l [43]. Figure from [33].

Table 1.1: A select list of parameters determined from the anisotropy in the CMB. Most recent values from [33].

Parameter	**Description**	**Value**	**Unc.**	**Units**
H_0	Hubble Constant	67.8	0.9	km Mpc^{-1} s^{-1}
h	Reduced Hubble Const	0.678	0.009	
Ω_m	Matter Density Parameter	0.308	0.012	
$\Omega_b h^2$	Baryonic Density	0.02226	0.00023	
$\Omega_c h^2$	DM Density	0.1186	0.0020	
$\lvert\Omega_k\rvert$	Curvature Parameter	<0.005		
Σm_ν	Sum of Neutrino Masses	<0.23		eV

simulations of BBN, constrain the baryonic matter abundance to $\Omega_b < 5\%$ of the total mass energy density of the universe, independently asserting that baryonic matter alone cannot close the universe.

The universal abundance of deuterium (^{2}H) is a direct and important validation of BBN. Deuterium is burned up in stars in proton-proton chain reactions, and is thus not a product of stellar nucleosynthesis. This implies that all deuterium is of primordial origin. Furthermore, the deuterium abundance is a measure of the efficiency of ^{4}He production during BBN [45]. Deuterium abundance is strongly anti-correlated to the baryon-to-photon ratio during nucleosynthesis. The ratio has a correspondence to the total baryon density. This independent measurement is in agreement with the baryonic abundance determined from the CMB power spectrum (table 1.1) [46, 47].

Section 1.2: Particle Dark Matter Candidates

Cosmological models suggest that dark matter is non-baryonic in nature. There are several particle dark matter candidates that have been identified in extensions of the Standard Model of Particle Physics. Four conditions generally have to be met for a particle to be considered dark matter. Clearly, a dark matter candidate must not interact with the electromagnetic force, otherwise it wouldn't be dark. It must be cold (non-relativistic) to explain the clustered galaxy distribution in the universe [48, 49]. DM must also have a lifetime that

is at least as long as the age of the universe, otherwise it would've decayed away. Since cosmological models include dark matter, the candidate particle(s) must exhibit proper relic abundance. Both thermal and athermal production mechanisms have been identified that can properly reproduce the cosmological abundance. A non-exhaustive list of some dark matter candidates (with baryonic DM) includes:

- Weakly interacting massive particles (WIMPs), section 1.2.1
- Massive compact halo objects (MACHOs) [49]
- Robust association of massive baryonic objects (RAMBOs) [50]
- Axions, section 1.2.2
- Dark pseudoscalar and vector bosons, section 1.2.3
- Primordial black holes [51]

Several groups are attempting to directly detect various DM candidates. This section will discuss WIMPs, axions, and dark bosons further. WIMPs are a popular class of thermally produced candidates that are the focus of many DM experiments. The Strong CP-problem from quantum chromodynamics (QCD) inspires the axion, described further in section 1.2.2. The main focus in this dissertation however, will be light (keV-scale) bosonic candidates, introduced in section 1.2.3.

1.2.1: Weakly Interacting Massive Particles

Weakly interacting massive particles (WIMPs) are a group of dark matter candidates that may have been produced thermally in the early universe. These electrically neutral particles are hypothesized to interact weakly with baryonic matter, scattering off of nuclei. The lightest neutralino predicted by minimally supersymmetric Standard Model (MSSM) extensions is a favorable WIMP candidate as MSSM provides a mechanism to explain stability, i.e. the conservation of R-parity [49]. Typical WIMP searches seek particles with masses between 10 GeV and 1 TeV.

WIMPs are a well motivated dark matter candidate because of the so-called 'WIMP miracle'. The relic density of WIMPs, Ω_χ, is approximated by

$$\Omega_\chi h^2 \simeq \frac{0.1 \text{ pb}}{\langle \sigma_A v \rangle}, \tag{1.5}$$

where h is the Hubble constant divided by (100 km s^{-1} Mpc^{-1}), σ_A denotes the total WIMP annihilation cross section, v is the relative WIMP velocity and $\langle ... \rangle$ indicates thermal averaging [52]. For $\Omega_\chi \sim 0.2$ and $h \sim 0.7$, the above equation implies that σ_A is characteristic of weak-scale interactions [53]. WIMPs may be detectable via scattering off the nuclei in a detector of sufficient mass ($\sim$1 tonne) within a reasonable ($\sim$1 year) amount of time.

Eqn. 1.5 is derived from the Boltzmann equation written in terms of the particle number density n:

$$\frac{dn}{dt} + 3Hn = -\langle \sigma v \rangle (n^2 - n_{eq}^2), \tag{1.6}$$

where H is the Hubble constant and n_{eq} is the equilibrium number density [49]. The present WIMP relic density can be calculated assuming they were in thermal equilibrium with SM particles after inflation. For temperatures less than m_χ, the WIMP number density becomes exponentially (Boltzmann) supressed. The WIMPs drop out of thermal equilibrium (freeze out) once the right hand side of equation 1.6 becomes less than the expansion rate of the universe [48]. After freeze out, the WIMP density remains fairly constant, leading to Eqn. 1.5.

Directly detecting WIMPs involves searching for nuclear recoils in a detector resulting from WIMP elastic scattering. The event rate depends on the WIMP and target mass, exposure, WIMP halo density in the Milky Way galaxy, and the WIMP nuclear cross section. The spectrum for WIMP recoil was derived by Lewin and Smith [54]. The formula for the rate involves many parameters and is not given here, but the general shape is an exponential decay as energy increases. An example of the expected spectrum of spin-independent WIMP interactions in germanium detectors is shown in figure 1.6. This plot was generated using

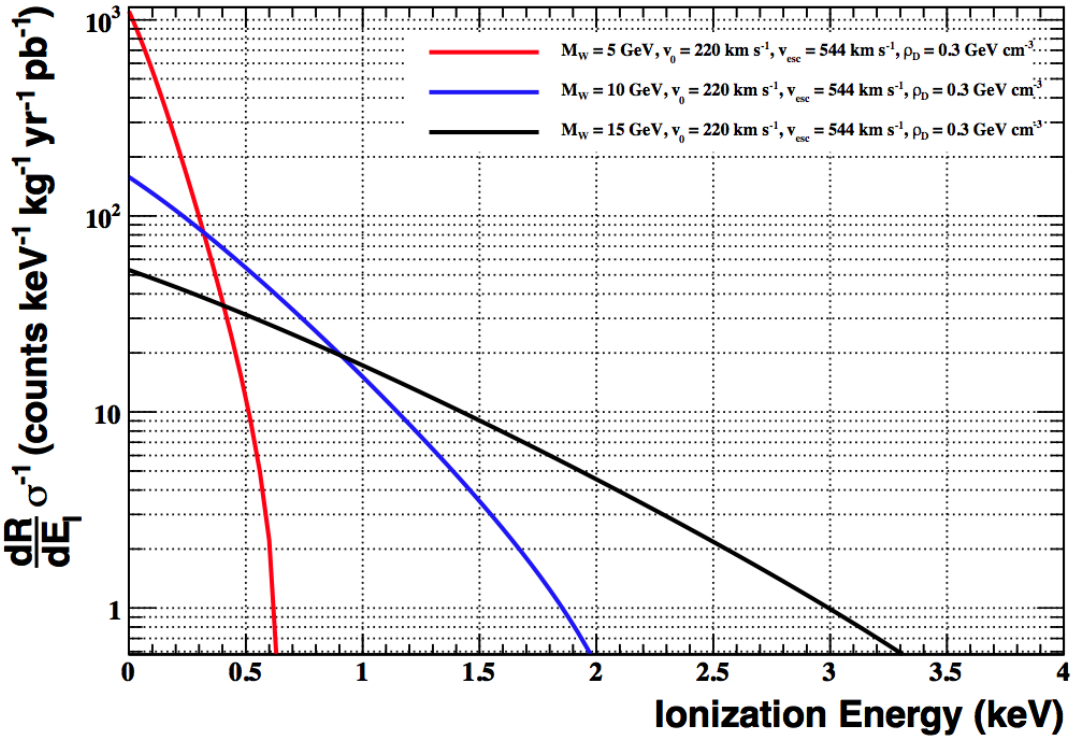

Figure 1.6: Expected WIMP spectrum for WIMPs of varying masses. Figure from [53].

pyWIMP, a tool developed by Mike Marino [52, 55].

The WIMP-nuclear cross section and WIMP mass are the two unknown quantities in the rate derived by Lewin and Smith. When showing their results from a direct search, many experiments choose to present an exclusion plot based on the upper limit of the cross section as a function of mass. A comparison of the WIMP exclusion limits from different experiments is shown in figure 1.7. Regions above the experimental limit are excluded, while regions below are inconclusive. Experiments may soon reach the coherent neutrino scattering limit, which would be an irreducible background in WIMP DM experiments.

1.2.2: Axions

The axion is a hypothetical pseudoscalar particle, resulting from a proposed solution to the strong CP problem in quantum chromodynamics (QCD). Cosmological constraints have limited their mass to between 10^{-7} and 10^{-3} eV while astrophysical constraints limit

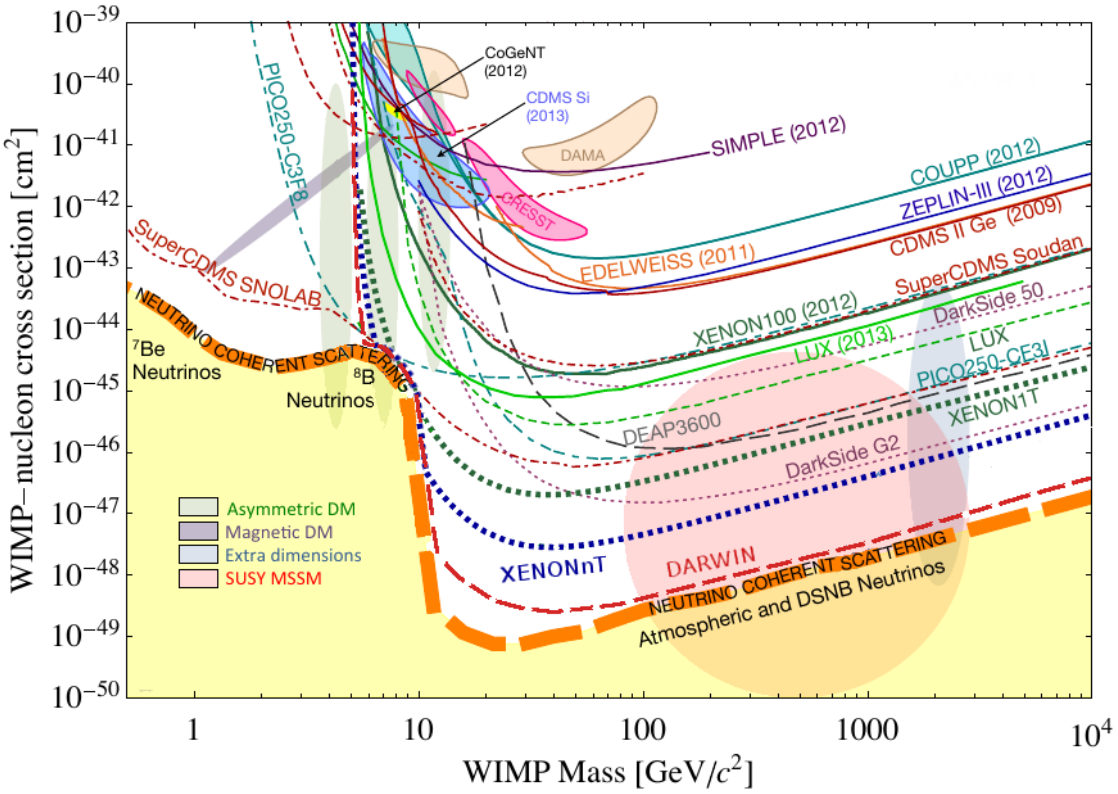

Figure 1.7: Exclusion curves generated from different experiments. Solid lines are reported limits, dashed lines are projected limits. The blobs represent unexplained excesses of events reported by experiments in the respective parameter spaces. Figure from [56]. Below the orange dashed line the spectrum due to coherent neutrino scattering is expected to dominate.

their coupling to ordinary matter, though large uncertainties remain [57]. Their theoretical foundation, long-lifetime (implied from their small mass), and their limited interactions with ordinary matter make them a popular dark matter candidate.

Quantum chromodynamics is the theory that describes the strong force, the fundamental force that binds atomic nuclei together. The theory describes interactions between quarks–the sub-hadronic particles that form either baryons or mesons–and gluons, the mediator of the strong force. In its most compact form, the QCD Lagrangian is given by [48]:

$$\mathcal{L}_{\text{QCD}} = \bar{\psi}(i\not{D} - m)\psi - \frac{1}{4}G^{\mu\nu a}G_{\mu\nu a} \tag{1.7}$$

where $\not{D}$ is the covariant Feynmann derivative associated with the gluon gauge potential, ψ is a quark spinor field, and $G^{\mu\nu a}$ is the antisymmetric QCD field strength tensor, analogous to the gauge invariant electromagnetic field tensor that describes EM fields in Minkowski space. The index $a \in \{1, ..., 8\}$ accounts for the eight different possible gluons.

Symmetries play an important role in field theories in general. For example, weak interactions maximally violate parity symmetry. Additionally, charge-parity (CP) violation has been measured in the weak sector. Notable cases include neutral kaon oscillation and the decay of $B,\ \bar{B}$ mesons [58, 59]. CP violation in the weak sector naturally leads to the question of whether CP-symmetry is violated in QCD. Experimental results place strict constraints on CP violation in the QCD sector [60]. For example, the measured upper bound on the neutron electric dipole moment, d_n has been measured to $|d_n| < 2.9 \times 10^{-26} e$ cm, see [61] and references therein. The absence of CP violation in QCD is known as the strong CP problem.

The CP violating term, $\bar{\Theta}$, is encapsulated within the QCD field strength tensor. Expanding the second term in the QCD Lagrangian exposes the CP violating angle [48]:

$$\mathcal{L}_{\text{QCD}} \supset \bar{\Theta}\frac{\alpha_s}{8\pi}G^{\mu\nu a}\tilde{G}^{a}_{\mu\nu}\ . \tag{1.8}$$

Equation 1.8 is the form that appeared in papers by Peccei and Quinn [62, 63]. Values of $\bar{\Theta}$ are naturally expected to be $\mathcal{O}(1)$, though to agree with experimental bounds it's necessary for $\bar{\Theta} < \mathcal{O}(10^{-9})$ [60, 61]. The large discrepancy constitutes a 'fine-tuning' problem in QCD. Peccei and Quinn proposed a spontaneously broken symmetry to solve the strong-CP problem. The massive axion is the pseudo Nambu-Goldstone boson that results from the symmetry breaking. It appears in the Lagrangian as a field, ϕ_A,

$$\mathcal{L}_{\text{QCD}} \supset (\bar{\Theta} - \frac{\phi_A}{f_A})\frac{\alpha_s}{8\pi}G^{\mu\nu a}\tilde{G}^a_{\mu\nu}. \tag{1.9}$$

where f_A is the axion decay constant. It can be shown from QCD that the potential for ϕ_A is minimized when $\phi_A = f_A\bar{\Theta}$ [48], canceling the CP-violating term.

Experiments attempting to directly detect axions often rely on the axion-two-photon vertex characterized by the coupling constant $g_{A\gamma\gamma}$. Via the Primakoff effect [64, 65], photons can convert to axions, or vice-versa, in the presence of a large electric or magnetic field. A microwave cavity tuned to a frequency associated with the axion mass may detect a perturbation due to an axion field, as in ADMX [66]. Another experimental concept is the 'light shining through walls' or LSW effect. Using strong magnetic fields, a photon could convert to an axion, traverse an opaque barrier, and then be converted back to a photon and be detected. A schematic from the OSQAR [67] collaboration is shown in figure 1.8. The probability of converting a photon to an axion depends on the strength of the magnetic field, the length traveled through the field, and the photon energy. A similar approach can be used to look for solar axions. Helioscope experiments, such as CAST [68] look for axions originating from the sun that convert to x-rays in their detector.

It was originally thought that the value of f_A was related to the electroweak symmetry-breaking scale $\nu_{weak} \sim 246$ GeV, but these axion models have been excluded [69–71]. Current models explore the parameter space such that $f_A \gg \nu_{weak}$. This gives rise to a couple of different models of axions, hadronic-like and Grand Unified Theory (GUT) model axions.

The two photon vertex coupling can be expressed in the following form:

$$g_{A\gamma\gamma} = \frac{\alpha}{2\pi f_A}\left(\frac{E}{N} - \frac{2}{3}\frac{4+z}{1+z}\right) = \frac{\alpha}{2\pi}\left(\frac{E}{N} - \frac{2}{3}\frac{4+z}{1+z}\right)\frac{1+z}{z^{1/2}}\frac{m_A}{m_\pi f_\pi} \tag{1.10}$$

where α is the fine-structure constant, f_A is the axion decay constant, z is the ratio of the up quark mass to the down quark mass (m_u/m_d), m_A the axion mass, m_π is the pion mass and f_π is the pion decay constant. E and N are electromagnetic and color anomalies associated with the axial current of the axion [69]. In GUT models such as DFSZ [72, 73], $E/N = 8/3$. For hadronic, KSVZ models [74, 75], $E/N = 0$. In general, a range of values for E/N is possible. These axion models with $m_A \lesssim 10$ meV have not yet been excluded by experiment.

One can also search for more general axion-like particles, where the coupling constants and mass are not related to the Peccei-Quinn symmetry breaking scale, i.e. the mass is independent of f_A. These will models will be discussed more in section 1.2.3.

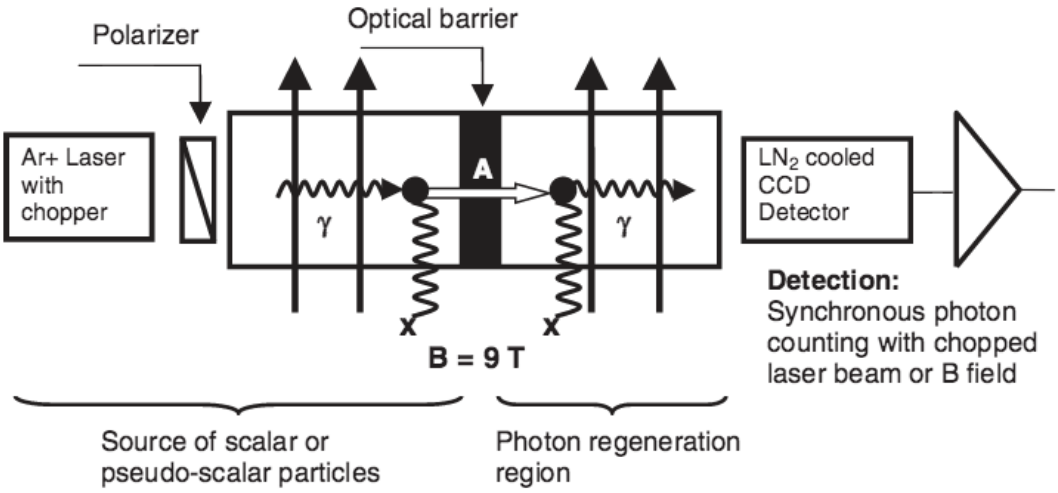

Figure 1.8: Schematic of the OSQAR light shining through wall experiment. Photons are converted to axions and then traverse the opaque barrier.

1.2.3: Bosonic keV-Scale Dark Matter

While there is a strong theoretical and cosmological basis for GeV-scale dark matter, current generation experiments have failed to detect a signal attributable to DM, see figure 1.7. Heavier dark matter models also do not fully explain gravitational clustering on both galactic and smaller scales. Bosonic light dark matter (LDM) candidates, with masses down to the keV range, provide alternative DM models that can be explored by existing neutrino and dark matter experiments [76].

DM candidates with mass at the keV-scale must have a higher number density to compensate for their low mass and a correspondingly small, or super-weak interaction cross section to explain their as-yet non-detection. Their small mass and low energy render them difficult to detect via elastic nuclear scattering, as in the case of WIMPs, demotivating searches for fermionic keV-scale candidates such as the sterile neutrino or the gravitino. In contrast, the bosonic LDM detection principle is an inelastic interaction analogous to photoelectric absorption. Assuming the particles are non-relativistic CDM candidates, a detection signal would be a peak with energy equal to the particle rest-mass. Recent LDM searches have focused on pseudoscalar and vector bosons since both existing and next-generation DM experiments could be competitive with astrophysical and cosmic gamma background constraints [76]. Figure 1.9 illustrates these constraints with possible sensitivity in Ge detectors.

For a bosonic pseudoscalar particle to be a viable keV-scale DM candidate, a couple assumptions related to coupling to the Standard Model must be made. The interaction term of the Lagrange density function looks like [76]:

$$\mathcal{L}_{\text{int}} = \frac{C_\gamma a}{f_a} F_{\mu\nu}\tilde{F}^{\mu\nu} - \frac{\partial_\mu a}{f_a}\bar{\psi}\gamma^\mu\gamma^5\psi + ... \tag{1.11}$$

with a, the pseudoscalar coupling constant, normalized by f_a. C_γ is the dimensionless coupling to photons $F_{\mu\nu}$ the electromagnetic field tensor, γ^μ are the Dirac matrices such that $\gamma^5 = i\gamma^0\gamma^1\gamma^2\gamma^3$, and ψ, $\bar{\psi}$ are dual Dirac spinors. The ellipses includes couplings to

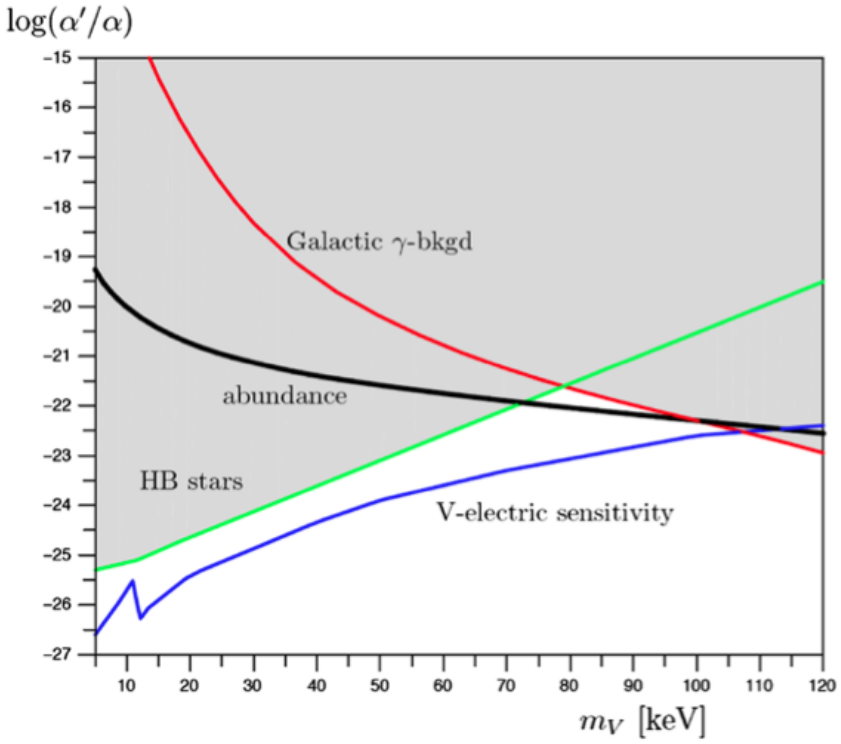

Figure 1.9: Vector bosonic dark matter exclusion plot. Blue: V-electric cross section for Ge, assuming a detector sensitivity equivalent to a 1 pb cross section for a 100 GeV WIMP. Green: constraint from He-burning lifetime in HB stars. Red: Constraint from 3γ decays. The thick black line corresponds to parameters necessary to reproduce the DM abundance thermally. Figure from [76].

other fermions and gauge bosons. The term on the left in eqn. 1.11 is related to the two photon decay channel (e.g the Primakoff effect), while the term on the right is indicative of an axioelectric coupling. For viable keV-scale pseudoscalar DM without overly restrictive constraints on f_A, we assume that the axioelectric coupling dominates while photon coupling is suppressed.

For keV-scale bosonic vector particles, the interaction Lagrange density can be written as [76]:

$$\mathcal{L}_{\text{int}} = e\kappa V_\mu \bar{\psi}\gamma_\mu\psi + ... \tag{1.12}$$

which is an elementary vector interaction. Here e is the electronic charge, κ is the vector hypercharge, and V_μ is the vector field. The product $e' = e\kappa$ is analogous to electromagnetic coupling such that $\alpha' = (e\kappa)^2/4\pi$ is similar to a vector-electric fine-structure constant. Because it is assumed that the vector mass, m_V is $\mathcal{O}$(keV) instead of sub-eV, coupling with photons is suppressed[3] [76, 77].

For experimentalists, a key difference between pseudoscalar and vector DM is their decays to photons. Since pseudoscalars are axion-like, their dominant decay mode is via the two photon decay. Vector decay into two photons is strictly forbidden. The dominant vector decay mode is to three photons. This has an impact on experimental sensitivity to bosonic DM candidates. Model dependent astrophysical constraints exclude the pseudoscalar parameter space that current experiments can probe, see for example [78, 79] and figure 6.3. For vectors, however, current experimental sensitivity is competitive with astrophysical constraints, see figure 1.9.

Bosonic scalar dark matter is not considered in this dissertation. The scalar-electric coupling term, which replaces the second term in eqn. 1.11, depends explicitly on the scalar mass. Scalar keV-scale DM thus requires highly model dependent parameters in order to be viable. Their phenomenology is also quite similar to the pseudoscalar boson.

[3]A more general form of the interaction term of the vector Lagrange density is $\mathcal{L} = \kappa V_\nu \partial_\mu F_{\mu\nu}$.

Section 1.3: Outline of Dissertation

This dissertation will focus on the sensitivity of the MajoranaDemonstrator (MJD) to bosonic dark matter candidates. Since MJD is a P-type point contact (PPC) germanium detector array experiment, chapter 2 will provide an overview of semiconductor properties and PPC Ge detectors. Chapter 3 will discuss the overall Majorana Demonstrator experiment detailing construction, design, and cleanliness requirements. These first three chapters are meant to serve as an introduction, so that the reader becomes familiar with the experimental purpose.

The latter chapters focus on the data collected with the MJD. Data collection and systematics will be discussed in chapter 4. Data cleaning and cuts will be the topic of chapter 5. Chapter 6 will discuss the data analysis and present the result of the bosonic dark matter search, along with other rare-event searches that were possible.

CHAPTER 2: Semiconductor Detectors and the P-type Point-Contact Germanium Detector

This chapter provides an overview of Germanium detectors, with extra focus on p-type point-contact (PPC) detectors. To begin, a review of detection principles in semiconductor detectors[1] is provided. The discussion will then shift to Germanium detectors, including some background on conventional detector configurations in order to lead into a discussion of PPC detectors. The remainder of the chapter will focus on PPC detectors, specifically their noise, resolution, and charge collection characteristics. The data presented in this dissertation was all acquired from the MAJORANA DEMONSTRATOR, which employs arrays of Ge PPC detectors.

Section 2.1: Properties of Semiconductor Detectors

2.1.1: Introduction

Ionizing radiation was discovered at the end of the 19^{th} century. Early discoveries were made using photographic plates, commonly used in research during that time. In 1896, Henri Becquerel–after whom the S.I. unit of radiation is named–discovered that it's possible to image certain phosphorescent materials on photographic plates even when the plates are covered by thick black paper. He concluded that invisible rays were emanating from these materials [80].

Detecting ionizing radiation with a semiconductor detector involves collecting ionized particles and/or liberated charge in a detector medium, usually by applying an electric field.

[1]These may also be referred to as solid-state detectors. While other types of detectors are technically solid-state, the term is usually reserved for semiconductor detectors in which ionizing radiation generates electron-hole pairs. The latter term will be used to avoid confusion.

Any liberated charge is collected by electrodes, hence a change in voltage or current across the electrodes indicates an ionizing event has taken place. Ideally, the response of the detector is a linear function of the incident energy deposit of the ionizing radiation.

Semiconductor detectors are widely used due to several advantages over other detectors types, such as gas-filled and scintillator detectors. Because semiconductors are made from denser and solid materials, they can more efficiently detect particles of higher energy, reducing the physical size of the detector. This includes gamma rays, for which many Ge detectors are optimized to detect. Another major advantage of semiconductor detectors is their superior energy resolution. Typically the energy resolution is limited by the statistical fluctuations in the number of charge carriers produced by incident radiation. In silicon and germanium, the energy required to create an electron-hole pair at 77 Kelvin (liquid nitrogen temperature) is 3.76 and 2.96 eV respectively [81, 82]. A typical Ge detector might have a resolution between 1-2 keV FWHM at 1173 keV (0.09-0.18%) [83], while the FWHM of a NaI scintillator detector might be roughly 60-70 keV (5-6%) [84].

2.1.2: The Band Gap Model

The periodicity of the crystalline structure of most solids provides a mechanism for explaining the conductivity of various materials by creating "band-gaps". In solids, electron energies are constrained to allowed bands, continuos intervals separated by forbidden regions, or gaps. A simplified model is shown in figure 2.1. Electrons in the lower energy valence band do not contribute to the conductivity. Thermal excitation may promote an electron from the valence band to the conduction band. In this state, the electron is unbound from the crystal lattice and is free to diffuse throughout the material. As shown in figure 2.1, the gap width in insulators is relatively large, $\gtrsim$5-10 eV, compared to semiconductors that have gap widths of $\simeq$1 eV. Assuming no thermal excitation, the valence band of insulators and semiconductors is full, and hence electrical conductivity drops to zero. For conductors such as copper, there is a partial overlap of the valence and conduction bands.

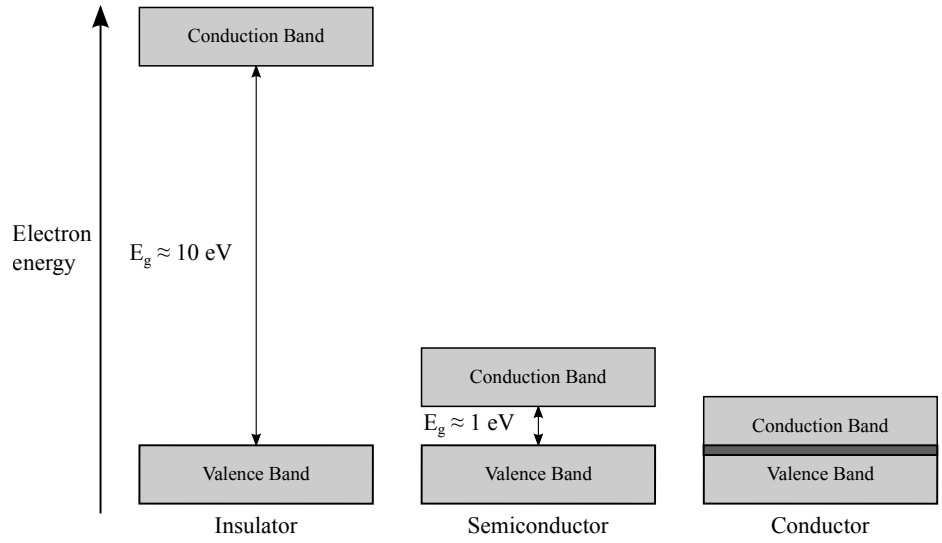

Figure 2.1: A simplified band gap model of solids. The larger energy difference between the two insulator bands (left) prevent most electrons from crossing the gap. In semiconductors (middle), thermal excitation is much more likely to excite an electron into the conduction band. For metals (right), the conduction band overlaps the valence band resulting in some excess of mobile charge. Figure from [53].

If an electron gains sufficient energy to cross the gap a net positive charged vacancy, or hole, will be left in the valence band. This effect is generally referred to as electron-hole pair creation[2]. Both the electron and the hole will drift under the influence of an electric field in opposite directions and at different drift velocities that depend on the carrier mobility, equation 2.1 [82].

$$v_h = \mu_h \mathcal{E} \qquad \text{and} \qquad v_e = \mu_e \mathcal{E} \tag{2.1}$$

where $\mathcal{E}$ is the electric field strength, v is the drift velocity, and μ is the field-dependent carrier mobility. Equation 2.1 breaks down at higher electric field strength; eventually the drift velocity reaches a saturation value, becoming independent of $\mathcal{E}$.

The probability per unit time is that an electron-hole pair will be thermally generated is

[2]In metal conductors only the flow of electrons contributes to the conductivity.

given in equation 2.2 from [82]:

$$\mathcal{P}(T) = CT^{\frac{3}{2}} \exp\left(-\frac{E_g}{2k_B T}\right) \tag{2.2}$$

where T is the temperature in Kelvin, E_g is the gap width, k_B is the Boltzmann constant ($k_B = 8.617 \times 10^{-5}$ eV/K), and C is a proportionality constant inherent to the material. If no electric field is applied, the thermally produced electron-hole pairs will eventually recombine. An equilibrium pair concentration will be established that is proportional to the production rate. In germanium detectors, this concentration is too high at room temperature (293 K) due to the small gap width (0.665 eV), resulting in higher than acceptable leakage currents. For this reason, germanium detectors are commonly operated at LN temperature to reduce the thermal pair creation [85].

2.1.3: Impurities and Dopants

In a completely pure semiconductor there are an equal number of electrons and holes at any given time. Each electron promoted to the conductance band produces a hole in the valence band. The equilibrium concentration of holes and electrons, which depends on temperature and the gap energy width, will be the same. In reality, a 100% pure, or intrinsic, semiconductor is impossible to achieve. There will always be some residual impurities in the semiconductor that affects the intrinsic conductivity of the material.

Intentionally adding impurities, or doping, a semiconductor crystal can have desirable effects on the properties of the material, including the conductivity. A pentavalent impurity, such as phosphorus or antimony, occupying a site in a tetravalent germanium or silicon crystal will introduce a surplus electron into the lattice. This type of impurity is referred to as a donor impurity. The donor electron is weakly bound at the impurity site, requiring very little energy to enter the conduction band. Since no site is available for the donor electron in the pentavalent crystal lattice, its energy level is in the intrinsic semiconductor gap region,

just below the conduction band. Similarly, a trivalent impurity, such as gallium or boron will introduce an additional acceptor site, or hole into the lattice. This manifests as an electron energy level slightly above the valence band. Figure 2.2 shows a simplified model of the effect of impurities in a semiconducting crystal.

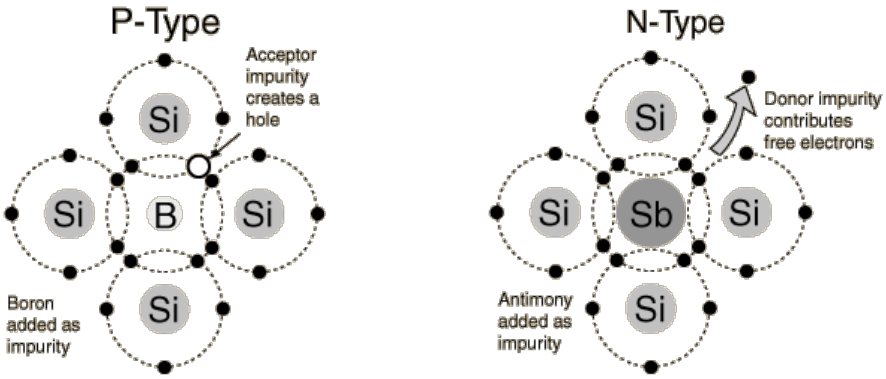

Figure 2.2: Simplified model of impurities in a silicon crystal. In the p-type material (left), an acceptor site or hole is created because of the trivalent boron impurity. The antimony impurity in the n-type material (left) contributes a donor electron that is very weakly bound to the lattice site. Figure reprinted with permission from [86].

Doped semiconductors with more donor impurities are referred to as n-type semiconductors while those with more acceptor impurities are designated as p-type. Electrons (Holes) are the majority charge carriers in n-type (p-type) materials. An impure semiconductor can be made to behave more like the intrinsic material by adding a compensating impurity of the opposite type. Heavily doped materials are often referred to with a '+' superscript, e.g. a semiconductor heavily doped with acceptor impurity is p^+-type. The importance of considering material type is examined in section 2.1.4.

2.1.4: Semiconductor Junction

If a p-type and an n-type semiconductor are thermally bound, semiconductor junction effects can be observed. The free charge carriers near the junction are able to migrate across the boundary into the opposite type. Donor electrons from the n-type material combine with holes in the p-type material (and vice-versa), effectively canceling out. The remaining

immobile space charge (ionized lattice atoms) creates an electric field that opposes the further diffusion of free charge. This region of electric field is called the depletion region. Any negative (positive) charge that forms in the depletion region, e.g from ionizing radiation, is forced towards the n-type (p-type) material. In Ge, the potential difference across this region is roughly 0.4 V [83]. See figure 2.3.

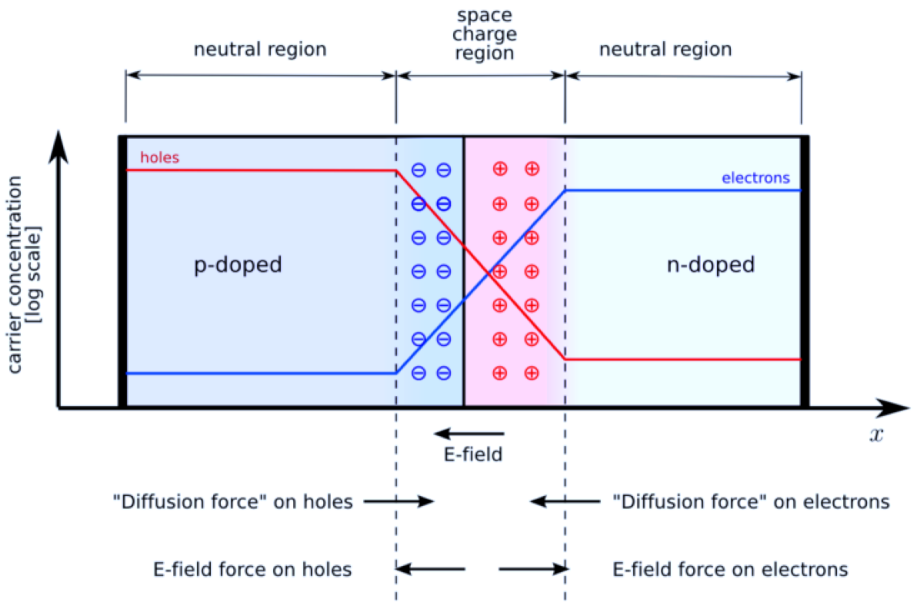

Figure 2.3: Charge distribution at the junction of opposite type semiconductors. Majority carriers from the two types each diffuse into the opposite typed material. At equilibrium, the resulting electric field opposes further diffusion, creating a depleted region (center). Figure originally uploaded by user "TheNoise" to English Wikipedia under the CreativeCommons License.

The detection principle in semiconductor detectors is based on detecting electron-hole pairs generated by ionizing radiation in the depletion region around the junction. A germanium detector, for example, might utilize the junction between a nearly intrinsic, slightly p-type material and a heavily doped n^+-type material. Initially, the depletion region is very narrow, but can be widened by applying a reverse bias voltage across the junction. A positive (negative) voltage applied to the n^+-type (p^+-type) material will attract free electrons (holes) away from the junction. This expands the region of immobile space charge, effectively widening the depletion zone. Under the assumption that the n^+-type is much more heavily

doped than the p-type material, the depletion width can be estimated as [82],

$$\begin{aligned} d &\simeq \sqrt{2\epsilon\mu\rho V}, \\ V &= V_0 + V_b. \end{aligned} \tag{2.3}$$

where d is the depletion width, ϵ is the dielectric constant ($= 12\epsilon_0$ in Ge), μ is the carrier mobility, ρ is the resistivity of the material, and V is the voltage across the junction. Here V is the sum of the intrinsic junction voltage V_0 and the applied bias voltage V_b. In practice, the bias voltage will be much larger than the junction voltage ($\sim$1000 V compared to $<$1 V). The resistivity of the material is given by [82],

$$\rho = \frac{1}{e\mu N} \tag{2.4}$$

where e is the carrier charge and N is the charge carrier density. This implies that the depletion width increases with the purity of the material. In most applications, a depletion region that spans the length of the detector ($\sim$few cm) while maintaining a reasonable bias voltage ($<$ 5000 V) is desirable. The germanium used in the production of high purity Ge detectors have measured impurity levels as low as 10^{10} atoms/cm^3 to achieve this [83].

Section 2.2: High Purity Germanium Detectors

Germanium detectors are widely used for x-ray and gamma ray detection and spectroscopy. While available silicon based detectors have a depletion thickness of a few millimeters, the depletion region in high purity germanium (HPGe) detectors can be centimeters thick. Germanium is also higher-Z than Si, making it a much more efficient gamma-ray detector per unit volume, facilitating detection of gamma rays with energies up to a few MeV. HPGe detectors have been in use since the 1980s and are commercially available [85, 87]. Their commercial availability and technological maturity have made them a popular choice for a variety of detection applications including scientific and defense research.

2.2.1: Crystal Fabrication

Detectors are fabricated from electronic-grade polycrystalline germanium–a raw material of very high purity used by the electronics industry [83]. To further purify the germanium to high-purity grade, the process of zone refining is used. An ingot of germanium is placed in a crucible and heated using radio-frequency (RF) heating coils. The portions of the ingot closest to the coils then melts, increasing the mobility of the impurities. The heating coils are slowly moved down the length of the crucible, resulting in a moving melted zone of the ingot. The impurity concentration remains highest in the melted zone. Eventually the impurities are swept to the end of the ingot, which can then be cut off. Multiple passes through the zone refining coils are usually required to reach the desired concentration. Figure 2.4 show a vertical zone refining setup.

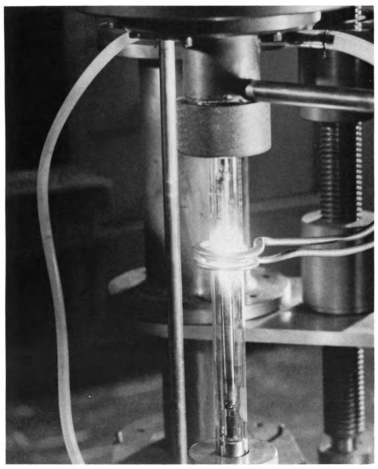

Figure 2.4: Vertical zone refining setup. The heating coil moves down the tube effectively dragging the impurities to the bottom of the crystal. Figure originally from [88], now in public domain.

After zone refining, the germanium is still polycrystalline and not yet ready for detector use. The ingot is sliced up to prepare for single crystal growth. Large single crystals are grown using the Czochralski method [89]. The purified polycrystalline material is melted inside a quartz crucible. The process takes place in an inert atmosphere such as argon or hydrogen. A specially oriented, rod mounted seed crystal is dipped into the crucible. The

seed crystal is a small piece of single crystal germanium from which the large crystal boule will grow. The size of the boule will depend on the temperature and how fast the crucible is pulled from molten germanium. The Czochralski crystal growing also serves as the final purification step in HPGe production, as impurities are removed with the excess crystal melt. Various techniques such as rotating the boule may be employed based on the experience of the crystal puller. Many of the parameters such as temperature and pull rate have to be precisely controlled by an experienced operator. For these reasons, the fine procedural details are often a commercial secret [83]. An simplified visualization outlining the process is shown in figure 2.5

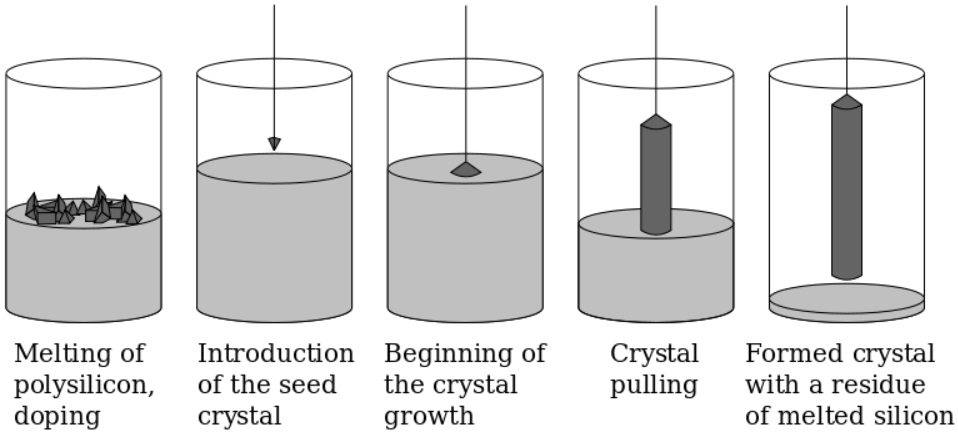

Figure 2.5: A simplified figure of the Czochralski process. The end result is a cylindrical single crystal boule. Image from wikimedia commons, entered in public domain.

Once the single crystal is prepared, the crystal must be cut into the proper detector dimensions. This is typically done with a specialized string saw to avoid damaging the surface. Hall effect measurements are used to determine the impurity concentration and type. Crystals not up to detector specification would be returned to the zone refinement stage of the process. Further modifications to the crystal shape may be made at this stage, including bulletization, i.e. the rounding of the edges of one face of the crystal. A bevel may be cut from the opposite face as well. These modifications are usually meant to improve the charge collection characteristics of the detector by eliminating regions that would have a low

electric field during detector operation [82, 83].

Finally, the n^+ and p^+ contacts on the detector must be formed. The n^+ contact on a p-type detector is made by diffusing lithium onto the surfaces. This is typically done on all surfaces with the exception of the base surface. Diffusion of lithium creates a dead-layer, a region of virtually constant electric potential in which no charge can be collected and thus no radiation can be detected. Typically this region is roughly 700 μm thick. The p^+ contact is usually made via boron implantation, and can be much thinner, $\sim$0.3 μm thick. Detectors designed for low-energy radiation detection (e.g. $\mathcal{O}$(10 keV), x-ray) will have a larger p^+ contact surface area that acts as a window for less penetrating radiations [83, 90].

2.2.2: Conventional Ge Detector Configurations

Two geometries are generally considered when configuring germanium detectors, the planar geometry and the coaxial geometry. The detector configuration has a direct effect on important detector characteristics including resolution and charge collection. For reference, a brief description of the two types is given. A simple schematic of different detector configurations is show in figure 2.6. A more in-depth overview of the P-type point contact (PPC) detector, a relatively recent configuration, can be found in section 2.3.

Planar Detectors

Planar detectors are geometrically simple. Electrical contacts are made on the flat faces of the cylindrical detector, with an n^+ contact on one face and a p^+ contact on the opposite face. By virtue of the geometry, the electric field in a planar detector is nearly independent of the radial position, depending only the distance from the blocking electrode (p^+ contact in p-type detectors, n^+ contact in n-type). Since the full depletion voltage is applied across the cylindrical face surfaces, significant surface leakage currents can be produced. Fluctuations in the leakage current are a source of electronic noise, and can have a negative impact on the detector resolution (see section 2.3.2). To mitigate these effects, a separate, narrow,

grounded, guard ring electrode can be included on the blocking contact face to minimize the current's effect on the detector signal. Planar detectors range from 3 - 70 mm in diameter and up to 3 cm in height [82, 83].

Coaxial Detectors

Coaxial detectors are the most common type of germanium detectors in use. In this configuration, the electrical contact is made on the cylindrical surface of the detector. An axial bore is removed from the center of the detector to provide the opposite contact. Usually the inner bore does not go all the way through the crystal. Coaxial detectors have a better capacitance to volume ratio than planar detectors. A large volume is desirable in order to increase the gamma peak-to-Compton ratio and detection efficiency. Since germanium crystals are grown axially, it's possible to produce very long coaxial detectors, with active volumes up to 800 cm^3 [83, 85].

Section 2.3: PPC Detectors

The P-type point contact detector is the detector configuration of choice for the MAJORANA DEMONSTRATOR, and has been deployed in multiple rare decays searches [53, 92, 93]. The geometry is similar to the low-capacitance planar detector in figure 2.6, however the detector is p-type, the rectifying electrode is n^+ diffused lithium surrounding much of the detector, and the p^+ blocking electrode is small, $\sim$3 mm in diameter point contact. The PPC detector configuration results in low-noise and superior resolution, along with charge collection properties that are well-suited for the pulse shape discrimination required by MJD.

2.3.1: Noise Characteristics

In any detector setup, it's important to minimize the effect of electronic noise. The amount of noise directly impacts detector resolution and energy threshold. Four sources of

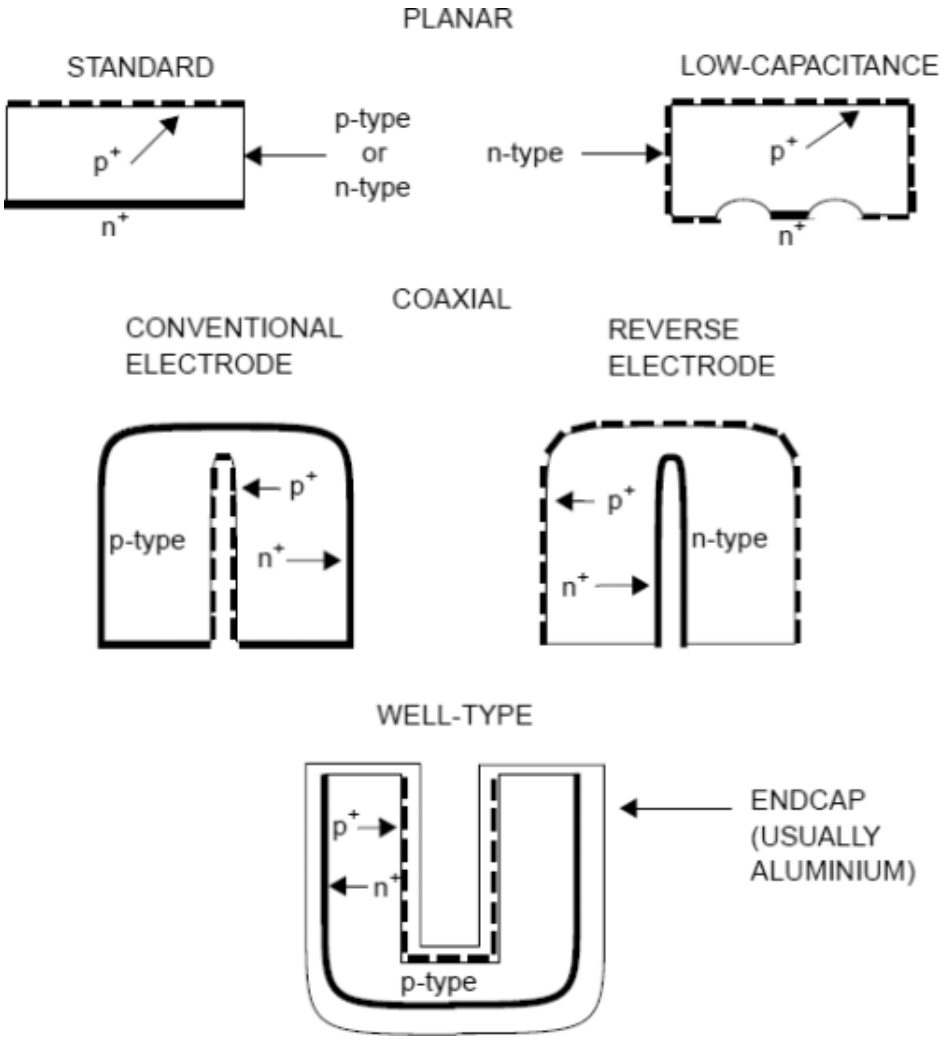

Figure 2.6: Conventional germanium detector configurations with common modifications. In this figure, solid (dashed) black lines represent the n^+ (p^+) contact. Top: planar detectors, with the standard design on the left and the low-capacitance design on the right. Mid: Coaxial detectors. Usually the outer surface is 'bulletized,' smoothing corner regions to remove volume with low electric field. The reverse electrode configuration is useful for detection of low energy radiation. The well-type detector has a wider center bore, radiation sources placed in the center will be detected with high efficiency. Figure from [91].

noise are considered, series and parallel white noise along with series and parallel non-white noise.

The series white noise, denoted by the spectral power density (i.e. the distribution of power over the frequency domain) term a [94], is caused by random thermal noise. It's related to temperature and FET transconductance, g_m by,

$$a = \alpha \frac{2kT}{g_m} \tag{2.5}$$

where k is the Boltzmann constant and α is a constant value between 0.5 and 0.7 depending on the FET operating point. There is also a non-white series $1/f$ term, a_f, which is related to charge trapping in the FET channel [92].

The spectral density of the parallel white noise is denoted, b. It is a shot (i.e poisson) noise related to the leakage current and to the thermal noise of the feedback resistor:

$$b = eI_L + \frac{2kT}{R_f}. \tag{2.6}$$

Here e is the electron charge, I_L is the leakage current and R_f is the feedback resistance. The term including the feedback resistance could be eliminated by using a pulsed-reset preamplifier, however detectors used in MJD have resistive feedback preamps. The amount of leakage current is generally indicative of the quality of detector and FET. Detectors with fewer impurities will exhibit less leakage current, see equation 2.4. The non-white parallel noise term $b_f/|f|$, describes the dielectric noise [94].

After applying a filtered response in the Laplace domain, one can obtain the equivalent noise charge by summing the noise components [94, 95],

$$\mathrm{ENC}^2 = \left(\frac{aA_1}{\tau} + 2\pi a_f A_2\right) C_{\mathrm{tot}}^2 + \left(b\tau A_3 + \frac{b_f}{2\pi} A_2\right) \tag{2.7}$$

where τ is the filter shaping time, A_i is an element of a set of coefficients that depend on

the filter shape, and C_{tot} is the combined detector and FET capacitance. Note that the non-white noise is independent of shaping time. During MJD data acquisition and analysis, a digital trapezoidal filter is applied [96]. The trapezoidal shaping coefficients are $A_1 = 2$, $A_2 = 1.38$, and $A_3 = 1.67$ [95]. In this case, the shaping time includes the both trapezoidal ramp times and the flat time. An example of the ENC^2 plotted versus τ is shown in figure 2.7.

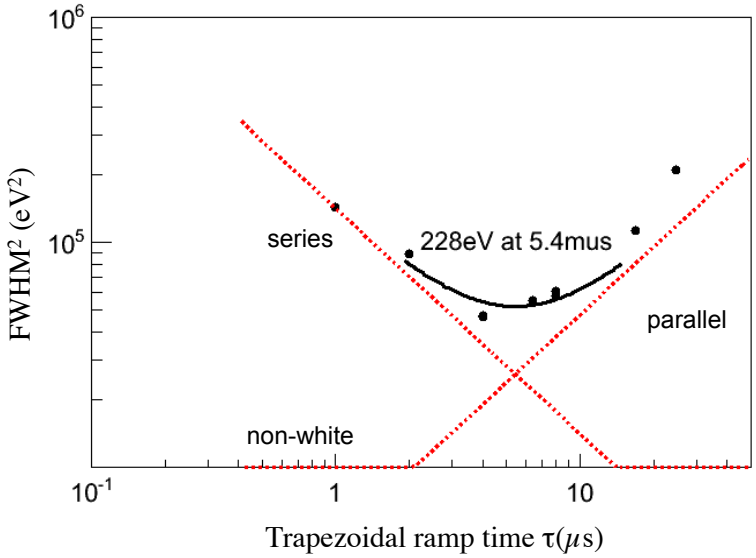

Figure 2.7: An example of the noise curve as a function of shaping time from a MAJORANA research PPC detector. The series, parallel and non-white noise contributions are shown (red-dashed). This is usually measured by finding the FWHM of a pulser peak to exclude the effect of charge production and collection. If white noise dominates, then the shaping time can be adjusted to minimize Equivalent Noise Charge. Figure generated by R. Martin, from [97].

In general, minimizing ENC^2 is desired. Typically this involves adjusting the filter shaping time and measuring the electronic noise. The minimum achievable noise as a function of τ can be found by simply taking the derivative and substituting. The resulting theoretical minimum is:

$$\text{ENC}^2_{\text{min}} = 2\,(abA_1A_3)^{\frac{1}{2}}\,C_{\text{tot}} + A_2\left(2\pi a_f C^2_{\text{tot}} + \frac{b_f}{2\pi}\right) \tag{2.8}$$

Equation 2.8 clearly shows the dependence of the noise on the total capacitance.

The advantage of PPC detectors is their inherently low capacitance. The commonly measured effect of series noise on the width of a pulser peak is directly related to the detector

capacitance and the amplifying field-effect transistor (FET) capacitance [92, 98]:

$$\text{FWHM} = (41\text{eV})V_n(C_D + C_F)/\sqrt{\tau} \tag{2.9}$$

where V_n is the FET noise voltage and τ is the characteristic time of the shaping amplifier. The capacitance of a PPC detector is given by [92, 99]:

$$C_D = 2\pi\epsilon_{Ge}\epsilon_0 r \tag{2.10}$$

where $\epsilon_0 = 8.85 \times 10^{-12}$ Farad/m is the permittivity of free space, ϵ_{Ge} is the germanium dielectric constant, and r is the point contact radius. Typical values for the PPC detector capacitance are ∼1 pF compared to ∼20 pF for a coaxial detector [99].

The low noise due to the small PPC capacitance also results in reduced energy thresholds. There is no standard method for setting detector thresholds. Experiments may simply set their threshold at five standard deviations above the noise pedestal or they might systematically increment the threshold until background rates are reasonable. Equation 2.11 provides a stochastic rate based procedure for threshold finding [92, 100]:

$$R \sim N_0 e^{\zeta^2/\left(2\sigma^2\right)} \tag{2.11a}$$

$$N_0 \sim \frac{1}{4\tau} \tag{2.11b}$$

The rate R, of spurious events above a threshold ζ depends on the detector noise, σ = FWHM/2.355, and the shaping time, τ. Normally τ will be fixed to minimize the noise (equation 2.7), so that the rate at a given threshold depends only on capacitance. Since the capacitance of PPC detectors is a factor of ∼20 better than coaxial detectors, the threshold can be set 20 times lower. Indeed, PPC detectors operating with sub-keV thresholds have been demonstrated [53, 92, 93], whereas the standard coaxial detector thresholds are well above 10 keV [101].

2.3.2: Detector Resolution

Energy resolution is one of the most important qualities of a detector. Germanium detectors are known for their superior energy resolution when compared to other detector types, (e.g ionization chambers or scintillators). For example, at 1.3 MeV the peak resolution for a coax detector is ∼2 keV FWHM, while for a NaI scintillator the FWHM would be 25-30 times larger [83, 84]. PPC detectors perform better than coaxial detectors at low energies (x-ray regime) because they're subject to less electronic noise. Other factors affecting the resolution must be considered as well, including statistical fluctuations in electron-hole pair production and charge collection efficiency.

The detected energy from a gamma radiation[3] event is stochastically spread out over a narrow range. There are four processes that affect the energy resolution of HPGe detectors. When summed in quadrature, these yield the ultimate detector resolution:

$$\sigma_{tot}^2 = \sigma_\gamma^2 + \sigma_p^2 + \sigma_c^2 + \sigma_e^2 \tag{2.12}$$

Each component is briefly described in the following list,

- σ_γ: Intrinsic gamma-ray width. This value is much smaller than the other uncertainties and is considered negligible.
- σ_p: Poisson fluctuations in the number of electron-hole pairs produced by an incoming gamma ray.
- σ_c: Spread of charges collected at the electrodes once the gamma ray energy has been fully absorbed by the detector
- σ_e: Electronic noise component. This was discussed in detail in section 2.3.1.

At low energies ($<$ 500 keV), the electronic (σ_e) and production (σ_p) terms dominate

[3]Since the discussion is focused on HPGe PPC detectors, it will be assumed that any ionizing radiation is a γ or x-ray.

the contribution to the energy spread. The fluctuation in the number of electron-hole pairs produced as a function of energy is given by,

$$\sigma_n(E) = \sqrt{\langle n \rangle} = \sqrt{\frac{E}{\langle \varepsilon \rangle}}. \tag{2.13}$$

Multiplying by the average energy required to produce a pair ($\langle \varepsilon \rangle = 2.96$ eV) results in the uncertainty of the energy absorbed by the detector,

$$\sigma_p(E) = \langle \varepsilon \rangle \times \sqrt{\langle n \rangle} = \sqrt{\langle \varepsilon \rangle E}. \tag{2.14}$$

Note that equation 2.14 predicts a FWHM = $2.355 \times \sigma_p$ for the ^{60}Co 1333 keV line of ~ 4.7 keV, which is large compared to < 2 keV FWHM quoted by detector manufacturers. The discrepancy arises from the original assumption modeling electron-hole pair creation as a poisson process. Each pair creation event is not necessarily independent of other events. The effect is accounted for by introducing the Fano Factor [102, 103], F:

$$\sigma_p(E) = \sqrt{\langle \varepsilon \rangle F E} \tag{2.15}$$

Typical measurements for F in Ge range from 0.057 to 0.12. Usually the measured Fano factor will be provided by the manufacturer on the detector data sheet.

At higher energies (>1000 keV), the charge collection spread has a noticeable impact on the resolution. Charges may become subject to trapping during collection. This results in tailing on the low energy side of the peak. The mathematical form of σ_c is not well understood and is often determined by measuring the total resolution and subtracting out the electronic and production components. In practice this term is modeled assuming a linear relationship with energy, such that $\sigma_c = cE$. A more in-depth discussion on charge collection and pulse shape discrimination is presented in section 2.3.3.

Summing each component in quadrature results in the oft used formula for resolution as

a function of energy,

$$\sigma_E(E) = \sqrt{\sigma_e^2 + \langle\varepsilon\rangle FE + c^2E^2} \tag{2.16}$$

where σ_e, F, and c are usually determined via a fitting routine. The FWHM of a set of known calibration peaks can be measured by a spectrometrist in order to fit equation 2.16. Knowing the resolution as a function of energy is necessary for setting limits in rare-event or low contamination settings. An example of a fit function is shown in figure 4.8.

2.3.3: Charge Collection in PPC Detectors

Ionizing radiation absorbed by a germanium detector liberates a collection of electron-hole pairs with total charge proportional to the incident energy. Under bias, an electric field permeates the detector so that holes migrate to the cathode–the point contact in a PPC detector–and electrons migrate to the anode. The field profile in a PPC detector affects the collection timing characteristics. If a gamma ray were to deposit energy at two different sites in the crystal, an appreciable delay in the induced charge signal may be discernible. Pulse shape discrimination techniques can identify charge collection delay, discriminating between these 'multi-site events' and single-site events. If energy is deposited near the detector dead layer, i.e close to the surface in regions of low electric field, the charge collection time could increase significantly, resulting in energy-degraded slow pulses. In contrast, charge drift times in coaxial detectors are fairly uniform throughout the crystal volume. See figure 2.8.

The output signal from a PPC detector can best be understood by applying the Shockley-Ramo theorem [105, 106]. The theorem provides a method for calculating the charged induced on the electrodes as electron-hole pairs drift through the detector. Each electrode is considered independently. The induced current on an electrode related to the drift velocity, v_d, and the weighting field strength, E_0,

$$i = q\mathbf{v_d} \cdot \mathbf{E_0}. \tag{2.17}$$

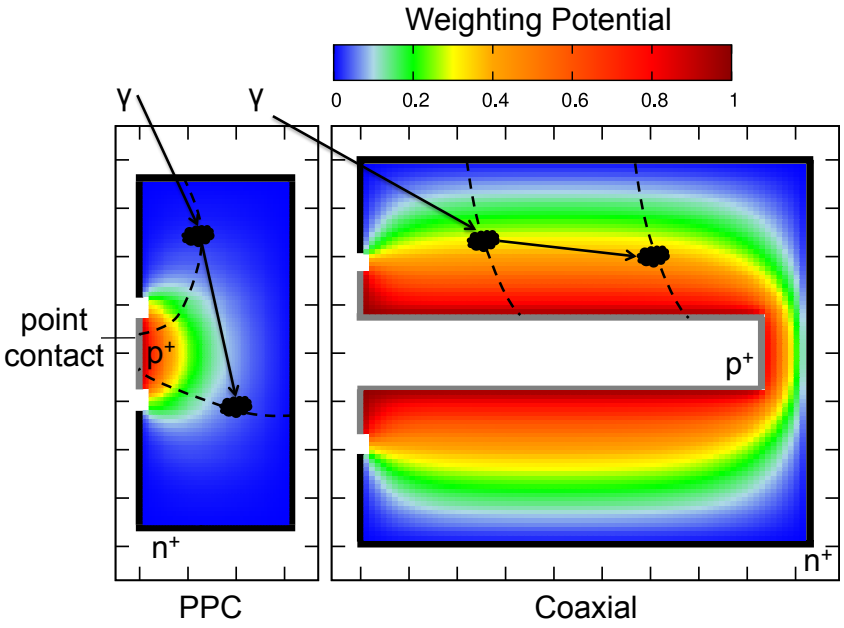

Figure 2.8: Drift paths in a PPC detector (left) and a coaxial detector (right). The incident gamma ray deposits energy in multiple sites in the detector. In the coax detector, the similar drift paths (dahsed) and nearly uniform weighting potential results in similar collection times. The equivalent scenario in the PPC detector results in different collection times at each energy deposition site. Pulse shape analysis can identify the multi-site event, taking advantage of the different drift times. Figure adapted from GERDA PSA [104] and [92].

Note that the weighting field has units of meter^{-1} since its defined from the unit-less weighting potential, $\mathbf{E_0} = -\nabla\varphi_0$. Charge is induced on the electrode as the electron-hole pairs drift through regions of changing weighting potential,

$$Q = -q\left(\varphi_{0,f} - \varphi_{0,i}\right). \tag{2.18}$$

The sum total charge induced on all electrodes is zero. The weighting potential is found by solving the Laplace equation, $\nabla^2\varphi_0 = 0$, for the detector geometry assuming the following boundary conditions:

- The weighting potential on the electrode under consideration (usually the p$^+$ contact on a PPC detector) is set to unity.
- The potential on all other electrodes is set to zero.

Static charge, e.g. space charge or trapped charge, is neglected. A map of the weighting potential with drift paths included for a PPC detector is shown in figure 2.9.

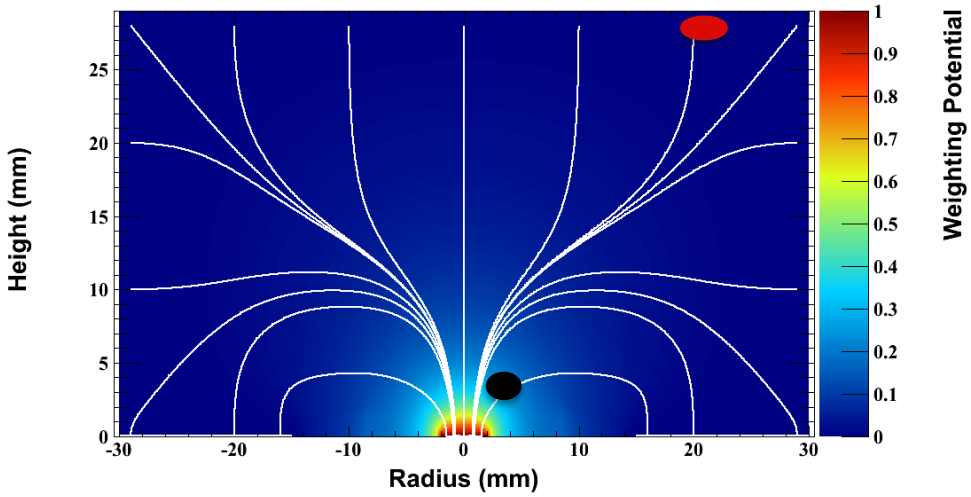

Figure 2.9: The weighting potential mapped in the MALBEK [53, 93] PPC detector. The weighting potential is maximal near the point contact and nearly zero elsewhere. The induced charge will be mostly due to holes drifting near the point contact. The white curves show drift paths. The location where the charge cloud is generated (black or red ovals) can affect the induced charge signal (figure 2.10). Figure generated with the `M3DCR` and `SigGen` packages from `RadWare` [107]. Figure adapted from [53].

According to the Shockley-Ramo theorem, the drifting of both electrons and holes will induce charge on the point contact. From figure figure 2.9 and equation 2.18, electrons produced in the bulk of the detector will induce a minimal charge since they drift toward the n^+ contact, experiencing only a slight change in weighting potential. The majority contribution to the signal will be due to holes as they drift very near the p^+ contact with its sharp potential gradient.

2.3.4: Slow Pulses

For detectors with a thick ($\sim$1 mm) Li drifted n^+ contact, the detection efficiency of low energy (<100 keV) x-rays drops off as energy decreases. As shown in figure 2.9, the weighting potential near the detector surface, in close proximity to the p-n^+ junction, is nearly constant resulting in a weak weighting field. Energy deposited beyond a fiducial layer close to the

junction may not be detected, defining a detector dead layer. PPC detector experiments have reported a small region between the dead layer and the detector bulk where long charge drift times are more likely [53, 92, 93, 108]. The energy distribution of slow pulses is roughly exponential with decreasing energy, and thus constitute a major background for low energy physics searches. Techniques for identifying and removing slow pulse backgrounds will be discussed in chapter 5.

One model that describes the cause and energy distribution of slow pulses identifies three detector regions: the recombination dominant region (RDR), the diffusion dominant region (DDR) and the full charge collection region (FCCR) [53, 109]. Electron-hole pairs produced in the RDR are very likely to recombine, contributing no energy to the signal pulse. The generated charge cloud does not occur at a single point however, and instead has a finite spatial distribution. While some fraction of the energy from the incident radiation may be undetected in the RDR, some of the holes may diffuse into the DDR. In this region the diffusion velocity is the dominant component of the total drift velocity. Charge in this region may slowly diffuse into the FCCR where it's accelerated towards the point contact. The resulting charge pulse is energy degraded with a $t_{10-90\%}$ rise-time of $\sim$1 μs or more, compared to fast pulses with rise time $\sim$200 ns. See figure 2.10.

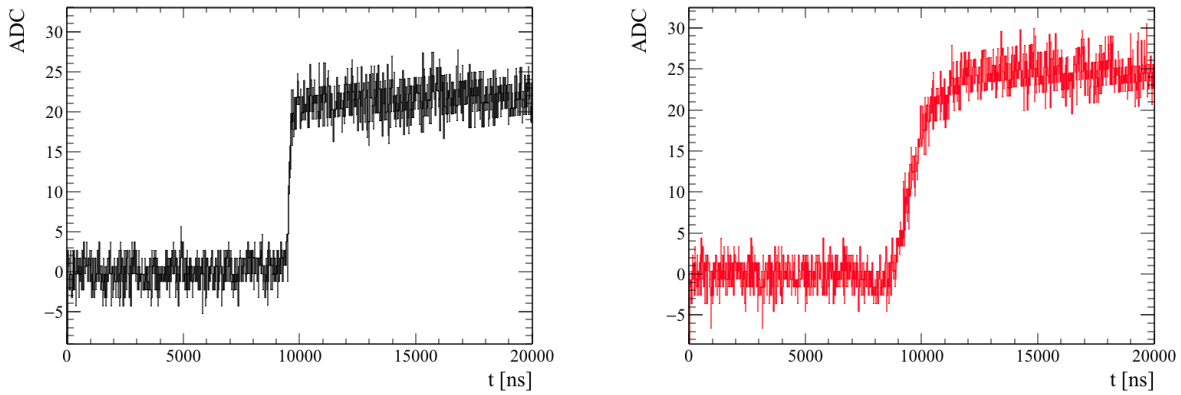

Figure 2.10: Digitized charge pulses from events within a MJD PPC detector. The left (black) pulse is a normal fast pulse, due to a Compton scattering event in the detector bulk (FCCR). Slow pulses, right (red) are a significant background at low energy are often associated with ionization events near the detector surface.

Section 2.4: Summary and Discussion

The P-type point contact detector is well suited for detecting ionizing radiation from a broad energy range. The pulse-shape discrimination capabilities resulting from varying drift lengths are useful for discriminating events at higher energies. This is a powerful background reduction tool for rare-event searches, including neutrinoless double-beta decay in ^{76}Ge. The low-capacitance geometry of the PPC detector is also ideal for low-energy physics searches, improving resolution over the coaxial design and resulting in lower thresholds. Techniques for removing slow pulses are under development that can increase the low energy reach of the detectors.

The results presented in this dissertation were measured with PPC detectors housed in the MajoranaDemonstrator. The MJD will be described more in chapter 3. Further details on background rejections is discussed in chapter 5. Finally, new limits on electronic coupling of bosonic dark matter and other rare decays is presented in chapter 6.

CHAPTER 3: The Majorana Demonstrator

This chapter provides a brief overview of the Majorana Demonstrator (MJD) neutrinoless double-beta decay experiment. The host lab infrastructure and the design of the Demonstrator is described in section 3.2. The focus then shifts to Module 1 (M1) since the data presented in this dissertation was taken during M1 commissioning runs. The chapter concludes with a brief summary of why MJD is suitable for a dark matter search.

Section 3.1: Experiment Overview

The Majorana Demonstrator is a neutrinoless double-beta decay ($0\nu\beta\beta$) experiment [110] taking place in the former Homestake gold mine in Lead, SD [111]. The experiment uses modular arrays of enriched P-type point contact (PPC) high-purity germanium (HPGe) detectors placed in custom ultra-low background cryostats for a combined total of 44.8 kg of detector mass. The Demonstrator makes use of passive and active shielding along with a radon purge in order to reduce external backgrounds. Internal backgrounds are mitigated by careful materials selection, screening, handling and cleaning. An overview of the shield design and module setup is shown in figure 3.1. With the low noise and threshold characteristics of Ge PPC detectors along with the tens of kgs of mass available, the MJD will be a competitive experiment for various dark matter searches.

3.1.1: Neutrinoless Double-Beta Decay

Some neutron-rich nuclei cannot decay via single-beta decay due to energy conservation. These nuclei may instead decay via double-beta decay providing an opportunity to further study this second-order process. See figure 3.2. Two neutrino double-beta decay ($2\nu\beta\beta$,

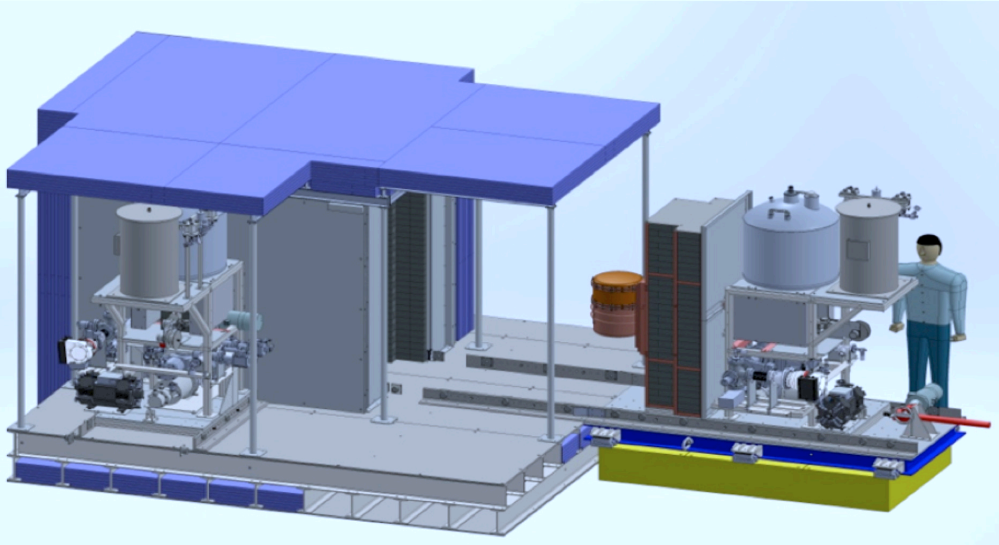

Figure 3.1: Engineering drawing of the MAJORANA DEMONSTRATOR. The shield, consisting of active and passive components, is capable of supporting two cryostat modules.

eqn. 3.1),

$$(Z, A) \rightarrow (Z + 2, A) + 2e^- + 2\bar{\nu}_e \tag{3.1}$$

is an allowed second-order Standard Model process in which two neutrons simultaneously transform into two protons, emitting two electrons and two anti-neutrinos. The first observation of $2\nu\beta\beta$ was in the 1980s by S. Elliott, A. Hahn, and M. Moe [112]. A list of some isotopes that decay via double-beta decay along with their decay half-lives are given in table 3.1.

To date, the only observed form of double-beta decay has been $2\nu\beta\beta$. Another, related variant of DBD is neutrinoless double-beta decay [121] ($0\nu\beta\beta$, eqn. 3.2):

$$(Z, A) \rightarrow (Z + 2, A) + 2e^- \ . \tag{3.2}$$

In this case, two neutrons in a DBD nucleus simultaneously transform into two protons, emitting two electrons and zero neutrinos. In the simple case that $0\nu\beta\beta$ decay is mediated by light neutrino exchange (figure 3.3), the inverse half-life is related to the effective Majorana

Figure 3.2: Decay scheme for isotopes of with A = 76. The energy scale on the left is keV. The ^{76}Ge is energetically forbidden from single beta decaying to ^{76}As, but can double-beta decay to ^{76}Se with a Q-value of 2039 keV. Figure adapted from [113].

mass via equation 3.3,

$$[\tau^{0\nu}_{1/2}]^{-1} = G_{0\nu}|M_{0\nu}|^2\langle m_{\beta\beta}\rangle^2 \tag{3.3}$$

where $G_{0\nu}$ is the phase space factor, $M_{0\nu}$ is the nuclear matrix element, and $\langle m_{\beta\beta}\rangle$ is the effective Majorana mass, i.e.

$$\langle m_{\beta\beta}\rangle = \left|\sum_{i=1}^{3} m_i U_{ei}^2\right| \tag{3.4}$$

In equation 3.4, The m_i are the neutrino masses and the U_{ei} are elements of the Pontecorvo-Maki-Nakagawa-Sakata (PMNS) neutrino mixing matrix, which encapsulate mixing parameters governing neutrino oscillations as they propagate through space along with a Dirac CP violating phase and two Majorana CP violating phases [122].

The full $Q_{\beta\beta}$ value of the decay is split between the emitted electrons (neglecting the nuclear recoil). The resulting detector signature is a narrow peak in at the full energy value of the decay. In other forms of beta decay, part of the energy is carried off by the neutrino(s) that escape the detector due to their intrinsically elusive nature yielding a continuum spectrum. A comparison of $2\nu\beta\beta$ and $0\nu\beta\beta$ is shown in figure 3.3.

Table 3.1: List of select double-beta decaying isotopes and their half-lives. The results are listed by year of publication. Also included are the phase factors ($G^{2\nu}$) and the matrix elements ($M^{2\nu}$), analogous to those in equation 3.3. Table from [114].

Nuclide	$\mathbf{T}^{test}_{1/2}$ **± stat ± sys** [y]	**rel. uncert.** [%]	$\mathbf{G}^{2\nu}$ [$\mathbf{10}^{-21}$ $\mathbf{y}^{-1}$]	$\mathbf{M}^{2\nu}$ [MeV^{-1}]	**rel. uncert.** [%]	**Experiment (year)**
^{136}Xe	$2.165 \pm 0.016 \pm 0.059 \cdot 10^{21}$	±2.83	1433	0.0218	±1.4	EXO-200 (2014) [114]
^{76}Ge	$1.84^{+0.09+0.11}_{-0.08-0.06} \cdot 10^{21}$	$^{+7.7}_{-5.4}$	48.17	0.129	$^{+3.9}_{-2.8}$	GERDA (2013) [115]
^{130}Te	$7.0 \pm 0.9 \pm 1.1 \cdot 10^{20}$	±20.3	1529	0.0371	±10.2	NEMO-3 (2011) [116]
^{116}Cd	$2.8 \pm 0.1 \pm 0.3 \cdot 10^{19}$	±11.3	2764	0.138	±5.7	NEMO-3 (2010) [117]
^{48}Ca	$4.4^{+0.5}_{-0.4} \pm 0.4 \cdot 10^{21}$	$^{+14.6}_{-12.9}$	15550	0.0464	$^{+7.3}_{-6.4}$	NEMO-3 (2010) [117]
^{96}Zr	$2.35 \pm 0.14 \pm 0.16 \cdot 10^{19}$	±9.1	6816	0.0959	±4.5	NEMO-3 (2010) [118]
^{150}Nd	$9.11^{+0.25}_{-0.22} \pm 0.63 \cdot 10^{18}$	$^{+7.4}_{-7.3}$	36430	0.0666	$^{+3.7}_{-3.7}$	NEMO-3 (2009) [119]
^{100}Mo	$7.11 \pm 0.02 \pm 0.54 \cdot 10^{18}$	±7.6	3308	0.250	±3.8	NEMO-3 (2005) [120]
^{82}Se	$9.6 \pm 0.3 \pm 1.0 \cdot 10^{19}$	±10.9	1596	0.0980	±5.4	NEMO-3 (2005) [120]

The observation of $0\nu\beta\beta$ would be a significant discovery of physics beyond the Standard Model. Though the exact decay mechanism is unknown, observation would prove that the neutrino is a Majorana fermion, i.e neutrinos are their own antiparticle [124]. As can be seen from equation 3.2, violation of lepton number conservation would also be observed. Majorana neutrinos provide a mechanism to generate the matter anti-matter asymmetry in the universe during leptogenesis, and provide an explanation for very low upper bounds (<2 eV) on neutrino masses (for more details, see [125, 126]). According to equations 3.3, measuring the $0\nu\beta\beta$ half-life sets a limit on the neutrino mass. This can provide information about the neutrino mass hiearchy, i.e whether the m_3 neutrino mass eigenstate is greater than or less than the m_1 eigenstate [127]. Currently the neutrino is the only known fermion with the potential to be a Majorana particle.

3.1.2: Experiment Goals

The main goals of the Majorana Demonstrator are:

- To demonstrate the technical feasibility of a Ge-based tonne-scale double-beta decay experiment.

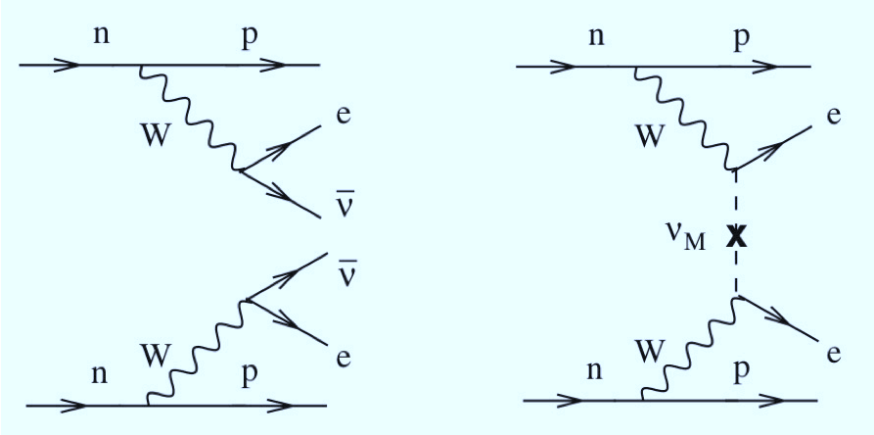

Figure 3.3: Left: Feynmann diagram of $2\nu\beta\beta$. Right: Diagram of $0\nu\beta\beta$ assuming the process is governed via exchange of a light neutrino [123].

- Development of a scalable detector design.
- Search for non-standard model physics in addition to $0\nu\beta\beta$.

Backgrounds

To achieve the first main goal of justifying the building of a tonne-scale germanium experiment, MJ has developed and implemented techniques to reduce backgrounds within the detectors, the detector materials, and shielding. The MAJORANA collaboration has set a background target of 3 counts/tonne/yr (after analysis cuts) in a 4 keV region of interest (ROI) around the ^{76}Ge full energy double-beta decay Q-value ($Q_{\beta\beta}$) at 2039 keV. This value would scale to 1 c/t/y in a tonne-scale experiment due to the increased self-shielding and cleanliness inherent to a larger experiment.

The background requirement is based on the $0\nu\beta\beta$ half-life sensitivity and discovery potential. See figures 3.4 and 3.5. Here, sensitivity is synonymous with an experiment's exclusion power of a parameter of interest, e.g. the $0\nu\beta\beta$ half-life, or an interaction cross-section. More generally, it is a given limit of a one-sided confidence interval beyond which the 'alternative hypothesis,' i.e. positive signal, is rejected. Discovery potential is more optimistic–it's more of an estimate of the significance (e.g. 3σ, 5σ) of a result, though technically it quantifies rejection of the 'null hypothesis,' i.e. background only. In each figure,

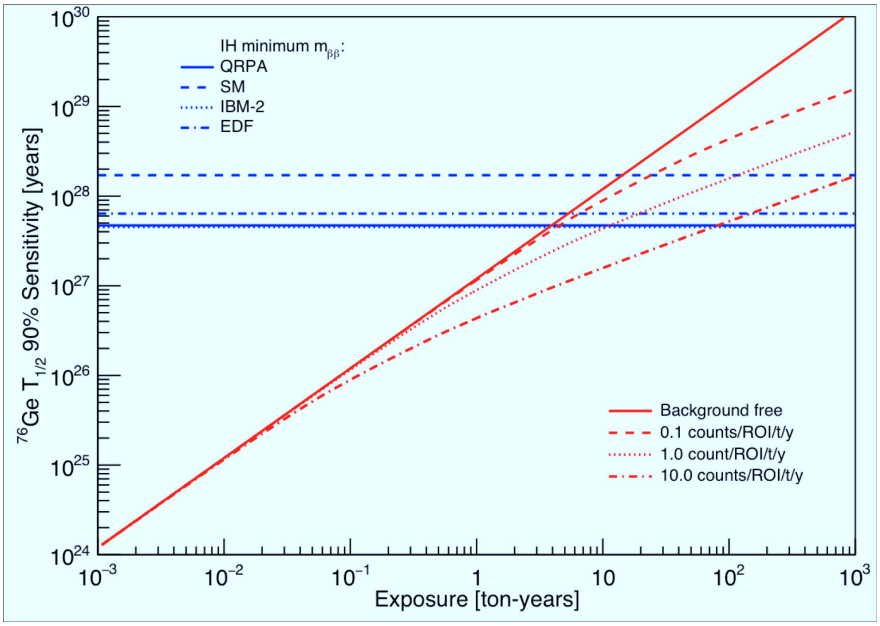

Figure 3.4: Sensitivity to neutrinoless double-beta decay, see equation 3.3. The inverted neutrino mass hierarchy is assumed for the computation of the minimum $\langle m_{\beta\beta} \rangle$ value (i.e. most pessimistic) in equation 3.4, based on measurements (and uncertainties) of neutrino mixing angles and squared neutrino mass differences. The parameter space below the red curves rejects $T_{1/2}$ with at least 90% confidence. The different blue thresholds are a result of different approximations of the nuclear matrix element to compute $T_{1/2}$, including QRPA [128] (solid), shell model (SM) [129] (dashed), IBM-2 [130] (dot), and EDF [131] (dash-dot). Figure generated by J. Detwiler.

the threshold required to completely cover the theoretically interesting $\langle m_{\beta\beta} \rangle$ parameter space (equation 3.4) is shown. The parameter space is computed from measurements of neutrino mixing angles and squared neutrino mass differences [122], assuming an inverted neutrino mass hierarchy (i.e $m_3 < m_1, m_2$). As can be seen in figure 3.5, backgrounds are particularly important for discovery potential. Even at exposures of 100 kg yrs, there is a significant difference in discovery potential among the various ROI BG rates. The current expected ROI count rate of MJD is < 3.5 counts/ROI/t/y [110] (see figure 3.14). For an exclusion comparison to other experiments and an overview of $0\nu\beta\beta$ decay, see [121] and references therein.

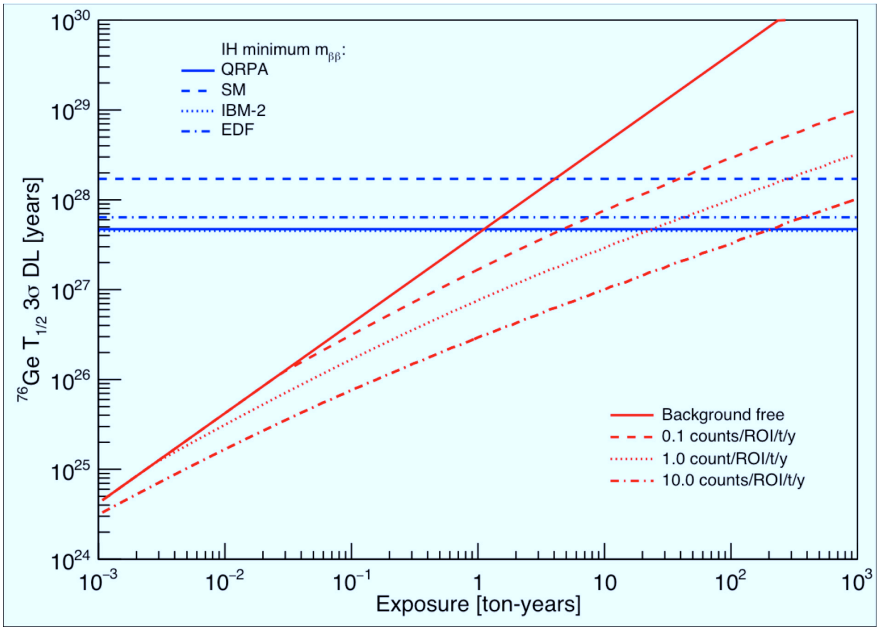

Figure 3.5: Neutrinoless double-beta decay discovery potential, calculated using the same physical parameters as the sensitivity plot, figure 3.4. The parameter space below the red curves reject the background only hypothesis with 3σ significance, i.e. evidence of a $0\nu\beta\beta$ peak should be present at the $Q_{\beta\beta}$ value (2039 keV, ^{7}6Ge). Figure generated by J. Detwiler.

Scalability

The second main goal of the MAJORANA DEMONSTRATOR is to design a scalable experiment. MAJORANA hopes to demonstrate the technical feasibility to construct and field modular arrays of germanium detectors as part of the effort to prove that building a tonne-scale experiment is possible.

The detector design follows a bottom-up approach: MAJORANA detector 'strings' are constructed from four or five PPC Ge detectors, custom-built cryostats each house seven strings, the cryostat and support hardware is assembled into a 'Module', and the modules are inserted into one of two MAJORANA shield ports. A tonne-scale experiment could expand upon this current design, operating multiple modules in parallel. MAJORANA operates two modules, Modules 1 and 2, housing 14 strings with 4-5 detectors each for a combined detector mass of 44.8 kg, with 29.6 kg of enriched detectors [110]. For more information see section 3.2. MAJORANA is collaborating with the GERDA [132] collaboration to determine

which germanium based detector design would be best suited to expand to the tonne-scale. Members from both MAJORANA and GERDA have recently assembled a new collaboration, LEGEND, to continue tonne-scale research.

Additional Physics

The MAJORANA collaboration has set the goal of conducting other non-SM physics searches in addition to $0\nu\beta\beta$. MJD may be sensitive to various dark matter candidates such as WIMPs, axions, and bosonic dark matter particles. Searching for these interactions require the ability to probe the low energy physics within the detector, below ∼20 keV. Because of their low noise characteristics and superior resolution at low energy, PPC detectors such as those utilized by MJD have lower thresholds compared to more traditional coaxial Ge detectors. Sub-keV thresholds have been demonstrated in PPC detectors including MALBEK [53, 93, 108].

Given the scale of the experiment, the DEMONSTRATOR is expected to set competitive constraints on dark matter couplings. Although LUX has ruled out much of the available phase space for spin-independent WIMP interactions [133], the DEMONSTRATOR may be able to improve upon the limit for low mass WIMPs (<10 GeV). Searches for Primakoff conversion of solar axions inside the Ge crystals may also be possible with MAJORANA. Coherent summing of conversion photons via Bragg scattering in the crystal could yield a time dependent signal at low energies [134]. Sensitivity would depend on how well the crystal orientation can be determined. This dissertation focuses on pseudoscalar and vector bosonic dark matter that couple electronically, via interactions analogous to Compton scattering or photoelectric absorption. Because of the superior resolution of PPC detectors at low energy and the larger exposure, the fully operational DEMONSTRATOR will be competitive with XMASS [79] and EDELWEISS [78]. For a more in depth discussion see chapter 6.

Section 3.2: Experiment Infrastructure and Hardware

Based on the goals outlined in section 3.1.2, the basic design principle of the MJD includes scalability of the experiment, radio-purity of all parts and tooling-components in order to keep backgrounds minimal, and cleanliness during construction and operation. Lab-space considerations are also necessary to ensure that cleanliness in an underground environment can be maintained.

3.2.1: The MAJORANA Lab Infrastructure

The MAJORANA DEMONSTRATOR experiment is performed at the Sanford Underground Research Facility (SURF) located in Lead, SD [111]. Most of the MJD lab infrastructure is located on the 4850 ft level of the former Homestake gold mine. The overburden provides shielding from cosmic rays–the muon flux at the 4850 ft level has recently been measured at $(5.31 \pm 0.17) \times 10^{-9}$ /s/cm^2 compared with 2.0 ± 0.2 /s/cm^2 at the surface [135]. The detector is housed in a recently excavated space adjacent to the Davis cavern where Ray Davis constructed his famous solar neutrino detector [136]. The LZ experiment [137] currently occupies that space. The Sanford Lab will also host the DUNE long baseline neutrino experiment [138].

Almost all of the MJD related work at the Sanford lab is performed in a cleanroom. The level of cleanliness depends on the sensitivity of the work being performed. MAJORANA occupies three labs at the 4850 level, and additional work is sometimes performed in the 'surface lab' cleanroom. Most of the MJD infrastructure is contained within the Davis campus, see figure 3.6, where the detector lab, a detector characterization lab, and the machine shop are located. Cleanliness protocols are in place throughout the Davis campus to maintain a buffer between the normal mine conditions and the lab cleanrooms. In 2011, a temporary cleanroom (TCR) was constructed prior to the occupancy of, and roughly a km from the Davis campus that was used for copper electro-forming. It has since been

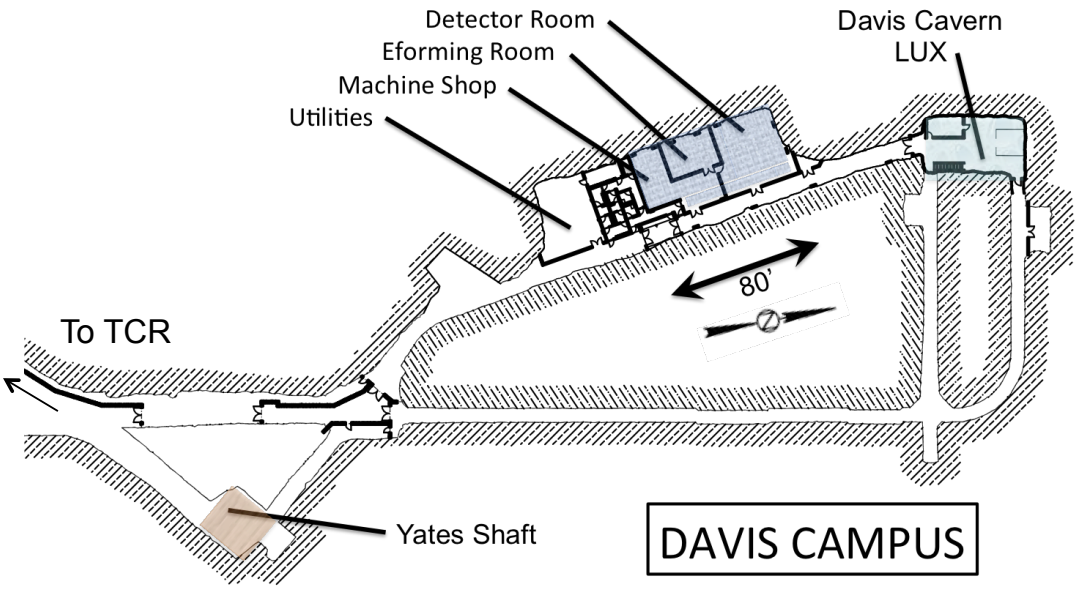

Figure 3.6: A map of the Davis campus. MJD and LUX are located in the clean space (80' drift and blue shaded space). The E-forming room is another name for the characterization lab. Taking a left after exiting the Yates shaft leads to the TCR.

decommissioned.

The TCR was where the MAJORANA collaboration produced copper used in detector components via copper electro-forming (EFCu)[1]. Due to the slow rate of EFCu growth, ten electro-forming baths were set up for parallel production, see figure 3.7. Each bath was capable of producing roughly 100 kg/year of EFCu. To grow the EFCu, commercial oxygen-free high-conductivity (OFHC) copper was placed in a bath filled with a solution of copper sulfate and sulfuric acid. Over time, copper plated onto a stainless steel cathode with dimensions that varied depending on the parts production schedule. Once the copper growth on the mandrel exceeded the desired thickness, it was removed from the bath, packaged, and transported to the machine shop via underground railcar. EFCu produced at the TCR was extremely radio-pure (< 0.1 μBq/kg of U). Because the EFCu was grown and stored underground, minimal cosmogenic contamination in the copper (e.g. ^{60}Co) was produced.

[1]Some early EFCu batches were produced at Pacific Northwest National Lab, but were used for supporting structures and shield components, not detector parts

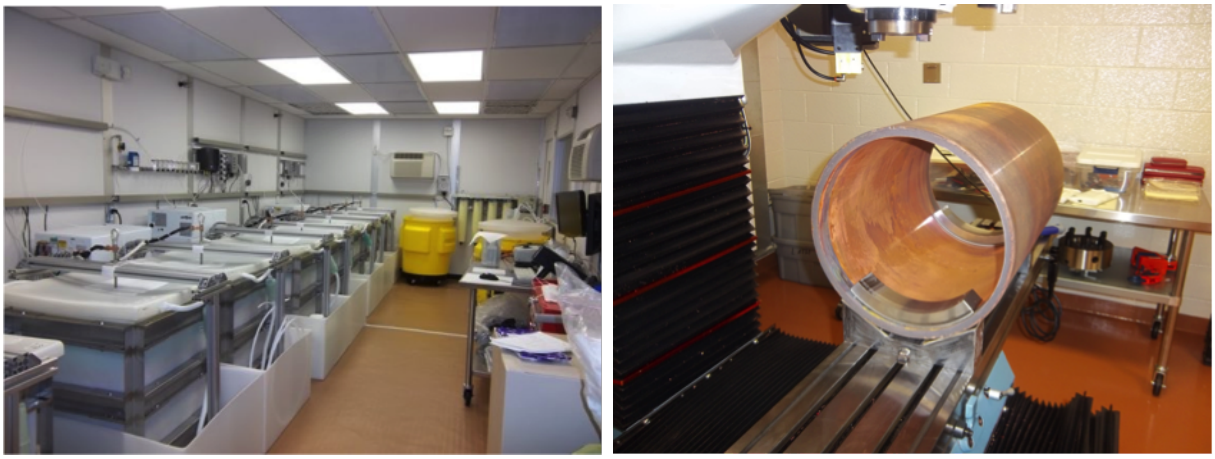

(a) Copper Electroforming (b) Machine Shop

Figure 3.7: (a) A view of the electroforming baths in the MAJORANA electroforming lab. (b) Preparations for milling of EFCu in the underground machine shop.

For more details about copper electro-forming and material testing see [139].

Detector parts and other sensitive components are machined in the underground MJD machine shop, see figure 3.7. The shop also operates as a class-5000 cleanroom. A CNC certified machinist is contracted from Adams-ISC in Rapid City, SD to machine parts, mostly from EFCu produced at the TCR. The shop has the standard machining tools: a mill, a lathe, a bandsaw, and a drill press. There's also an automatic mill and lathe for quicker production of smaller parts such as copper nuts and bolts. For complex parts, a wire-EDM machine is available. An oven is used in the shop during the process of removing copper from the mandrel via a bake and quench procedure, see [139]. To keep track of all the parts produced in the shop, the MAJORANA collaboration maintains an internal parts tracking database [140]. Each part is assigned a serial number that is laser engraved onto the part. The full history of the part including fabrication, cleaning, transportation, and storage is tracked in the database beginning with copper electro-forming on the mandrel.

Adjacent, but separate from the machine shop is the detector room and the characterization room. The detector room is a class-1000 cleanroom that houses the main detector and shielding, the data-acquisition (DAQ) racks, a wet-lab for final parts cleaning, and a liquid nitrogen (LN) purged glovebox for detector string assembly and installation. Machined parts

undergo cleaning to remove surface contaminants introduced during shipping and handling in the wet-lab. String work is performed in the class-5, liquid nitrogen (LN) purged glovebox in order to reduce radon and other contamination of critically sensitive detectors. Shielding will be discussed more in section 3.2.3, while Module 1 is the subject of section 3.3. The characterization room is used mainly for individual detector and string tests.

3.2.2: Detector, String, and Cryostat Assembly

Detector, string, and cryostat assembly is performed in the glovebox. The glovebox is divided into three sections, each engineered for the progressive stages of string building and assembly. Individual detectors are assembled in the detector glovebox. Multiple detectors are assembled into detector strings in the string assembly glovebox. Each string is loaded into a cryostat in the module glovebox; a total of seven strings can be loaded into a cryostat assembly.

Assembly of detectors and strings can only begin if the glovebox has been cleaned. Cleaning involves wiping down surfaces with deionized water and ethanol. The glovebox is continuously purged with LN boil-off. Particle counts are monitored at all times, and must return to normal levels after glovebox cleaning before work can commence. All parts and tools required for detector building are accounted for in the glovebox; any extra required parts are gathered from a nitrogen purged dry box and placed in the glovebox antechamber. Components in the antechamber must be purged with nitrogen gas for 24 hours before being moved into the work space.

A detector assembly consists of the germanium crystal, an EFCu high-voltage ring for detector biasing, a grounded point contact electrode for charge collection, and a low-mass front-end (LMFE) for signal readout. The assembly is held together with hollow EFCu hexagonal bolts and teflon nuts. All components are handled according to strict protocol outlined in the detector assembly procedure [110]. Building the detectors can be especially challenging because personnel working in the glovebox will often have four layers of gloves

(a) Detector Assembly (b) String Assembly

Figure 3.8: (a) A MAJORANA detector assembly. The germanium crystal is supported by an EFCu frame consisting of the HV ring (bottom), hexagonal bolts, and a detector mount. The LMFE is attached to the center of the detector mount (b) A string assembly consisting of a stack of four detectors being loaded into a module. Loading is performed in the module glovebox.

(2 from the cleanroom suit, the glovebox glove, and a clean glove over the glovebox glove) resulting in inhibited dexterity. The LMFE is particularly fragile due to its low mass required because of its proximity to the detector. Contact with the LMFE surface can damage the tiny wire bonds connecting the JFET to the pads on the silica board. Ultra-fine 50-gauge PICO-COAX cables [141] are epoxied to the board to connect the LMFE to a preamplifier or a diagnostic tool. After the LMFE is installed, the detector baseline is checked via the first stage preamplifier output to ensure no connections on the board were broken. An example of a detector assembly is shown in figure 3.8.

Once enough detector units are completed (four or five depending on the string size), they are transferred to the string building glovebox via an interlock chamber. The same cleanliness protocols as the detector glovebox apply when working in the string glovebox. Detectors are stacked and held together using three tie rods that fit through the hollow hex bolts. At the top of the string is an adapter plate that is used to attach the string

to a copper coldplate that's kept in thermal contact with a mass held at LN temperature. Some additional hardware is used for cable management. Completed strings undergo initial testing and characterization outside of the glovebox in a custom-designed string test cryostat. After a string undergoes testing, it is then transferred to the module glovebox to prepare for cryostat loading. See figure 3.8.

The third chamber of the glovebox is the module glove box, used for loading strings into one of the MAJORANA custom built cryostats, see figure 3.11. The full module must be docked to this glove box to install strings into the cryostat. String loading is performed by raising the string using a lift to secure it in place while it's bolted to a coldplate capable of holding seven strings. The coldplate is attached to a copper hoop that has been electron-beam welded to a crossarm tube[2]. Cabling from the string is run through ports in the coldplate and attached to an adapter on the opposite side. Additional cabling runs through the crossarm tube to the service body feedthroughs of the module vacuum system. The crossarm tube houses cabling and a thermosyphon tube for cooling of the coldplate [142], while simultaneously providing a vacuum path for cryostat pumping [110].

After all the strings are loaded and the cabling connections checked, preparations for sealing the cryostat are made. A thin copper IR shield is placed around the detectors to reduce IR shine that affects detector temperature, and thus leakage current, during operation. To seal the cryostat, the cryostat can is placed on the lift, raised up, and then carefully clamped to the hoop. A copper lid is placed on top of the hoop, completing the cryostat assembly.

Once initial roughing vacuum leak checks are complete, the cryostat is pumped down to ultra-high vacuum. This can take multiple days because of the large volume and the amount of material obstructing the crossarm tube, e.g. cabling, and IR shine-path shielding.

[2]E-beam welding was performed by Electron Beam Welding Associates in Indianapolis, IN. To minimize cosmic ray exposure, the parts were driven and detailed logs were kept of the time that the parts were above ground. A muon counter was taken along with the parts in an attempt to quantify cosmic ray exposure during the trip.

When the vacuum pressure is low enough, $\sim 10^{-5}$ Torr, the thermosyphon cooling system is pressurized to begin cooling the strings. Heat from the coldplate is carried away by the two-phase nitrogen working fluid in the thermosyphon tube. A dewar filled with LN, housing a condenser placed at a height above the coldplate, serves as a thermal reservoir for the two-phase fluid. A ballast tank is used for pressure equalization. Gravity stimulates the convective heat flow between the coldplate and dewar [142]. Once the detectors' temperature is low enough they can be biased. Diagnostic data is taken while the module is attached to the glovebox to ensure the module is ready to be moved into the shield.

3.2.3: Detector Shielding

The DEMONSTRATOR shield consists of both passive and active layers. Two keyed ports in the shield allow for the docking of two independent modules in adjacent faces of the shield. An overview of the shield design is shown in figure 3.9.

The cryostat, lead shield monolith, and electronic and vacuum hardware for a module are built on a sliding bearing table designed for a heavy load that rests on a track. To move a module from the glovebox, the locks on the track that secure the module in place can be released, allowing the module to slowly roll onto an air bearing transport ("hovair") platform [143]. The hovair platform can be used to guide the module around the lab in order to transfer it to the shield port. The platform docks close to the shield and the module is rolled into place, guided by tracks on the shield over-floor. Moving the module is a delicate task, and usually takes a full day of planning and effort.

From inside the shield, the cryostat is immediately surrounded by two layers of copper shielding, the first layer is 2" thick EFCu, while the second layer is 2" of OFHC. These two layers of Cu protect from Pb x-rays, bremsstrahlung, and other forms of naturally occurring radioactive materials in the Pb shielding. The total weight of the lead in the shield is approximately 54 tons. A LN boil-off purged radon exclusion box encapsulates the lead. Active muon veto panels detect any muons that pass through the detector. These panels

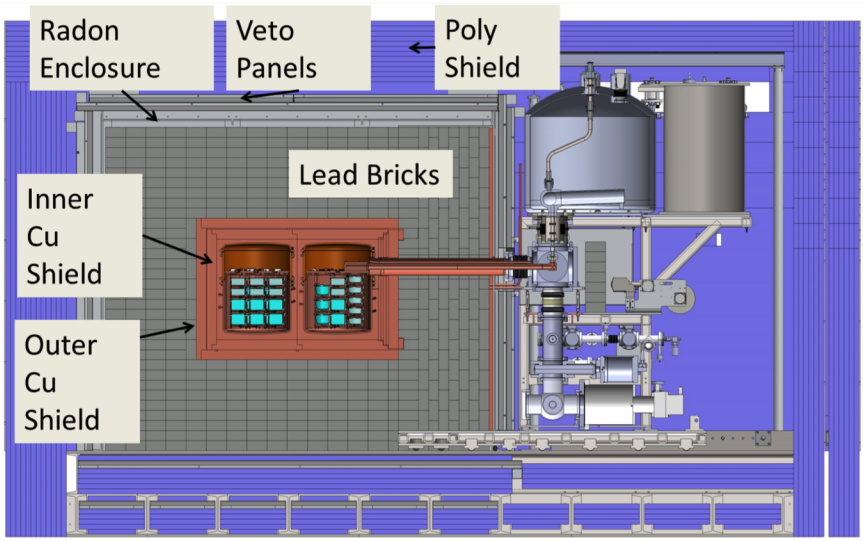

Figure 3.9: A cross section of the MJD shield. An active muon veto surrounds the the lead and copper passive layers. The inner shield and modules are enclosed by borated polyethylene. On the right, a module model consisting of the cryostat, crossarm tube, vacuum service body, LN dewar and ballast is docked to the shield.

also allow studies of the muon flux incident on the MJD and also the effect of muon-related events in Ge detectors [135, 144]. The outer most layer is a borated polyethylene neutron shield. This helps mitigate any neutrons from the cavern, e.g (α, n). It should be noted that the shield rests on an over-floor, and that veto and poly panels can be installed inside the over floor so that there is coverage on all six sides.

For the analysis in this dissertation, the shield was incomplete. The most significant shield component missing was the inner EFCu shield. Installation of the inner copper shield was completed in Dec, 2015 after M1 commissioning. Additionally, installation of some of the veto panels was incomplete as of Jan 2016. Because Module 2 was still under construction during the data taking period, a special blank monolith was installed in place of the Module 2 monolith to provide shielding for M1.

Section 3.3: Module 1

Data for the analysis presented in this dissertation was taken with Module 1 of the MJD from July to October, 2016. This section will provide an overview of Module 1 detector configuration and DAQ. Preliminary simulation work will also be discussed. For a more in-depth analysis of the data, see chapters 4-6.

3.3.1: Configuration

Module 1 contains seven detector strings. Strings are mounted to the coldplate–the EFCu mass that's in thermal contact with the thermosyphon tube–see figure 3.10. Each string has four detectors, with the exception of the five detector string in position four. Both natural and enriched ($\sim$88% ^{76}Ge) Ge crystals are used in M1. There are 20 enriched detectors, with a total mass of 16.8 kg and nine natural detectors with a total mass of 5.7 kg. All of the natural detectors are BEGe's [90], made by CANBERRA Inc., while the enriched detectors were manufactured by ORTEC [87]. Germanium enrichment was performed by ISOFLEX [145]. General module construction details are given in section 3.2.2. A picture of Module 1 during construction in the glovebox is shown in figure 3.11.

3.3.2: Electronics Readout and Performance

Each detector in Module 1 is equipped with an independent signal-readout circuit. Signal amplification proceeds in two stages. The first stage consists of a low-mass front-end (LMFE), which contains the input FET and the feedback components, along with a preamplifier. As shown in figure 3.8, the LMFE is located close to the detector resulting in minimal stray input capacitance. Long cabling, extending through the crossarm tube, connects the LMFE to the preamplifier located outside of the cryostat. The second stage is capacitively coupled to the first, and provides differential dual gain output. An illustration of the readout circuit is shown in figure 3.12.

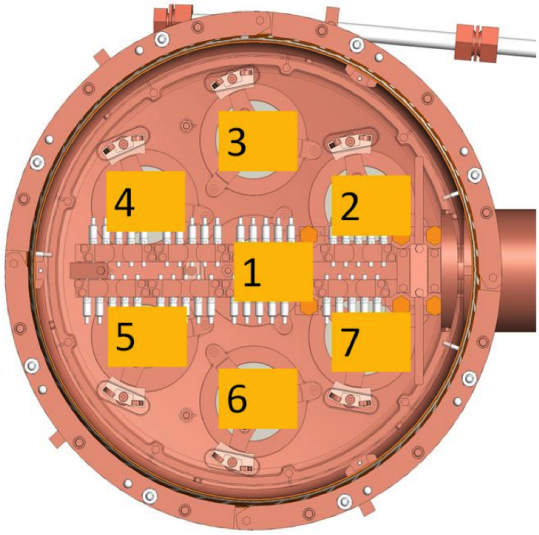

Figure 3.10: A top down view of the cold plate showing the string positions in Module 1.

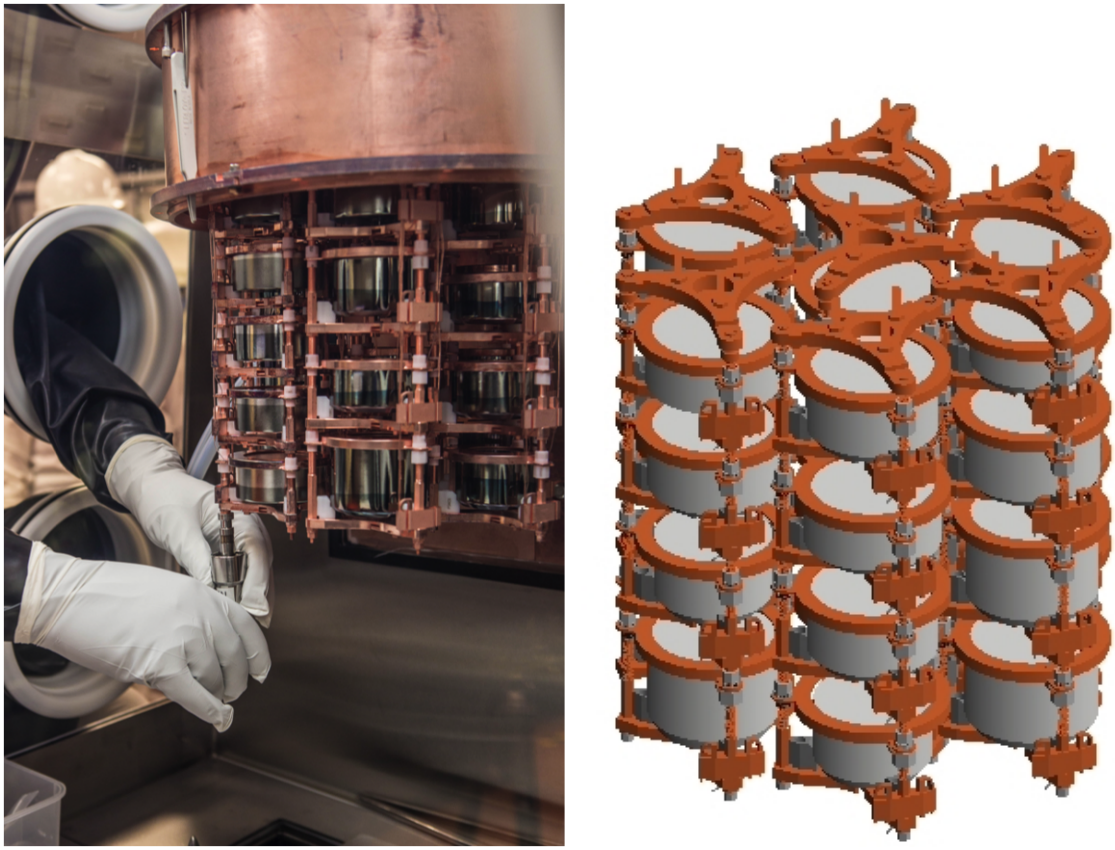

(a) Module 1 (b) Simulated Assembly

Figure 3.11: (a)Module 1 in the module glovebox during construction. Photo credit: Matthew Kapust. (b) Seven string array geometry in MaGe generated with the flexible string geometry framework.

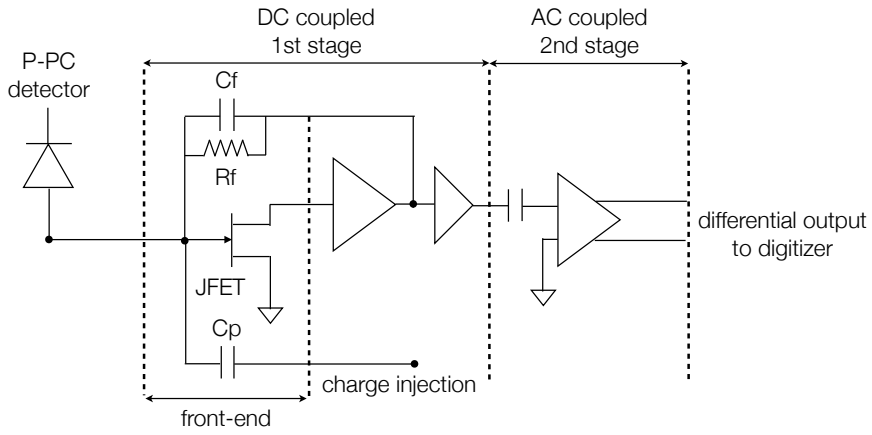

Figure 3.12: High-level view of the detector readout electronics. The first-stage is a low-mass front end (LMFE) resistive feedback circuit connected by long cabling to a preamplifier. Long cabling connects the LMFE to the second-stage preamplifier, which provides dual-gain . Figure from [146].

The LMFE is a resistive feedback circuit. Since the DEMONSTRATOR consists of multiple detectors, the simpler feedback design was preferred over the alternative pulse-reset architecture. The compact design of the LMFE was necessary due to its proximity to the detector. The mass of the 20.5 x 7 mm^2 LMFE is roughly 80 mg. The board substrate is fused silica, which has a low thermal conductivity. This allows for large temperature gradients across the board, so that the FET temperature can be maintained within the optimal operating range for noise performance. The FET is a low-noise Moxtek MX-11 die (i.e. the material on which the circuit is fabricated) with high transconductance and low input capacitance. At cryogenic temperatures, the resistance of the feedback resistance is roughly $\sim$10-100 GΩ. The feedback capacitance is $\sim$0.2 pF. Low-noise levels have been achieved with the LMFE: without a detector, the noise charge is 55 eV FWHM, and with a small PPC it's as low as 85 eV. The noise charge measured with Module 1 detectors is higher due to larger detector capacitance, see for example, figure 2.7. For more information about the LMFE, see [110, 146].

Readout boards are housed in an electronics box that is attached to the vacuum service body. Preamplifiers are grouped by detector string positions in the electronics box. Due

to the long cabling in the first stage, the pre-amplifer rise-time increases from ∼10 ns to roughly 40-70 ns. The fanout of the second stage is piped to the data acquisition hardware.

3.3.3: DAQ

Data acquisition for MAJORANA is managed by the ORCA[147, 148] (Object-oriented Real-time Control and Acquisition) software package. Along with managing acquisition hardware readout, ORCA also handles real-time data visualization, process control, and slow controls monitoring. Other collaborations, in addition to MAJORANA, have also used ORCA including SNO [149], HALO [150], and KATRIN [151].

An overview of the Module 1 DAQ is shown in figure 3.13. Digitizers originally designed for the GRETINA [152] detector group were modified for use with the DEMONSTRATOR. The GRETINA card is a combination of a digitizer and digital signal processor with 10 channel inputs that connects with a VME backplane [153]. The nominal digitization frequency is 100 MHz with 14-bit ADC precision. A field-programmable gate array (FPGA) performs digital trapezoidal shaping and pole-zero correction for online energy calculation. Waveform triggering occurs if the online energy exceeds the trigger threshold set by the DAQ operator. The ADC threshold is set low enough to search for low-energy physics (equivalent to ∼1-2 keV), but high enough to avoid triggering on baseline noise. If the threshold is too low the trigger rate and the size of the output files can increase by many orders of magnitude, see section 2.3.1.

Housed within the same VME crate are CAEN [154] cards used for readout of veto electronics. A trigger/scalar card provides a common clock for all attached devices. Each VME crate has one slot reserved for a single board computer (SBC). The SBC and a desktop computer running ORCA are on the same private network. All communication with the SBC is handled by ORCA through a TCP/IP socket, i.e via ethernet cable.

Data collection is separated into runs–each run is an hour long unless the run file exceeds 2 GB. Large run files are common during calibration runs, where the average run time for

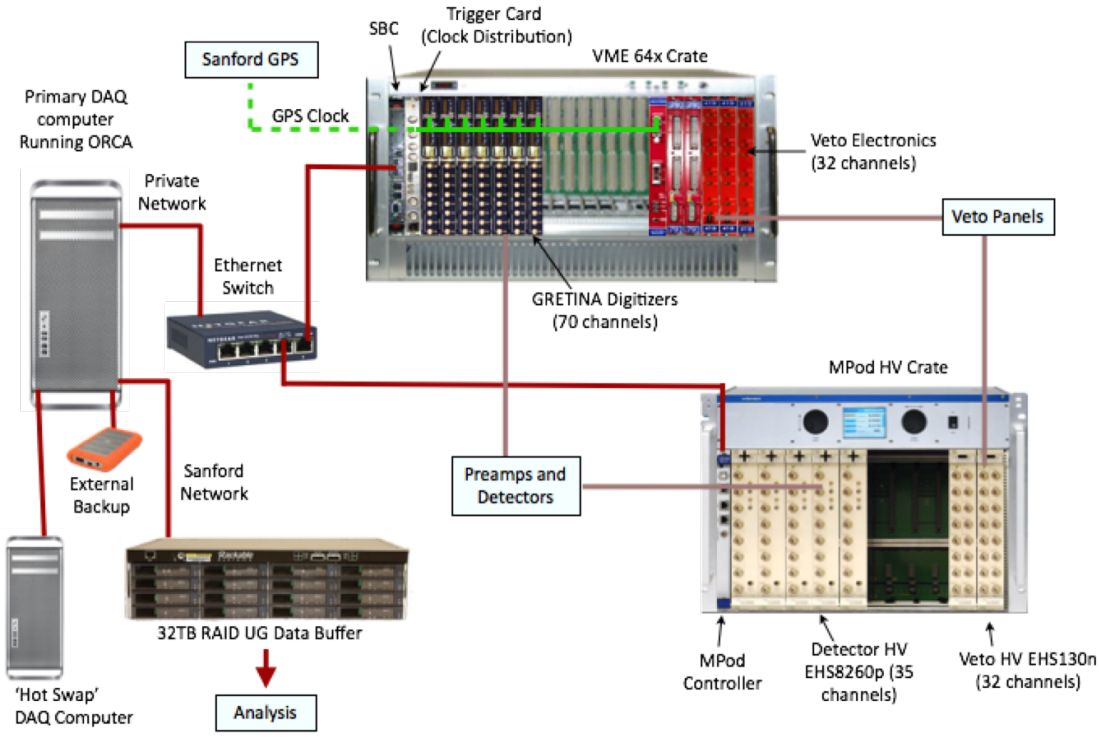

Figure 3.13: Data acquisition overview for Module 1. The MPod crate and HV cards for detector biasing is also shown. Figure provided by Mark Howe.

a file is only 10 minutes. A new run automatically begins upon termination of the previous run. Data from each run is temporarily stored on a RAID server in the detector room until a cron job ships the data to PDSF [155], a cluster located in Berkeley, CA managed by the National Energy Research Scientific Computing Center (NERSC).

3.3.4: Anticipated backgrounds

Background rates in Module 1 were estimated after performing an extensive assay campaign of all parts and materials used for detector and shield construction. Monte Carlo simulations using MaGe [156], a front-end for Geant4 [157, 158] developed jointly by Majorana and Gerda were used to compute the number of counts in the $0\nu\beta\beta$ region of interest. The results are shown in figure 3.14.

Bremsstrahlung and Compton scattering produce a continuum background in the low-energy (<100 keV) region analyzed in subsequent chapters. The continuum rates are corre-

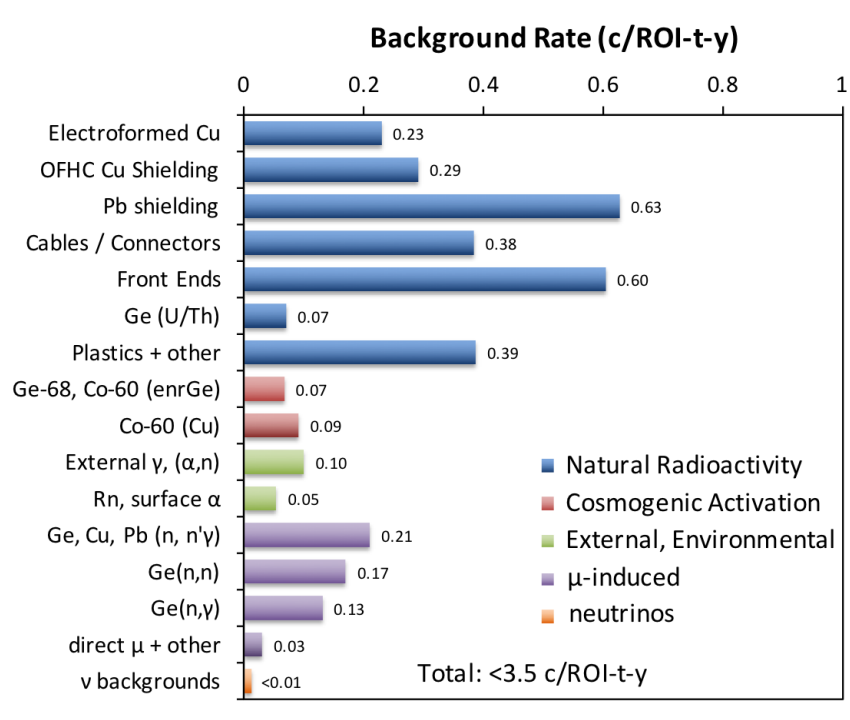

Figure 3.14: The expected background rate in the $0\nu\beta\beta$ ROI from materials used in the construction of the DEMONSTRATOR. The contribution from μ-induced and neutrino backgrounds are also shown. Figure generated by J. Detwiler [110].

lated with the activities measured during assay. At energies below 20 keV, cosmogenic activity (e.g. tritium, ^{68}Ge) from detector surface exposure produces the dominant background. Cosmogenic backgrounds are irreducible and only decrease as the cosmogenic products decay away. Since the tritium half-life is 12.3 years, the measured rate will persist throughout the duration of the DEMONSTRATOR live time. The background model is shown in figure 4.7.

CHAPTER 4: Characterization of Data and Systematics

In this chapter I review the dataset that was used for the dark matter analysis. Experimental systematic parameters that directly effect the rare-event sensitivity are computed. A discussion of the data selection provides context for the exposure calculation. The calibration method is reviewed and correction factors are computed. A discussion of the calculation of the resolution curve in the low energy region is also provided. A table listing the systematic parameters is given in the summary.

Section 4.1: Data Selection

Data presented here was taken during the 2015 in-shield commissioning of MJD Module 1. This was the first set of data collected with a full set of 7 strings housed in an electroformed copper (EFCu) cryostat, and is designated Data Set 0 (DS0). A subset of the DS0 data was used for the dark matter analysis that was acquired between June 30th and Sep. 22, 2015.

4.1.1: Data Description

Data is segmented into 'runs', a term used by ORCA. Each run contains digitized detector waveform data along with run meta-data, such as the run collection time interval (i.e run length), run category, and quality control flags implemented as a bit mask. The duration of most runs is usually set to one hour, though the 2 GB file size constraint can result in shorter run lengths. At the end of each run, data collection is stopped and transferred to redundant storage servers for additional processing. A new run begins automatically and the process repeats until it's interrupted by a DAQ user or a system crash.

DS0 consists of three categories of data: calibration, characterization, and background

data. Calibration and characterization runs were interspersed between background runs in DS0. Calibration runs were performed every few days to compute calibration parameters for each detector in order to correct for long-term drifts in energy gain. The calibration procedure will be discussed in more detail in section 4.2. Characterization runs were used for systematic and quality control measurements. Examples include: runs during which a script performed threshold optimization by measuring event rates as a function of energy threshold, and runs used to estimate the efficiency of data cleaning cuts (discussed in section 5.3.3). Background runs consist of the sets of non-diagnostic data taken without a calibration source in place. These runs will be the main focus of the physics analysis in chapter 6.

During commissioning, background run quality was classified as either good (also referred to as 'golden') or bad [159]. Only good background runs were used for physics analyses. Multiple criteria differentiated between good and bad runs, including run duration, slow controls' status, and event rate. Bad runs often exhibited event rate bursts, or short time intervals ($\sim$5 mins) with abnormally high event rates. Bursts were generally attributed to personnel activities in the detector lab. For example, 1000 fold rate increases were measured when the wire-EDM machine was operating in the machine shop. Elevated rates were also found to be correlated with time of day: detector rates were often lower at night and during the lunch hour. A spreadsheet maintained by the run selection and data cleaning group kept track of good and bad runs. Some additional criteria were applied to the run selection for low-energy analysis. Run selection will be discussed further in section 4.1.2.

4.1.2: Analysis Live-time and Exposure Determination

The exposure calculated for the low-energy analysis is the product of the total active mass of the detectors and the run live-time. Each run contains the start and end time so that the live-time can be computed. Before the total DS0 background live-time can be computed, the detector and run selection must be completed.

Of the 29 Module 1 detectors, 13 were used for DS0 low-energy physics analyses. The

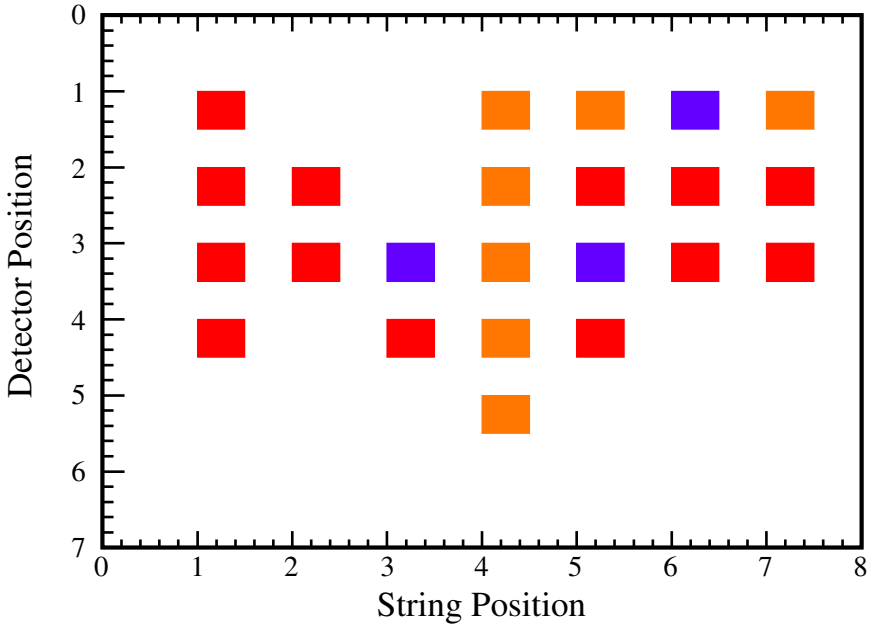

Figure 4.1: A representation of the Module 1 status during the commissioning period. The string positions are represented on the x-axis and the detector number, from top to bottom is shown on the y-axis. A specific detector is referenced as PxDy, where x and y correspond to the axes labels. The red markers indicate the position of enriched ORTEC OPPE [87] detectors that were considered in the physics analyses of background data. Orange markers indicate natural BEGe [85] detectors that were used during systematic characterization but were excluded from physics data analysis. Purple markers were biased enriched detectors that were too noisy to use. The unmarked positions P2D1, P2D4, P3D1, P3D2, P6D4, and P7D4 were unbiased during DS0 taking.

natural germanium detectors had more surface exposure than the enriched detectors resulting in a ∼10 fold increase in their cosmogenic background rate, see figure 4.7. They were excluded from the physics analyses, though seven of the nine natural detectors were used for validation of systematic parameters. Six Modue 1 detectors were unbiased during DS0 because of high-voltage connectivity problems. Three enriched detectors were highly sensitive to microphonic and electronic noise, resulting in high event rates at low energy. The latter nine detectors were not considered during physics analyses or systematics characterization. A map of the Module 1 detector positions is shown in figure 4.1.

Background runs identified on the Run Selection Working Group's DS0 spreadsheet as

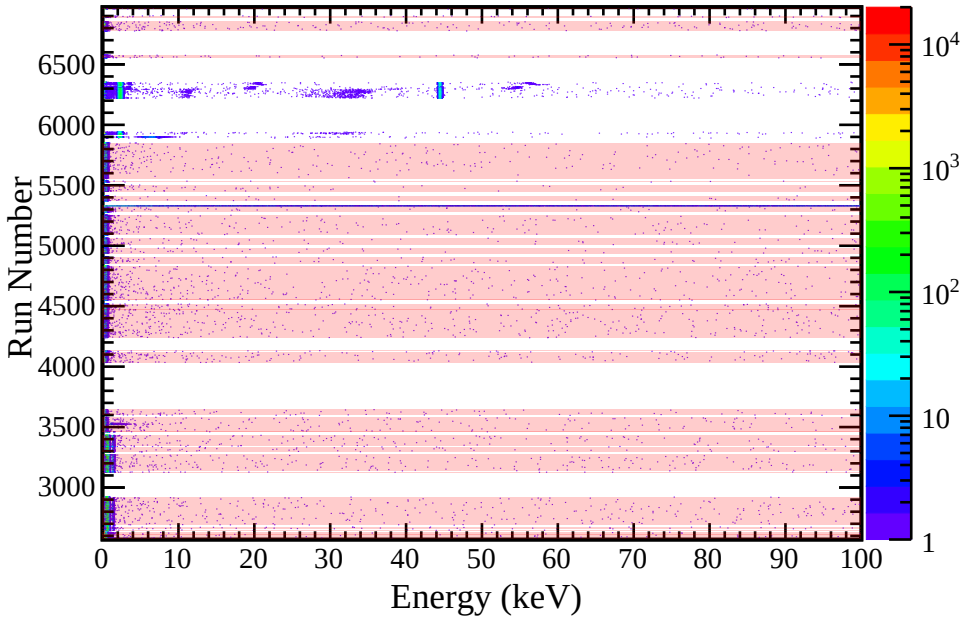

Figure 4.2: Histogram of run number vs energy after data cleaning cuts are applied (see chapter 5). The shaded red bands are runs that were included in the physics analyses. A number of artifacts remain in runs that were excluded. Pulser issues resulted in high event rates between runs 5880 and 6350. The solid line at run 5331 is actually a calibration run that was mistakenly left in the preprocessing list. There is a very low energy artifact in run 3523. The vertical band on the left side is due to the noise pedestal. White bands with no spectra are either calibration, characterization, or bad background runs.

'good' were considered for low-energy analysis. Some of the good runs on this list had abnormally high event rates at low energy, and had to be cut from low-energy selection. High-rate background runs were identified by generating a 2-D histogram of run number vs energy spectra. An example is shown in figure 4.2. Runs with an abnormally high rate (non-poisson) were visually rejected from the run selection criteria. Rejected runs include runs with pulser issues (5880 - 6350) and a calibration run mistakenly flagged as a background run (5331). The final run selection list is shaded red in the figure.

The live-time is calculated using the run list shown in figure 4.2. There is a two second run live-time uncertainty for each run, corresponding to one second at both the beginning and end of the run. A total of 2293 runs were used in the analysis, resulting in a

$\sqrt{(2\text{ s})^2 \times 2293} \approx 96\ s = 0.0011\ d$ uncertainty. The total live-time for the DS0 background data used in this analysis was 47.503 $\pm$ 0.001 days.

The event rate in each detector was low enough to neglect dead time resulting from detector recovery after signal generation and from the DAQ readout rate. This was true even after applying a detector multiplicity cut (see section 5.2.2). A periodic pulser was injected into each detector's preamplifier to ensure the readout was live throughout an entire run's duration. The live-time fraction of each run was estimated by comparing the trigger rate at the pulser-peak 'energy' measured by the Gretina card. This comparison was checked for each run that the pulser was active and a live-time fraction was found to be >99.999% [160].

The active mass fraction is used for exposure calculation. The manufacturer provides the total mass and the dead-layer thickness of each detector. The dead-layer thickness and detector dimensions are used to compute the dead-layer volume. Detectors' physical dimensions were measured with $\mathcal{O}(10\ \mu\text{m})$ precision using a Starrett precision measuring tool [161]. Subtracting the dead-layer volume from the total detector volume gives the fiducial volume. The ratio of the fiducial volume and the total volume is the active mass fraction (assuming constant density), and is shown for each detector in table 4.1 [162]. Summing the masses of the 13 enriched detectors results in a total active mass of 10.06 $\pm$ 0.13 kg. The total active mass of the 7 natural detectors is 3.90 $\pm$ 0.07 kg. To be conservative, the active mass uncertainties of each detector are added linearly since each Starrett measurement isn't necessarily independent.

Exposure was computed separately for the enriched and natural detectors in figure 4.1. Combining the 47.503 $\pm$ 0.001 live-time and the 10.06 $\pm$ 0.13 kg active mass of the enriched detectors yields a total low-energy DS0 exposure of 478 $\pm$ 6 kg d. The natural detector exposure is 478 $\pm$ 6 kg d.

Table 4.1: Table of the active masses of Module 1 detectors used in the bosonic DM analysis along with the masses of natural detectors used for systematic checks.

Detector	**Active Mass Frac.**	**Active Mass (kg)**	**Detector**	**Active Mass Frac.**	**Active Mass (kg)**
P1D1	0.90 ± 0.01	0.51 ± 0.01	P6D3	0.92 ± 0.01	0.70 ± 0.01
P1D2	0.93 ± 0.01	0.98 ± 0.01	P7D2	0.91 ± 0.01	0.71 ± 0.01
P1D3	0.90 ± 0.01	0.91 ± 0.01	P7D3	0.94 ± 0.01	0.59 ± 0.01
P1D4	0.93 ± 0.01	0.97 ± 0.01	P4D1*	0.90 ± 0.02	0.56 ± 0.01
P2D2	0.89 ± 0.01	0.72 ± 0.01	P4D2*	0.90 ± 0.02	0.56 ± 0.01
P2D3	0.92 ± 0.01	0.66 ± 0.01	P4D3*	0.90 ± 0.02	0.57 ± 0.01
P3D4	0.93 ± 0.01	1.02 ± 0.01	P4D4*	0.90 ± 0.02	0.55 ± 0.01
P5D2	0.92 ± 0.01	0.73 ± 0.01	P4D5*	0.90 ± 0.02	0.55 ± 0.01
P5D4	0.92 ± 0.01	0.98 ± 0.01	P5D1*	0.90 ± 0.02	0.55 ± 0.01
P6D2	0.90 ± 0.01	0.68 ± 0.01	P7D1*	0.90 ± 0.02	0.56 ± 0.01

*Natural Detector

Section 4.2: Low-Energy Calibration

A 0.3 μCi ^{228}Th source was used for energy-scale calibration. Calibration of low-energy data was particularly challenging because of the lack of statistically significant spectral lines below the ^{212}Pb 238 keV peak. This section will discuss the calibration procedure and address the methods used to verify and correct the calibration in the low-energy analysis region of interest, 5–100 keV.

4.2.1: MJD Energy-Scale Calibration

Digitized waveform output undergoes data processing before the analysis tools can calculate physical event parameters, including event energy. The ORCA DAQ (section 3.3.3) stores the raw waveform digitizer output in ORCA xml-format files. An event builder reads the raw output, ports meta-data from the file header, and reconstructs the waveform data from the raw binary. Records from multiple channels produced close in time are grouped into the same event. The event builder output, stored in ROOT [163] files, is designated as 'built' data. Digital signal processing of the built data is performed using the 'Majorana-Gerda Data-Objects' (MGDO) [164] package. The raw and built data sets are large and analyzing

them is CPU-intensive so the built files undergo further processing with the 'Germanium Analysis Toolkit' (GAT) to extract waveform parameters of interest, e.g. energy and timing values. The datas encapsulated in GAT processed files are convenient for front-end including histogramming and higher level analyses.

Event energies are determined from charge-pulse waveforms convolved with a trapezoidal filter. A trapezoidal filter is any filter that transforms a waveform into a trapezoidal shape, see for example, [165]. The trapezoidal filter requires two parameters, the ramp-time (t_{ramp}) and the flat-top time (t_{flat}). The width of these timing windows affect the output shape: a shorter ramp-time results in a steeper sloped trapezoid, a longer flat-time results in a wider trapezoid. The total shaping time is,

$$t_s = 2 \times t_{ramp} + t_{flat} \ .$$

The shaping time can be optimized to improve resolution, see section 2.3.1. For DS0,

$$t_{ramp} = 4.0 \ \mu\text{s} \ ,$$
$$t_{flat} = 2.5 \ \mu\text{s} \ ,$$

was used for all detectors. The 10.5 μs shaping time was chosen because it's roughly half of the waveform 2020 ns time window (the last 10 ns bin is neglected). In the future, these values will be optimized for individual detectors.

The height of the trapezoidal output corresponds to the energy of the charge pulse. The charge-pulse decays with a characteristic time constant given by the RC constant of the preamplifier feedback loop, roughly 72 μs. A pole-zero correction is applied to each waveform to reduce undershoot on the leading edge of the trapezoid, which can distort the overall shape. Initial analyses of the DS0 energy-spectrum took the maximum value of the trapezoidal filtered waveform as the energy estimate. It was later determined that the maximum is positively biased because of noise fluctuations in the waveform, especially

at lower energy where the signal to noise ratio is smaller. For the low-energy analysis, the energy is estimated by measuring the filtered value at a fixed time 6 μs after the start (t_0) of the trapezoidal rising edge (i.e the trailing edge) [96].

The initial, raw energy values are in arbitrary ADC units, and depend on the timing parameters. A linear calibration is applied to attain the energy-scale in units of keV,

$$E = aE_{\mathrm{ADC}} + \tilde{E}_0 \text{ [keV]} , \tag{4.1}$$

where a is the energy-scale calibration and $\tilde{E}_0$ is the offset parameter. Using a ^{228}Th line source, the measured ADC energy values can be compared to known full-energy γ-ray peaks. The following peaks were used for DS0 calibration: 238 keV ^{212}Pb, 583 keV ^{208}Tl, 727 keV ^{212}Bi, 860 keV ^{208}Tl, 1512 keV ^{212}Bi, and 2614 keV ^{208}Tl. Calibration constants are extracted via a linear regression of E vs E_{ADC} for each detector in Module 1. A ^{228}Th calibration spectrum from DS0 data is shown in figure 4.3.

4.2.2: Correcting the Low-Energy Calibration

Energy estimation errors in the calibrated DS0 low-energy spectrum arise from both extrapolation of equation 4.1 below 238 keV and from digitizer non-linearities. Previous HPGe experiments avoided extrapolation errors by including x-ray peaks from the cosmogenically activated germanium isotopes (^{68}Ge, ^{65}Zn, and ^{55}Fe) in their calibration fit, see table 4.2. With 478 kg d of exposure, the x-ray peaks in the enriched detector background weren't significant enough to use for calibration. Extrapolation errors in DS0 were instead corrected by including a zero energy estimate in the calibration fit. Measurements of the digitizer non-linearities were taken to reduce errors associated with the non-linearity. An additional fit of the residual calibration error was measured to estimate the remaining scale uncertainty.

The biggest problem faced when correcting the low energy calibration is the lack of statistically significant peaks below 100 keV. To avoid this problem, a high statistics calibration

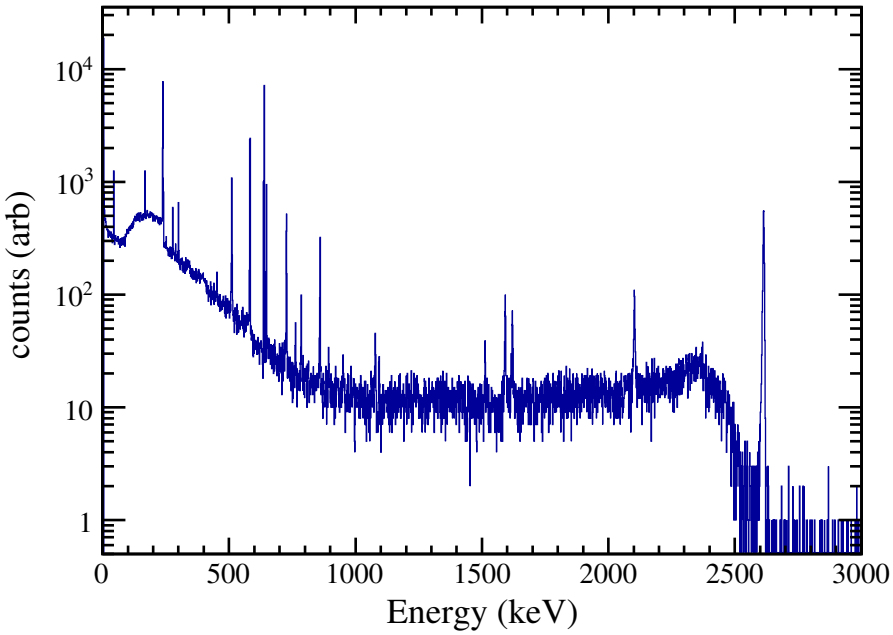

Figure 4.3: An example of a ^{228}Th calibration spectrum used for energy-scale calibration of Module 1 DS0 data. A reference for thorium decay chain γ-ray peaks can be found on the NNDC chart of nuclides [166].

spectrum was generated by summing the data from the 13 physics analysis detectors over all DS0 calibration runs. Additional low-energy thorium chain x-ray peaks were revealed. These peaks, along with cosmogenic peaks in the natural spectrum were used to correct and validate the energy scale below 100 keV.

Prior to November 2015, summing spectra from multiple detectors resulted in peak smearing at low energy. This was noticed while attempting to measure the 10.36 keV ^{68}Ge peak

Table 4.2: List of common cosmogenic isotopes in Ge. The total x-ray energy results from the subsequent cascade of electron de-excitations following the nuclear decay.

Isotope	**Peak Energy**	**Description**
^{3}H	18.6 keV*	β-decay spec.
^{68}Ge	10.36 keV	K-shell x-ray
^{68}Ga	9.66 keV	
^{65}Zn	8.98 keV	
^{55}Fe	6.54 keV	

*Endpoint energy

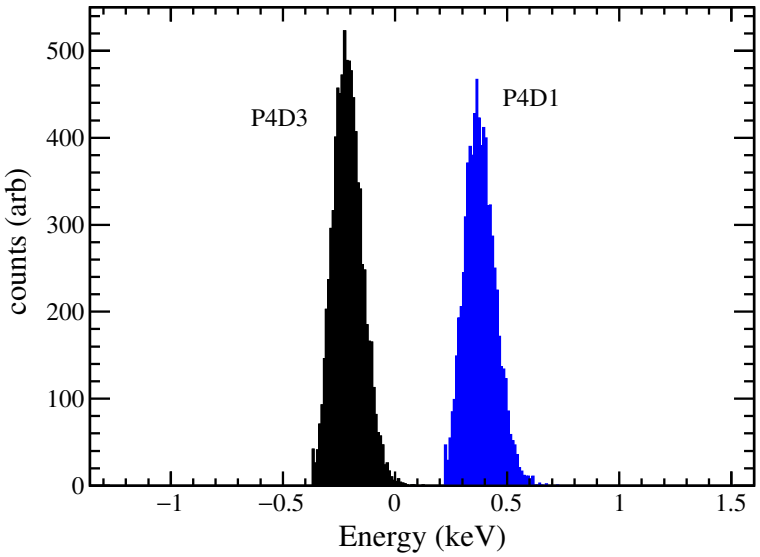

Figure 4.4: Histograms of the measured noise energies for detectors P4D1 and P4D3 before inclusion of the noise peaks in the calibration fit (equation 4.1). If the detectors were calibrated perfectly, the peaks should align at zero. The error in the offset is the cause of the peak smearing shown in figure 4.5.

after summing the natural detector background spectrum. Due to extrapolation errors, the x-ray peaks in the individual detector spectra were offset relative to each other. At < 10 keV, peaks were offset by roughly 0.2-0.5 keV. Including the zero-energy point in the calibration fit fixed the offset mismatch between the detectors. The zero energy point was estimated from the measured ADC energy value of baseline noise data. This data was generated by forcing random DAQ triggers. A comparison of the noise peaks taken during a September 2015 characterization run is shown in figure 4.4. Including the so-called zero-energy noise peak into the calibration fit reduced the offset error by more than an order of magnitude, and improved the summed spectrum resolution in figure 4.5.

The digitizer non-linearity introduced a bias that shifted energy estimates downward. An initial estimate of the digitizer non-linearity was obtained by comparing the calibration spectra from the high-gain (unattenuated) and low-gain (attenuated) channels, see figure 4.6. A digitized triangle wave was used to measure the non-linearity of the Gretina cards. The change in the ADC value as the voltage was incremented by a set unit was recorded and

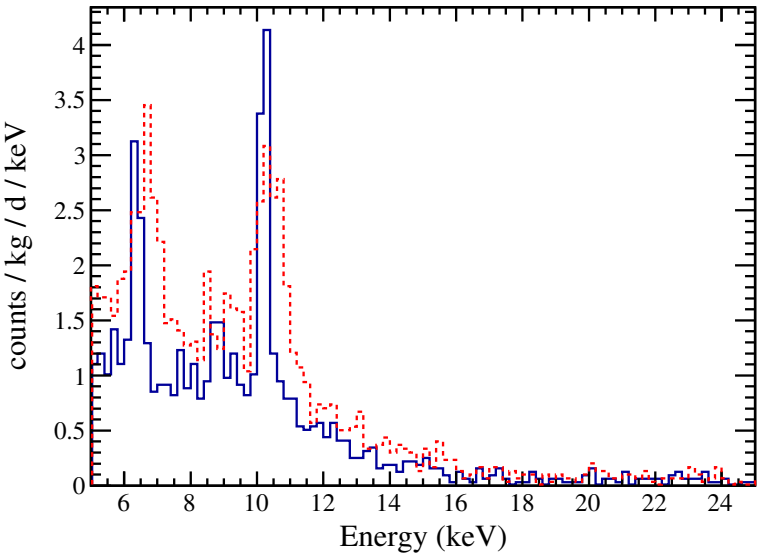

Figure 4.5: Summed natural detector spectra with 195 ± 3 kg d of data. The red dashed spectrum was taken before the offset correction. The blue spectrum shows the improvement resulting from the inclusion of the noise peak in the calibration fit. The offset correction reduces the smearing due to misaligned peaks, improving the resolution.

binned for each ADC unit. The integral non-linearity was measured by averaging the differential non-linearities of each bin and then integrating over all ADC bins. A sawtooth like pattern of integral-nonlinearities occurs across the ADC bins [167]. A table of the measured integral and differential non-linearity values as a function of ADC was used to correct the non-linearity error during energy calibration.

Residual non-linearities still introduced energy estimation errors after the correction was applied. An additional linear adjustment was applied to correct the low-energy calibration. A multi-peak fitting routine was used to measure the peak centroids of the low-energy thorium chain peaks in the summed calibration spectrum. The fit centroids were then compared to the known energy values. Table 4.3 shows the measured centroids and their deviation from the true value.

The residual values and their uncertainties in table 4.3 were used to compute a shift to

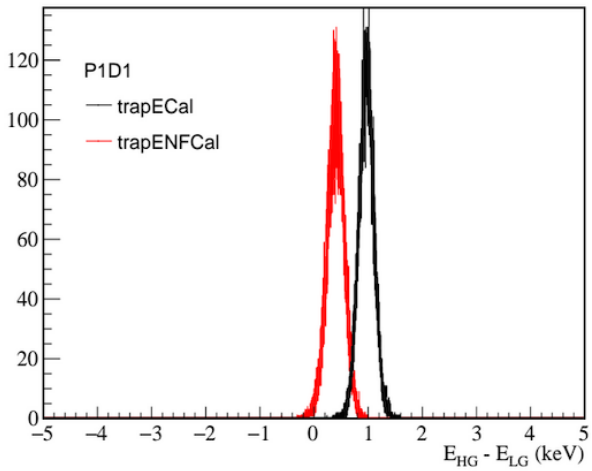

Figure 4.6: Distribution of the energy-scale difference between the high-gain and low-gain channels between 5-100 keV for detector P1D1. A non-linearity correction is not applied to the energy parameter 'trapECal' (black), while a correction is applied to the 'trapENFCal' parameter. Residual non-linearities persist, and must still be accounted for. Figure from [96]

the summed spectrum energy estimate:

$$\Delta E(E) = \alpha_E(E - E_{\text{center}}) + E_0 \ . \tag{4.2}$$

Here α_E is the fit scale adjustment and E_0 is the fit offset correction. To minimize the correlation between the two parameters, the fit was centered around the constant, $E_{\text{center}} = 95.0$ keV. From the fit, $\alpha_E = -0.0014 \pm 0.0008$, $E_0 = -0.256 \pm 0.016$ keV, and $\text{corr}(\alpha_E, E_0) = -0.22$ keV. In the likelihood analysis (chapter 6), the shift wasn't applied to the summed spectrum directly, but was instead added to both the bosonic dark matter mass and ^{68}Ge x-ray energy nuisance parameters.

For a rough validation of the residual non-linearity correction given by equation 4.2, the multi-peak fitter was applied to the cosmogenic lines in summed background spectra of the natural detectors. The predicted shift at the ^{68}Ge 10.36 keV k-shell peak from equation 4.2 is -0.12 ± 0.07 keV. The measured peak centroid was 10.22 ± 0.06 keV, which is offset by roughly -0.14 keV and is consistent with the predicted value.

Table 4.3: Low energy x-ray lines used to test energy calibration. A multi-peak fitting routine was applied to the sum of the spectra for the 13 analysis detectors across all the calibration runs. The centroid values were compared with ^{228}Th chain x-rays and γ-rays.

X-ray	**Peak Energy (keV)**	**Measured Energy (keV)**	**Residual (keV)**	**Res. Unc. (keV)**
Bi $K_{\alpha 2}$	74.815	75.04	-0.22	0.09
Bi $K_{\alpha 1}$	77.107	77.36	-0.25	0.03
^{228}Th*	84.373	84.7	-0.3	0.10
Bi $K_{\beta 3}$	86.830	87.0	-0.2	0.10
Bi $K_{\beta 1}$	87.349	87.59	-0.24	0.06
Bi $K_{\beta 1}$	89.784	89.97	-0.19	0.06
^{212}Pb*	115.183	114.90	-0.29	0.02

*γ-ray

4.2.3: The DS0 Low-Energy Spectrum

The calibrated energy-spectrum used for the dark matter analysis is shown in figure 4.7. The extrapolation error correction and non-linearity correction have been been applied. The residual bias shift, equation 4.2 is not applied to the full spectrum. Details of the data cleaning cuts applied to produce this spectrum are saved until chapter 5. The total analysis exposure is 478 $\pm$ 6 kg d. Also shown is the total energy-spectrum from 185 $\pm$ 3 kg d of natural detector exposure used for systematic checks. The natural detector spectrum shows events from all of the cosmogenic backgrounds listed in table 4.2. In the enriched spectrum, the 10.36 keV peak is discernible, along with an excess below 20 keV that is attributed to tritium in the final analysis. Error bars on the bins encapsulate both the poisson uncertainty in the count rate along with the exposure uncertainty.

Section 4.3: Resolution Measurement

Understanding the resolution at low energy is critical for the bosonic dark matter and other physics analyses. A finer resolution results in greater sensitivity to rare events that manifest as mono-energetic peaks. In addition to calibration challenges covered in section 4.2, the lack of sharp peaks in the ^{228}Th calibration spectrum introduces obstacles during charac-

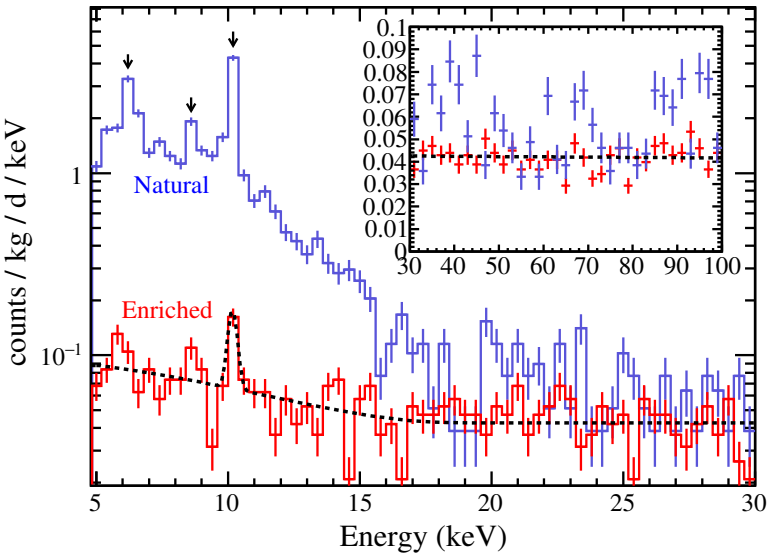

Figure 4.7: The DS0 low-energy spectra from 185 ± 3 kg d of data from the natural detectors (blue) and 478 ± 6 kg d of enriched detectors (red). Error bars show the poisson uncertainty in the rate coupled with the uncertainty in the live-time. The dashed black curve shows a fit of a tritium spectrum + 10.36 keV ^{68}Ge peak + linear background fit to the enriched data. Inset: Spectra above 30 keV.

terization of the resolution below the 238 keV ^{212}Pb line. In order to estimate the resolution below 100 keV as a function of energy, the summed enriched calibration spectrum is used. This section will discuss resolution curve fitting and uncertainty estimation.

4.3.1: Fitting the Resolution below 100 keV

The resolution parameters (FWHM/2.355) for each peak fit in the multi-peak fitter can be extracted and fit to the resolution curve:

$$\sigma_E(E) = \sqrt{\sigma_e^2 + \langle\varepsilon\rangle F E} \tag{4.3}$$

where E is the energy in keV and the fit constant $\langle\varepsilon\rangle = 2.96$ eV is the average energy required to produce an electron-hole pair in Ge. The fit parameter, σ_e, is the electronic noise contribution to the energy resolution and F is the Fano factor. At low energy, the

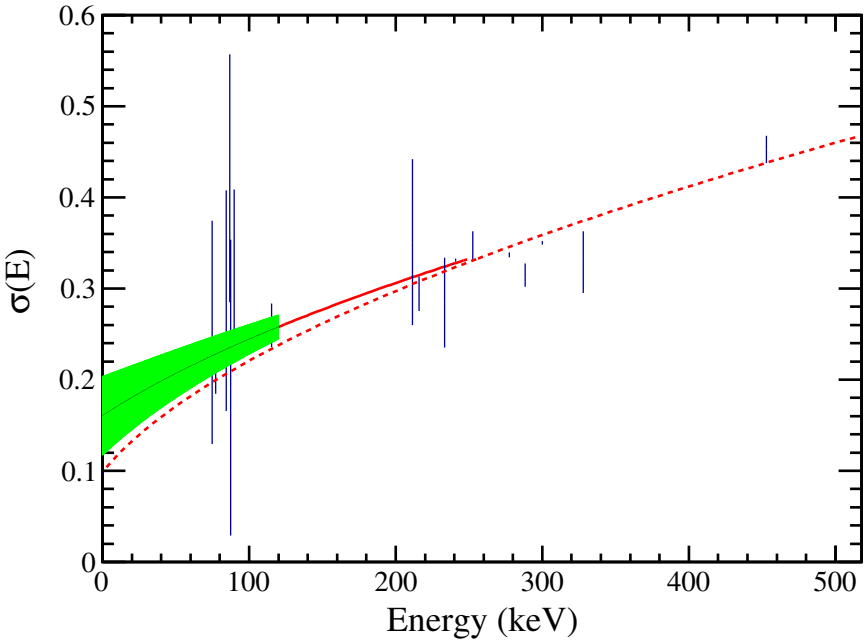

Figure 4.8: The resolution fit function, equation 4.3. The solid curve, ranging from 1–250 keV, is the function used in the analysis. The dashed curve is a fit from 0–3000 keV. The green 68% confidence band was generated to estimate the uncertainty on σ_E.

resolution component associated with charge collection is neglected. For further discussion of the resolution function, see section 2.3.2.

There is some peak broadening that occurs because of spectral summing from multiple detectors. While this effect is reduced due to the inclusion of the zero-energy peak in the calibration fit, residual offsets persist. This effect is more significant at lower energies since the ratio of the relative offset to the individual detector resolution is larger than at higher energies. The offsets are roughly 0.05 keV compared to 0.6 keV FWHM at 10.3 keV and 2.0 keV FWHM at 1333 keV. Since the resolution curve is computed for the summed enriched spectra and not for each individual detector, the range of the fit was restricted to 1–250 keV in order to capture the resolution degradation resulting from offset smearing.

4.3.2: Resolution Fit Parameters

Two fits of the resolution (FWHM/2.355) as functions of energy are shown in figure 4.8, a restricted-range fit, and a full-range fit. The full range fit predicts a better resolution at lower energy than the restricted-range fit. To be more conservative with low-energy physics sensitivity of MJD, the resolution is estimated from the restricted range. The resolution of the baseline noise peak (zero-energy) was excluded from the restricted-range fit because it pulled the resolution curve down, and introduced a 4σ inconsistency between the predicted and measured values of $\sigma_E(E)$. From the fit, $\sigma_e = 0.16 \pm 0.04$, $F = 0.11 \pm 0.02$. The fit parameters were fully correlated, $\text{corr}(\sigma_e, F) \sim 1$. A 68% confidence belt was computed for $\sigma_E(E)$, based on the fit uncertainties of σ_E and F. The confidence belt is used to constrain the resolution in the likelihood analysis.

To validate the curve prediction at lower energies, a gaussian + linear function was fit to the 10.36 keV peak in the summed enriched background data. This peak was not included during function fitting. The σ_E(10.36 keV) value was 0.20 ± 0.05 keV. The predicted value from the fit excluding the noise peak was 0.17 ± 0.04 keV, which is consistent with the measured value.

Section 4.4: Summary of Systematic Parameters

Systematic parameters required for the bosonic DM analysis were introduced in this chapter. The exposure, energy calibration, and resolution are key parameters needed to constrain the signal contribution from dark matter and other exotic physics. The systematic uncertainties are used to limit the parameter space of floating values in the likelihood analysis in chapter 6. A table of systematic parameters is give below.

Table 4.4: Systematic parameters and uncertainties used in the DS0 bosonic dark matter analysis energy estimation.

Parameter Description	**Value**	**Unit**
Enriched Exposure	478 ± 6	kg d
Natural Exposure	185 ± 3	kg d
Cal. Gain Correction (α_E)	-0.0014 ± 0.0008	$\sim$
Cal Offset Correction (E_0)	-0.256 ± 0.016	keV
Cal. Fit Center (E_{center})	95	keV
corr(α_E, E_0)	-0.22	$\sim$
Electronic Noise (σ_e)	0.16 ± 0.04	keV
Fano Factor (F)	0.11 ± 0.02	$\sim$
corr(σ_e, F)	1	$\sim$

CHAPTER 5: Data Cleaning

This chapter will discuss low-energy data cleaning. Detector surface events and electronic noise produce spurious counts in the low-energy spectrum. Waveform discrimination methods and data cleaning techniques have been developed to identify and remove these events. Wherever data cleaning cuts are applied, the impact on the physics data of interest will be quantified.

Section 5.1: Surface Event Removal

As discussed in chapter 2, surface events produce energy degraded pulses in PPC detectors with long rise times. These events, referred to as slow pulses, constitute a major background in low-energy HPGe experiments [53, 92]. Slow pulses are a result of incomplete charge collection from energy depositions in detector regions where the drift velocity is diffusion dominated. Previous experiments have tagged slow pulses by measuring the $t_{10-90\%}$ rise-time of charge pulses or by applying wavelet de-noising. Rise-time measurements become increasingly difficult with decreasing energy due to the reduction of the signal-to-noise ratio. A more robust slow-pulse tag can reduce unwanted backgrounds.

5.1.1: The T/E parameter

The T/E parameter was developed as an alternative to rise-time measurements for slow-pulse tagging. The inspiration for the T/E parameter comes from the A/E parameter used by both the GERDA [104, 132] and MAJORANA collaborations [110] for pulse-shape discrimination and multi-site event tagging. The parameter T is defined as the maximum

value of the triangle-filtered[1] charge waveform. T is scaled by the waveform energy E, producing the T/E value, to break the pulse-height energy-dependence. The effect of the triangle filter is shown in figure 5.1.

A triangle filter is applied to charge-pulse waveforms via discrete function convolution. The functional form of the triangle filter is similar to a high-pass Haar wavelet [168]:

$$\Delta_{\text{filter}}(t) = \begin{cases} \frac{1}{2a} & -a \leq t < 0 \\ -\frac{1}{2a} & 0 \leq t < a \\ 0 & \text{Else} \end{cases} \tag{5.1}$$

where a is the ramp time of the filter. The filter is normalized by the shaping time, equal to twice the ramp time. Triangle filter shaping-time parameters were chosen to optimize the slow-pulse discrimination capability of the T/E parameter. A gap-time of 10 ns, corresponding to the Gretina card timing resolution was added to the filter. The triangle ramp-time was set to 100 ns based on A/E tuning performed by the MAJORANA run selection and data cleaning group [169]. Increasing the ramp-time decreases the discrimination power of T/E. Decreasing the ramp time increases the susceptibility to high frequency noise: at very low energy (<3 keV for 100 ns ramp) the T/E cut breaks down because $T \rightarrow$ const., so that $T/E \propto 1/E$. This breakdown happens at higher energies with shorter triangle ramp-times.

The T-value will be maximal when the shaping time is greater than the charge-pulse rise time. If the shaping time is less than the rise time, the full charge difference is never completely covered during the convolution, resulting in a degraded filtered-waveform maximum. This principle can be used to distinguish slow-pulses from fast-pulses. Figure 5.2 shows the effect of a triangle filter with 100 ns ramp time on both a slow and fast waveform.

A simple threshold was set on the T/E value to differentiate between slow pulses and

[1]The trapezoidal filter, discussed in section 4.2, becomes a triangle filter as the flat-top time approaches zero.

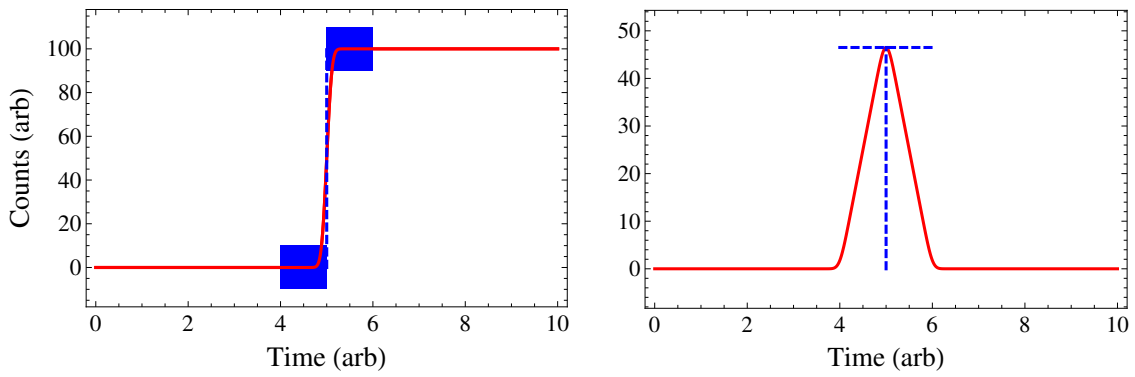

Figure 5.1: Left: A snapshot of the application of a triangle filter to an idealized charge waveform modeled with an error function at the time of maximal difference. The blue boxes represent the two averaged timing windows. Right: Convolution of the triangle filter and the waveform. The T value is the maximum value of the filtered waveform. Scaling by the trapezoidal energy estimate produces the T/E parameter.

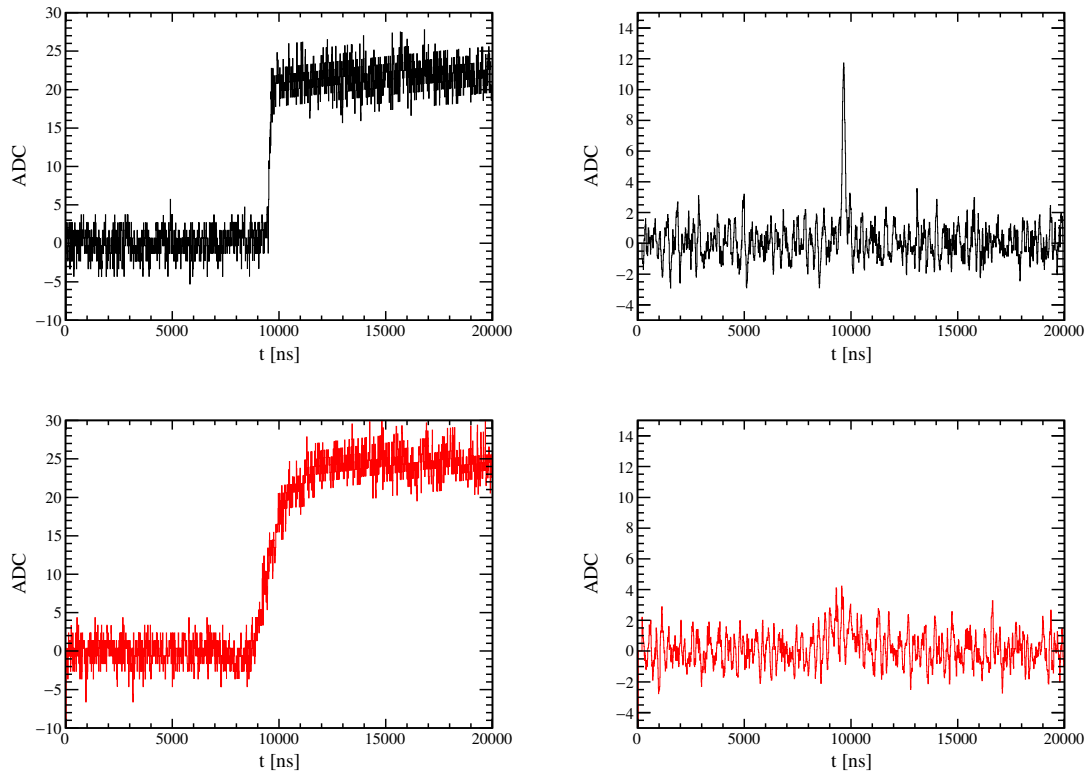

Figure 5.2: The effect of the triangle filter with 100 ns ramp-time on fast and slow pulses of similar energies. Top: A fast charge pulse with energy ∼8 keV (left) and the filtered response (right). Bottom: A slow charge pulse with energy ∼9 keV (left) and corresponding response (right). There is a clearly discernible triangle peak in the plot on the top right, with a maximum value of ∼12. The maximum value of the filtered slow pulse is < 4.

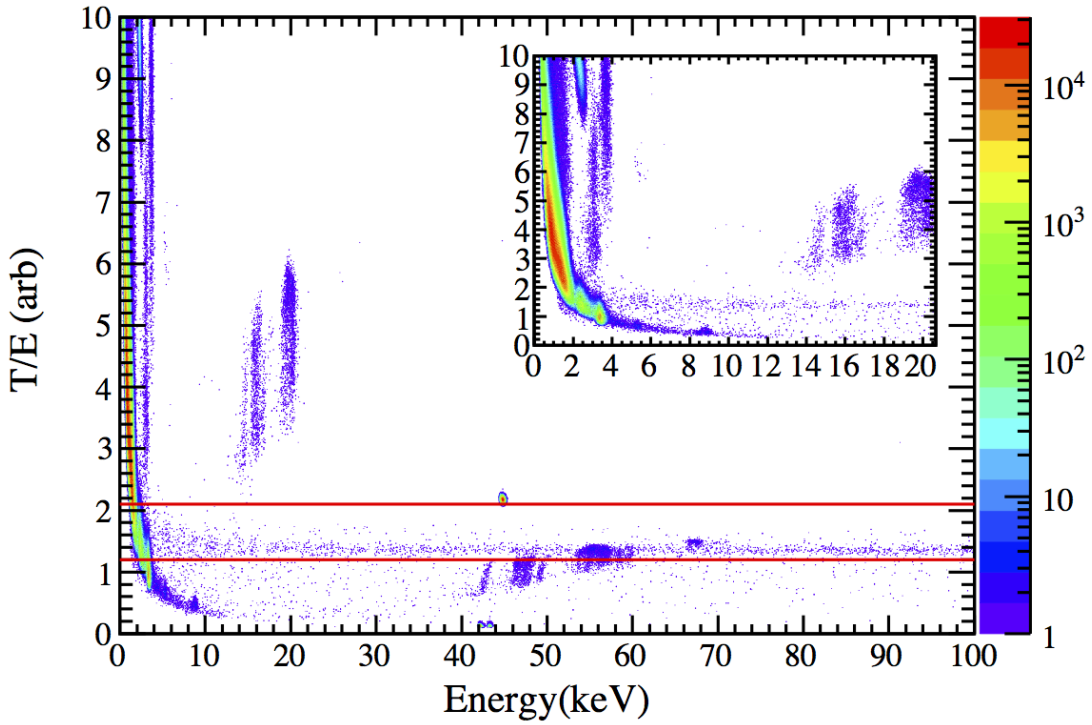

Figure 5.3: A 2-D histogram of T/E vs E from 250 kg d of the 13 enriched DS0 detectors without any data cleaning applied. Events between the red lines ($T/E = \{1.2,\ 2.1\}$) are accepted by the T/E cut. Events below the bottom red line are either slow pulses or electronic noise. At very low energy, < 5 keV, pulser-retriggering events dominate the spectrum. The spurious blobs result from transient micro-discharge events and pulser ringing.

fast pulses. At higher energies, $\gtrsim 50$ keV, the number of slow pulse events is significantly reduced. The >50 keV region can be useful for tuning the T/E cut thresholds. For DS0, events outside the $1.2 < T/E < 2.1$ window rejected. Care was taken to avoid cutting too aggressively because the T/E distribution broadens slightly at low energies as the signal to noise ratio decreases. A plot of the T/E vs E without any data cleaning from the first 250 kg d of DS0 background data is shown in figure 5.3. Characterization of the T/E physics event acceptance is saved for section 5.3 because a subset of the electronics noise events is found within the parameter region of interest, particularly between 40-70 keV and below 5 keV. A data cleaned version of the T/E vs E plot is shown in figure 5.8.

Section 5.2: Electronic Noise Removal

At low energy, electronic noise dominates the event rate. In the raw spectrum, there were $\mathcal{O}(10^8)$ events (mostly below 5 keV) while in the data-cleaned spectrum there were $\mathcal{O}(10^3)$ events. The vast majority of these events fell into two categories, pulser-retriggering events and transient micro-discharge events. An example of each is shown in figure 5.4. Specific waveform tags were developed to handle both cases.

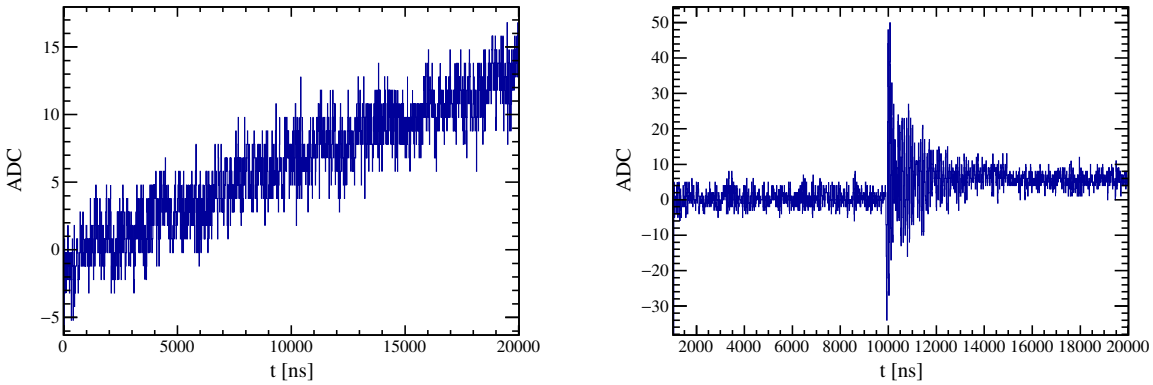

Figure 5.4: The two types of (baseline subtracted) electronic noise that dominate the event rate at low energy. Left: Pulser retrigger events. The digitizer triggers on the recovery of the electronic pulser, resulting in an upward going pulse. Right: Transient micro-discharge / pulser ringing event.

5.2.1: Tagging and Removing Pulser-Retriggering Events

As discussed in section 4.1.2, an internal electronic pulser is used for live-time validation, ensuring that the detectors are live for the full duration of data taking. Ringing associated with pulsers on various digitizer channels triggers waveforms that undershoot the baseline. If a channel's threshold is too low, the Gretina card will trigger as the undershoot decays to the baseline. This produces the rising pulses shown in figure 5.4, denoted pulser-retriggering events.

Retriggering events can be identified by their rising waveform tail, defined here as the section of the waveform in the 1 - 2 μs time domain (i.e. the right half). Charge-pulse

waveforms generated by physics events exhibit a falling tail due to the pulse decay through the feedback resistor. The ideal technique for discriminating retrigger waveforms is finding the average value of the derivative the tail, i.e the average slope. During DS0 analysis, an average tail slope parameter was not available in the GAT-processed dataset (described in section 4.2), and adding parameters to the dataset took multiple months. Because of the parameter availability, a related method taking advantage of the minimum value of trapezoidal-filtered waveforms was instead utilized.

The trapezoidal filter described in section 4.2 is sensitive to the rise and decay of waveforms. Convolving a charge-pulse waveform with a trap-filter produces a trapezoidal shape, however the falling waveform tail causes a slight undershoot in the post-filtered waveform. In contrast, pulser-retrigger waveform tails generally increase monotonically; convolving them with a trap-filter does not produce tail undershoot. Using this principle, the minimum of the trap-filtered waveform, 'trapMin', can discriminate between physics and pulser-retrigger events. Charge-pulse waveforms are generally characterized by negative 'trapMin' values. Pulser-retrigger waveforms are tagged by searching for 'trapMin' values of zero or above. See figure 5.5.

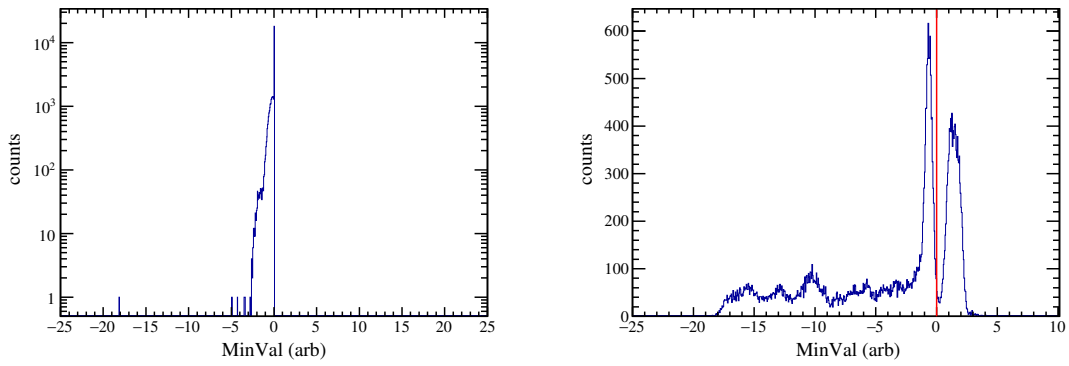

Figure 5.5: Distribution of the old (left) and the improved (right) trapezoidal min parameters from 15.4 kg d of P7D1 data. The old parameter measured the minimum over the full time-domain of the filtered waveform and was always ≤ 0. The improved parameter searched for the minimum in the tail of the non PZ-corrected filtered waveform. Events with MinVal ≥ 0 are rejected.

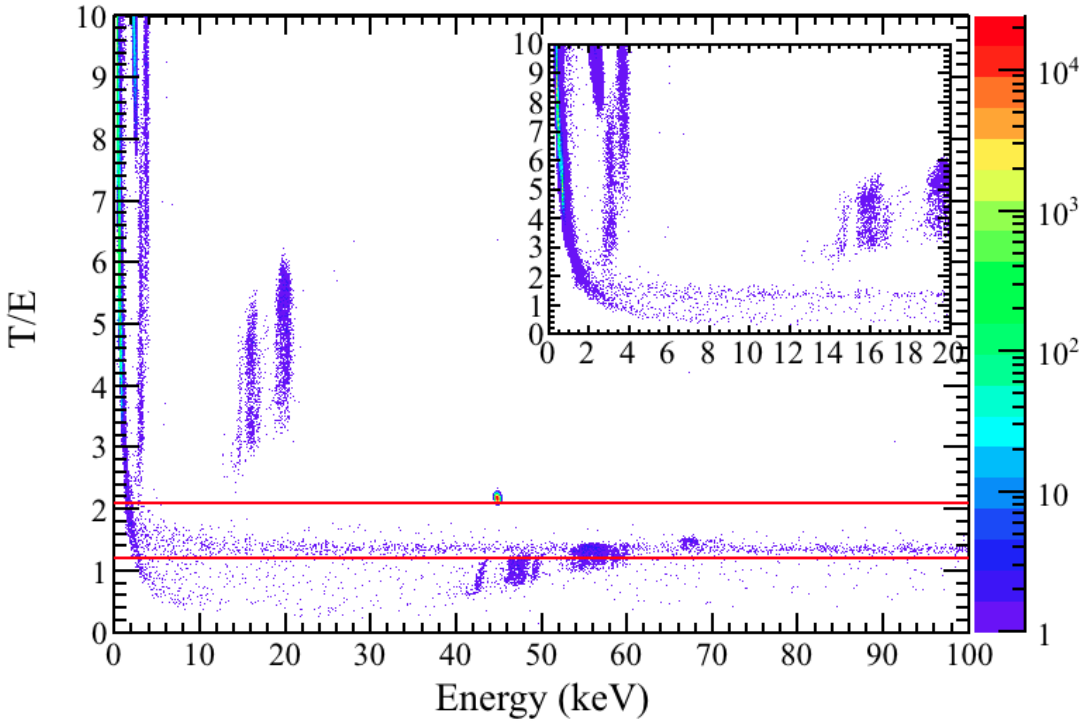

Figure 5.6: The effect of the trapezoidal filtered minimum parameter on the T/E parameter vs energy. Events with non-negative minimum values have been removed. The total number of events in this figure is 2.1×10^6 compared with 5.6×10^7 in figure 5.3, a 96% reduction.

The originally available trapMin parameter misidentified too many physics waveforms as retrigger waveforms because pole-zero correction reduced or eliminated the post-filtered undershoot. Two changes were made to the trapezoidal minimum parameter to reduce the mixing between pulser-retriggering events and physics events in the cut parameter space. First, the extremum finder used to find the minimum was confined to the upper half of the waveform time-domain, >10 μs. This eliminated the zero upper bound on the trapMin parameter that was due to the implementation of the trapezoidal filter in MGDO. Second, trapezoidal filtering for the trapMin parameter was applied without applying a pole-zero correction to waveforms, enhancing the trapezoidal undershoot. The overall result was much better separation between physics and retrigger waveforms in the trapMin parameter space; see the example in figure 5.5.

Events with trapMin > 0 are cut from the analysis. Noise event reduction from pulser retriggers are well illustrated in the T/E vs. E plot. A data cleaned version of the T/E vs E plot is shown in figure 5.8. The trapMin cut reduced the number of 0-100 keV events in figure 5.3 by roughly 96%, see figure 5.6. Most of the events removed from the trapMin cut are either outside the accepted T/E space or outside the 5 - 100 keV analysis region of interest. Further analysis of the event reduction is saved for section 5.3.2. The remaining noise events in figure 5.6 are transient events, shown on the right in figure 5.4, and require a separate cut method.

5.2.2: Transient Pulse Identification and Removal

Transient event pulses are characterized by high frequency bursts. This causes their elevated T/E values, shown in figure 5.6. Burst events are less well understood than the pulser-recovery events discussed in section 5.2.1. They originate from a wide variety of sources, including pulser-ringing due to impedance mismatching in electronics chain, HV breakdowns in cabling. Many of these events appear in both the T/E acceptance space and the 5 - 100 keV analysis window.

Developing an efficient transient event tag with the available parameters in the GAT processed data set during DS0 analysis proved to be quite challenging. A frequency analysis, such as a Fourier transform may have provided an effective tag, but such tools were unavailable at the time. The best available option was a raw waveform minimum parameter, originally included in the GAT data to tag digitized waveforms with dead bits. A plot of minimum raw waveform value vs energy is shown in figure 5.7. Some bursts with features undershooting the baseline can be tagged. Setting a minimum raw waveform value threshold to fully separate physics and burst events was not possible. Physics events were incorrectly tagged if the minimum value threshold was too high. The efficiency of the transient tag was was poor if the minimum value threshold was set too low. During tag optimization trials, the highest achieved transient tagging efficiency with the minimum value parame-

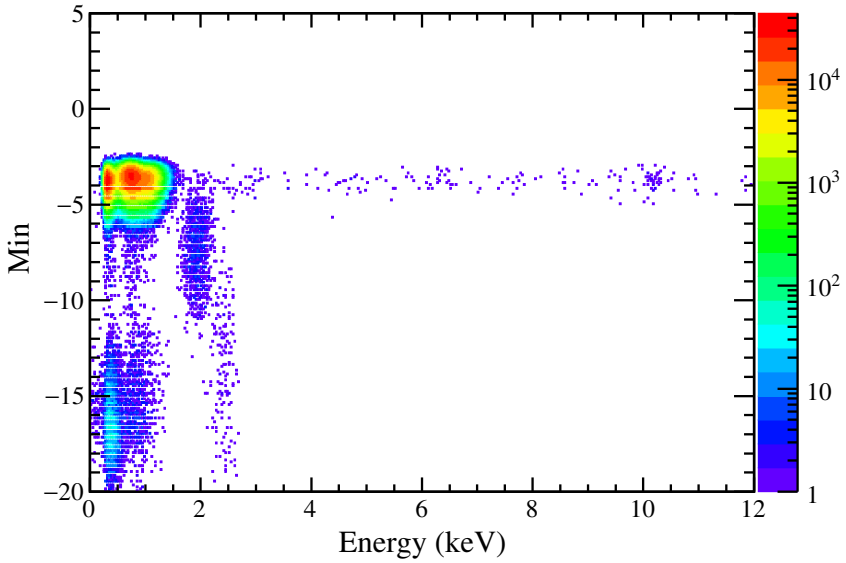

Figure 5.7: Minima from 15.4 kg d of P7D1 data. Values on the y-axis are in arbitrary units. For this detector, the transient noise pulse energy was less than 3 keV. There is some mixing of the transient pulses with the physics pulses near 2 keV.

ter was ∼95%.The untagged burst waveforms were intolerable because their measured T/E parameters were within the acceptance region.

Although an effective transient tag was not developed for the DS0 data, it was still possible to remove >99.9% of the burst events. In September 2015, the MAJORANA detector subgroup discovered excessive sparking associated with the top detector of the position 6 string. Though this detector had already been removed from the analysis because of excessive low-energy events, cross talk associated with the sparking simultaneously triggered multiple channels, including analysis detector channels. Soon afterward, it was found that simply limiting the analysis to single detector events removed nearly all of burst events from the data. A detector multiplicity parameter had been included in the GAT-processed data to study coincident detector events, so this so-called multiplicity cut was quickly implemented. Only events with single detector multiplicity were selected for analysis. A plot of the T/E vs energy with both the pulser-retriggering cut and the multiplicity cut is shown in figure 5.8.

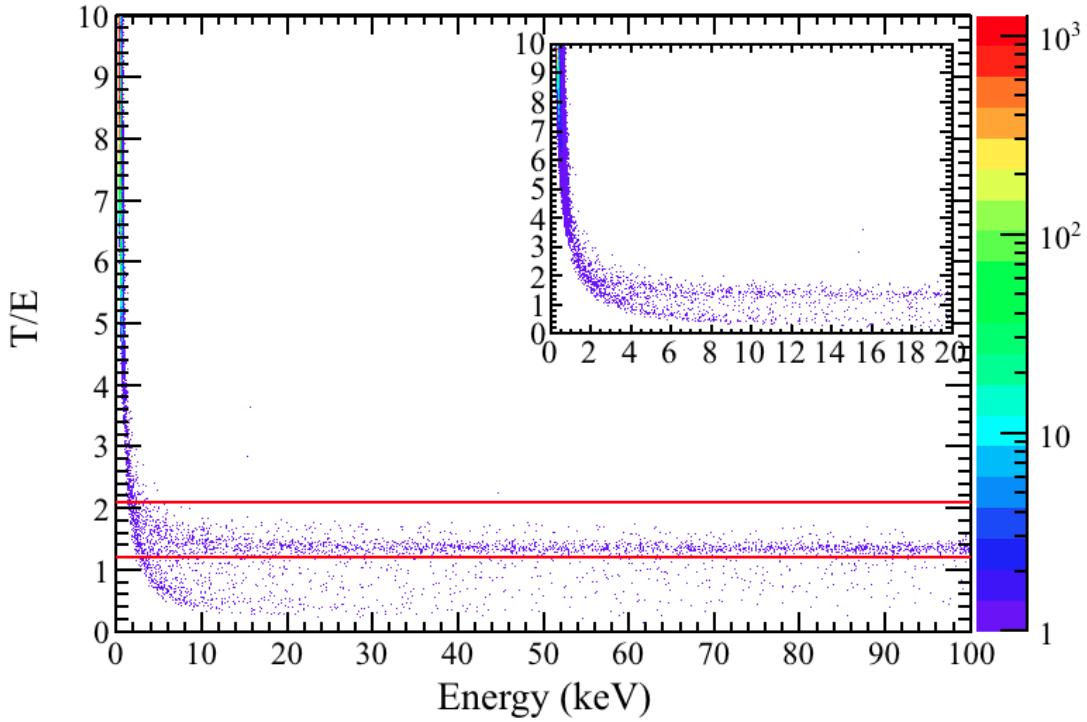

Figure 5.8: The final version of the T/E vs E plot, with virtually all electronic noise removed. The inset shows a zoomed-in region below 20 keV. Slow pulses are removed by only keeping events in the parameter space between the two red lines. The spectrum in figure 4.7 can be generated by projecting all the counts between the red lines onto the energy axis.

Section 5.3: Data Cleaning Efficiency

While each data cut is designed to remove unwanted noise events in the energy spectrum, some physics events will invariably be cut accidentally. Quantifying the acceptance efficiency of each of the three cuts: the multiplicity cut, the retriggering cut, and T/E cut is necessary so that event rate corrections can be applied in the final analysis. It was found that the multiplicity cut and the pulser-retriggering cut have a negligible effect on the DM analysis region of interest, while the T/E cut has a non-negligible effect within the 5 – 20 keV energy range.

5.3.1: Acceptance Efficiency of the Multiplicity Cut

When applying the multiplicity cut, there is a risk that independent events could occur in coincidence (within a 50 μs window) resulting in an accidental cut. This frequently occurs in calibration runs, however the rate in background runs is low enough that this effect is negligible.

The average event rate in all detectors during the DS0 run, including detectors that were not subject to the DM analysis is roughly 25 Hz. By measuring the minimum time between triggers in calibration runs, it was determined that there's a 43 μs dead-time between each trigger [160]. If multiple channels trigger within this window, the event is considered a coincident event and is cut. For the multiplicity acceptance analysis that follows, the dead-time is estimated as a 50 μs event window. Assuming that independent physics events are poisson distributed, the parameter of interest is the probability that a background event will occur within the 50 μs following another event. This is computed by:

$$\mathcal{P}_{coinc} = \sum_{n=1}^{\infty} \frac{\lambda^n e^{-\lambda}}{n!} \tag{5.2}$$

where λ is the expected number of events in a 50 μs window, equal to 25 events/s times 50 μs, or 0.00125 events. The summation evaluates to roughly 0.12%, meaning that 99.88%

of poisson distributed events pass the cut. The high acceptance efficiency of the multiplicity cut is considered negligible, and is neglected in the rare-event physics analyses.

5.3.2: Acceptance Efficiency of the Pulser-Retriggering Cut

The pulser-retriggering cut targets very specific waveforms and has a high acceptance efficiency for events in the 5-100 keV energy window, see figures 5.3 and 5.6. A small fraction of events cut with the trapMin parameter manifest with energies up to 12 keV, but those events also occur outside the T/E acceptance region. Neglecting the retrigger cut entirely was an option, though removing events from the analysis that failed the cut reduced analysis time by a factor of $\sim$10.

The retriggering cut was applied to calibration data to measure the data acceptance rate. Physics events in a calibration run were expected to dominated the event rate. One random calibration run was chosen from each DS0 calibration run period, and the total energy-spectrum was produced. For each detector, the energy-spectrum between 5 – 100 keV was integrated before and after applying the cut. The acceptance efficiency was computed from the ratio of the integral values. An example of the effect of the pulser-retriggering cut on a detector's energy spectrum is shown in figure 5.9.

Figure 5.10 shows the acceptance efficiency for each operating detector during DS0 data collection. The figure shows that most of the events that are removed by retrigger cut are outside the accepted T/E parameter space. Note that fewer events in the 5–100 keV region are rejected in the enriched detectors than the natural detectors. The enriched and natural detectors were manufactured by different companies, ORTEC [87] and Canberra [90] respectively, and have some minor geometrical differences that may be the reason for the difference. For each of the enriched detectors used in the DM analysis, the acceptance efficiency was $> 99.95\%$ for events above 5 keV. The retrigger reduction rate is negligible and is not considered in the final analysis.

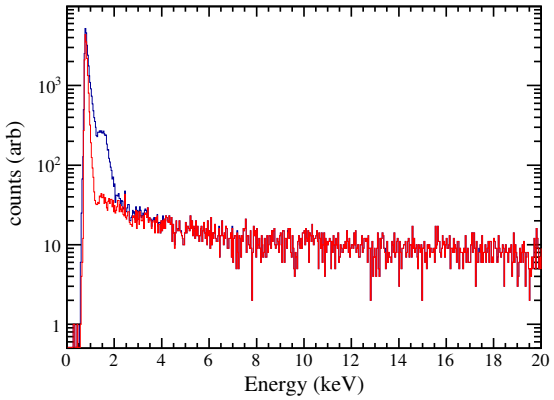

Figure 5.9: The effect of the pulser-retriggering cut (red) when applied to a calibration energy spectrum from detector P1D2 (blue). Both spectra have been subject to the T/E cut described in section 5.1.1. Roughly 90% of events below 4 keV are removed while virtually all events pass the cut above 5 keV.

5.3.3: The T/E-Cut Acceptance Efficiency

Differentiating between slow-pulses and fast pulses becomes increasingly difficult as the signal-to-noise ratio of the charge waveforms decreases. Invariably some fraction of fast pulses will be rejected along with the slow pulses. Determining the fast pulse acceptance as a function of energy requires a pure source of fast pulses that are subject to the same electronics and analysis chain that detection events are subject to.

Pulser generated waveforms were used for T/E-cut acceptance measurements. For five detectors in DS0: P1D3, P2D2, P3D3, P5D2, and P6D3; a jumper in the HV electronics was severed to allow for capacitive coupling of an external pulser input. The P3D3 detector was not considered in this analysis because of issues with spontaneous gain shifts. An Agilent 33220A [170] waveform generator was used to inject pulses to the detector's 2nd-stage preamplifiers.

The injected waveforms were semi-trapezoidal with a ramped rising edge and a square falling edge. The amplitude of the waveforms was kept constant. To vary the energy estimate of the pulses, two high-precision, variable attenuators were used to step down the pulser voltage. A script was written to scan a range of pulser rise-time values in 5 ns increments within

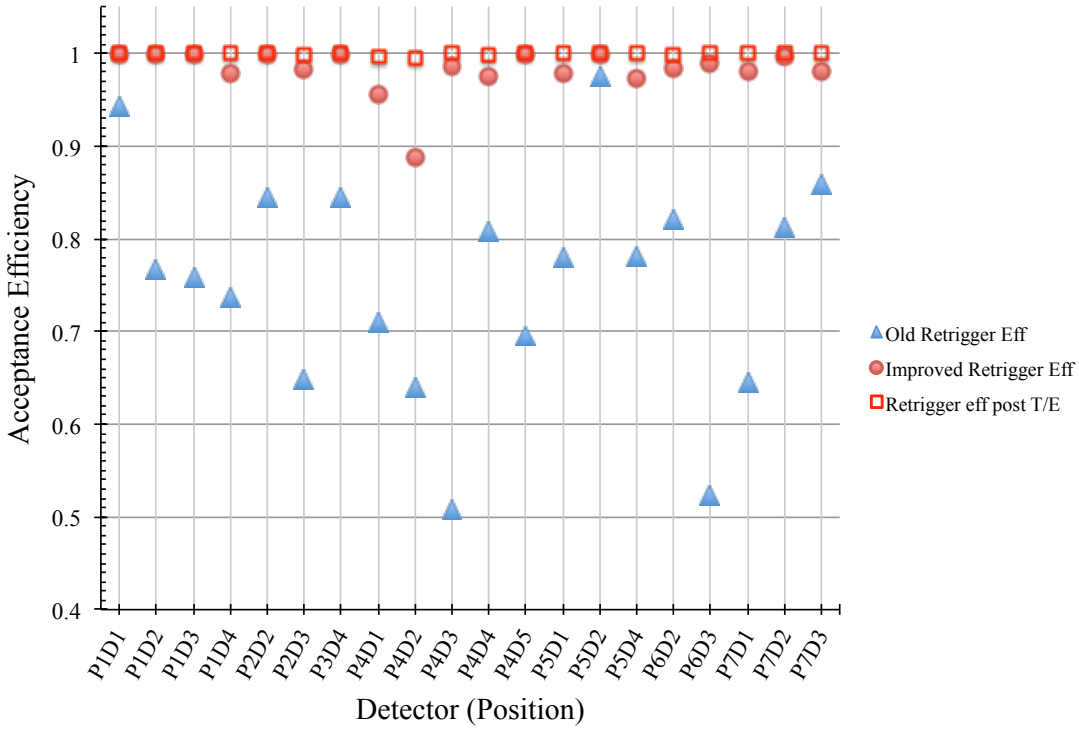

Figure 5.10: The pulser-retriggering cut acceptance efficiency for each detector used in the DM analysis plus the natural detectors (see figure 4.1). The integral of random calibration data energy spectra from 5 – 100 keV was computed with and without the cut applied. The ratio of the two values is shown in the figure. Blue triangles show the efficiency when the minimum is found from the full time domain of the trapezoidal filtered waveform. Red circles show the efficiency when the minimum is found from the tail region (>10 μs) of the waveform. The open squares show the efficiency of events in the accepted T/E parameter space.

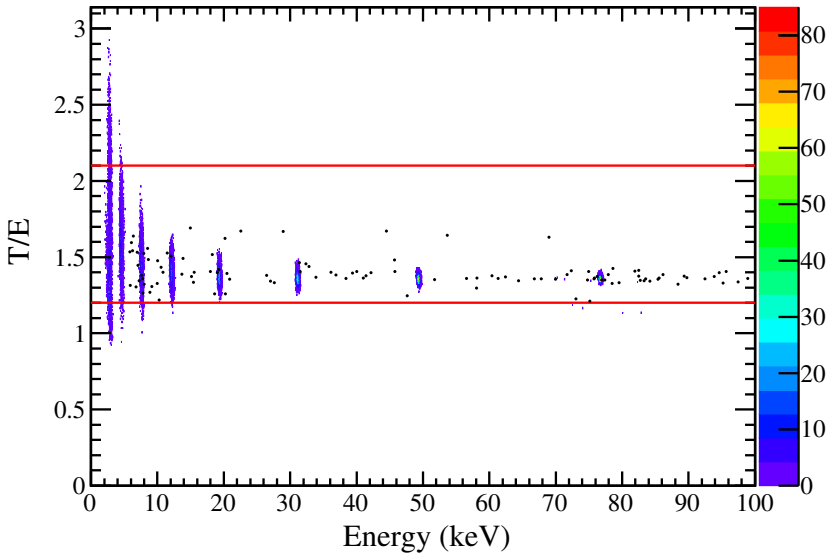

Figure 5.11: Plot of the tuned T/E vs E for external pulser events in P5D2. The blob-like pulser events overlay background events (scattered black dots). The pulser rise-time was tuned over a series of runs so that the T/E of the higher-energy pulser events matched with the T/E of the background events. The red lines show the accepted region of the T/E box cut.

a 150 – 250 ns range. For each of the externally-pulsed detectors, the rise-time was tuned so that the T/E of the pulser waveforms matched the T/E of background physics events above 70 keV. After tuning, pulser data was taken at varying attenuation values. There was a noticeable increase in the variance of the measured T/E values when the computed pulser waveform dropped below 20 keV. An example of a T/E vs. E plot of pulser data is shown in figure 5.11.

To estimate the fast pulse acceptance rate as a function of energy, the ratio of accepted pulser events to total pulser events was computed. Recall that events within the $1.2 < T/E < 2.1$ window are accepted. Two energy histograms were generated by projecting the pulser events in figure 5.11 onto the energy axis: one containing only events in the acceptance window, and one containing all pulser events. The resulting spectra of pulser energy peaks were partitioned by attenuation value (i.e. blobs in figure 5.11) to create variably binned histograms with a total of one bin per partition. To compute the acceptance rate, a

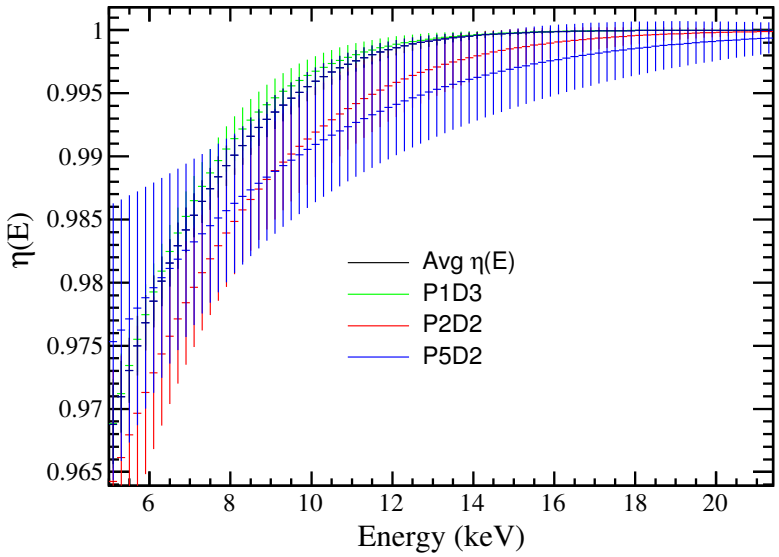

Figure 5.12: The T/E acceptance curves for P1D3 (green), P2D2 (red), and P5D2 (blue) The average value of the three curves is also shown in black. At 5 keV, the worst possible acceptance value from either detector is roughly 96%. Above 20 keV, the acceptance is close enough to 100% and is neglected in the DM analysis.

histogram of the ratio of accepted events to the total number of events was generated using a member function in the ROOT package. Uncertainty values for each bin were computed assuming that the acceptance ratio was binomially distributed ensuring that uncertainty approaches zero when acceptance approaches 100%.

As shown in figure 5.11 only 7 pulser peaks contained events above 5 keV. For each of the three externally pulsed detectors included in the analysis, an error function (Erf) was fit to the computed acceptance values:

$$\eta(E) = \mathrm{Erf}((E-\mu)/\sqrt{2\sigma}) \,, \tag{5.3}$$

where E is the peak energy. The parameters μ and σ were allowed to float in the fit. The 68% confidence intervals for $\eta(E)$ were computed from the uncertainties of μ and σ. A plot of the T/E acceptance functions for P1D3, P2D2, and P5D2 is shown in figure 5.12 (P6D3 was improperly tuned and was not included).

The acceptance estimates shown for the three detectors in figure 5.12 were the only estimates available for DS0. Ideally, externally pulsed data would have been available for all detectors. This will be the case for future data sets collected during production data runs. In the bosonic dark matter analysis, the T/E acceptance efficiency fit from P5D2 data was used to estimate the overall acceptance for the analysis spectrum. These are conservative values because P5D2 has the widest confidence belt and permits the lowest values of $\eta(E)$ above 7 keV. The P5D2 fit values were $\mu = -26 \pm 4$ keV, $\sigma = 13.7 \pm 1.7$ keV with a strong anti-correlation, corr(μ, σ) $\sim$ -1. A correction is added to the likelihood analysis for energies below 20 keV, see equation 6.12. Above 20 keV, the acceptance quickly approaches 100% and is not considered in the DM analysis.

Section 5.4: Data Cleaning Summary

Three data cleaning cuts are applied to MJD DS0 for the bosonic DM analysis. Table 5.1 summarizes the data cleaning parameters. A multiplicity cut is applied to remove electronic and microphonic noise that triggers multiple channels. Background physics events such as Compton scattering that deposit energy in multiple detectors are also conveniently removed by this cut. A waveform tag that takes advantage of the pole-zero undershoot in a trapezoidal-filtered charge-waveform, caused by capacitive discharge in a feedback circuit was developed. This tag was effectively identified pulser recovery waveforms that were characterized by rising tails. Finally a scaled triangle filter (T/E) applied to charge-pulse waveforms was useful for discriminating between slow and fast rising waveforms. The application of the three cuts described in this chapter resulted in the DS0 spectrum shown in figure 4.7.

For both the multiplicity cut and the pulser-retriggering cut, the event reduction of anti-coincident physics events was found to be negligible. A small, <4%, fast-pulse reduction at very low energies was associated with the T/E cut. The $\eta(E)$ function in equation 5.3 is accounted for in the DM analysis. A profile likelihood analysis that takes into account

the data cleaning and systematic parameters is used to constrain the electronic coupling of bosonic dark matter and additional exotic physics in chapter 6.

Table 5.1: Summary of the data cleaning parameters.

Parameter	**Description**	**Acc. Range**	**Acc. Efficiency**
T/E	Energy scaled triangle-filtered waveform maxima, for slow-pulse removal.	$1.2 < T/E < 2.1$	$\eta(E)$ (>96%)
trapMin	Trapezoidal filtered minimum, searches for filtered undershoot. Used to remove pulser-retriggering events.	< 0	>99.95%
Multiplicity	Number of coincident detectors in an event, use for transient pulse removal.	1	>99.88%
waveformMin*	Raw waveform min val tested to tag transient events	*abandoned	

CHAPTER 6: Profile Likelihood Analysis and Results

The profile likelihood method was used to analyze the DS0 background data that passed the selection criteria and the cleaning cuts. This chapter will provide an overview of the profile-likelihood method and its application to the energy spectrum. A model of the response in the energy-spectrum from a hypothetical signal above a background is developed. The analysis technique is then applied to constrain the number of dark matter signal counts in the model, with the degree of confidence determined via Wilk's theorem. This chapter will present the results from searches for pseudoscalar and vector dark matter. Results of the following additional rare searches will also be given: the 14.4 keV solar axion peak, a 10.6 keV peak from Pauli-exclusion violating decay in germanium, and an 11.1 keV peak following an electron decay in germanium.

Section 6.1: The Profile Likelihood Method

Confidence intervals describing the strength of a particular component in a data model can be computed using the profile likelihood method [122, 171, 172]. A generic data model will often consist of a set of parameters of interest, such as the number of detected signal or background events, along with a set of nuisance parameters. These nuisance parameters will usually represent data collection systematics, i.e. experimental parameters such as measurement resolution and efficiency. In the profile likelihood analysis, all parameters are simultaneously optimized in the data model with respect to a particular parameter(s) of interest, resulting in a test statistic that depends on the interesting parameter(s), see equation 6.4. The method has been used by this and other experiments to search for rare events amongst background events.

6.1.1: Constructing the Profile Likelihood Function

The first step of the profile likelihood analysis is constructing an un-binned likelihood function. Since optimization requires maximizing a multivariate function and is usually performed by computer software, the first step is generally the most demanding of the analyst. The likelihood function is computed over all the data points [171]:

$$\mathcal{L}_{\text{model}}(\vec{\theta}, \vec{\nu}) = \prod_{i}^{n} f(x_i; \vec{\theta}, \vec{\nu}) \tag{6.1}$$

where $\{x_i\}_i^n$ is the set of random variables measured by the experiment, $\vec{\theta}$ is a set of parameters of interest and $\vec{\nu}$ is a set of nuisance parameters. Here f is a probability density function (PDF) that encodes the data model. A common example is a gaussian signal peak superimposed upon a polynomial background. The parameter of interest in this case might be the number of signal counts in the gaussian peak. The nuisance parameters would be the peak mean and width, along with the polynomial coefficients describing the background model. If there is some prior degree of knowledge about a parameter, additional terms can multiplied to the likelihood function to constrain the parameter to a certain range. For example, if ν_i is known to be within the range $\bar{\nu}_i \pm \sigma_{\nu_i}$ assuming gaussian error bars, then equation 6.1 can be multiplied by [122]:

$$\mathcal{C}_{\nu_i}(\nu_i; \bar{\nu}_i, \sigma_{\nu_i}) = A \cdot \text{Exp}\left(\frac{(\nu_i - \bar{\nu}_i)^2}{2\sigma_{\nu_i}^2}\right) \tag{6.2}$$

where A is an arbitrary normalization constant. The gaussian in equation 6.2 restricts the range within which ν_i can float during extremum finding of $\mathcal{L}_{\text{model}}$. If two parameters ν_i and ν_j are correlated, the gaussian in equation 6.2 can be replaced with a multivariate gaussian distribution.

In rare-event searches, it is often difficult to distinguish between background events and signal events. For a given energy, E, it is assumed that the total number of counts in

the neighborhood of E will be poisson distributed. In order to properly account for the fluctuation of the signal and background counts, the PDF in equation 6.1 can be extended, allowing the count rates to float in the likelihood optimization. This is done by multiplying the likelihood function by a poisson constraint term [172]:

$$\mathcal{L}_{\text{ext}}(S, B) = \frac{(S+B)^n}{n!} e^{(S+B)} \ , \tag{6.3}$$

where S and B are elements of $\vec{\theta}$ that correspond to the number of signal and background counts in the model PDF, f, and n is the number of data points. When the data model is fit during the extended likelihood function maximization, the poisson term ensures that S and B are anti-correlated so that the proper number of events in the data can be attributed to each. The full extended likelihood function, $\mathcal{L}$, is the product of $\mathcal{L}_{\text{ext}}$, $\mathcal{L}_{\text{model}}$, and the constraints, $\mathcal{C}_i$.

To define the profile likelihood, let $\vec{\phi} = (\vec{\theta} \ \cup \ \vec{\nu}) - \{\varphi\}$, where φ is the parameter of interest. The profile curve is a function of φ only [172]:

$$\lambda(\varphi) = \frac{\mathcal{L}\left(\varphi, \hat{\vec{\phi}}\right)}{\hat{\mathcal{L}}\left(\hat{\varphi}, \hat{\vec{\phi}}\right)} \ . \tag{6.4}$$

A hat over a parameter indicates the value at the extremum of the likelihood function, $\hat{\mathcal{L}}$. The profile curve $\lambda(\varphi)$ is the value of the likelihood function at φ scaled by the global extremum value when all other parameters have been optimized. When $\varphi = \hat{\varphi}$, the profile statistic value is unity. Since it is usually easier to handle summations than products in formulae, the negative log of the likelihood function (NLL) and profile curve is often computed. The monotonicity of the log function ensures that parameter critical points and the likelihood critical values remain unchanged.

The profile curve of a parameter φ encapsulates not only the best fit value in the model, but also the degree of confidence in the fit. According to Wilks' theorem [173], the log of

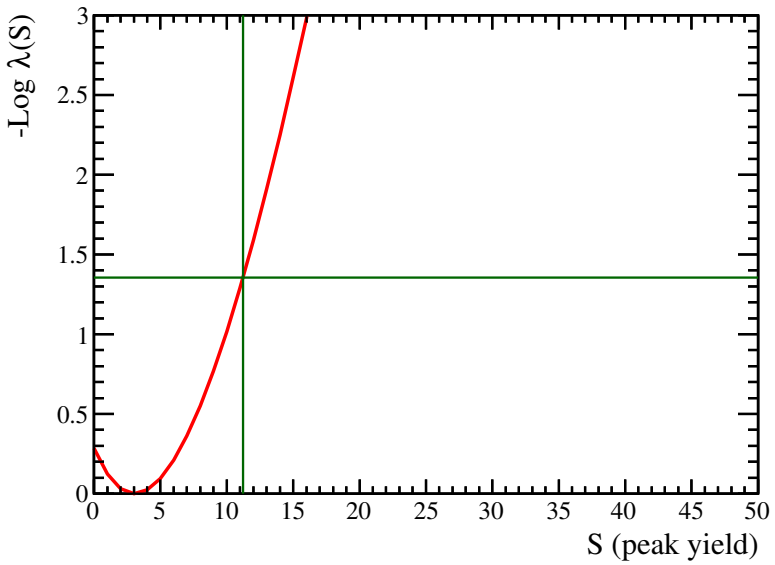

Figure 6.1: A profile curve generated from the DS0 data, searching for a signal peak at 14.4 keV. The horizontal green line intersects the profile curve at the bounds of the 90% confidence interval (1.355). Note that the lower bound is below zero, indicating that zero signal is well within the interval. The vertical green crosses the abscissa at the 90% upper limit.

the profile curve closely follows a chi-squared distribution of one degree of freedom:

$$\frac{\chi^2}{2} = -\log\,\lambda(\varphi)\ . \tag{6.5}$$

The $100(1-\alpha)\%$ confidence interval (C.I.) for φ is the interval Φ such that all elements of the map $2\times\mathrm{nLL}(\Phi)$ are less than χ^2_α. The 90% C.I. is presented in the results that follow. This corresponds to negative log profile values less than $\chi^2_{0.1}/2 = 2.71/2 = 1.355$. An example of the profile curve for a 14.4 keV peak signal is shown in figure 6.1.

Because of statistical fluctuations in any data set, there is a chance that the best fit value for a parameter of interest could be a non-physical value, e.g. a negative mass. This is a fairly common occurrence when estimating the limit on the number of signal events when the background is expected to dominate. Computation of the C.I. for parameters with

non-physical best fit values is handled by shifting the profile curve [172]:

$$\log\lambda'(\varphi) = \log(\varphi) - \log(0) \ . \tag{6.6}$$

In this case, the lower bound of the interval is already in the non-physical region so only the upper limit is of any concern. The CI is still defined as the parameter interval that is mapped to values of less than 1.355 by the negative log profile curve. Equation 6.6 is a conservative method of restricting the optimal parameter value to a physical domain because the width of the parameter interval is increased, introducing over-coverage to the CI.

In practice, computing the profile curve in equation 6.4 is done via optimization software. In this work, the RooFit [174] extension of ROOT [163]–a data analysis package used in nuclear and particle physics–minimized the NLL function. RooFit utilizes the MINUIT [175] package and the MIGRAD [176] algorithm. The RooFit software was originally developed by the BaBar collaboration for analysis of B-meson decay data, and has since become a tool used by many rare-event search experiments [177–179].

6.1.2: Building the Signal and Background Model

In the RooFit framework, probability density function objects are created to represent different components of the data model. RooFit has the ability to sum and multiply PDFs together via a set of PDF handling classes. For this analysis the signal is modeled by a simple Gaussian. The background model has three components: the tritium decay spectrum, the 10.36 keV ^{68}Ge K-shell x-ray, and a linear continuum. The parameter of interest is the number of counts in the signal component. Both the signal and background components will be constrained by an extended likelihood term, see equation 6.3. A multi-variate gaussian constrains the model nuisance parameters.

Signal Model

A bosonic dark matter interaction with the detector is expected to be fully absorbed, imparting its rest mass energy into the detector. This process is analogous to the photoelectric effect. At low energies, spectral tailing effects are minimal because the statistical fluctuation due to charge production dominates the fluctuation due to collection, see equation 2.12. The expected signal pdf is thus a gaussian centered about the rest mass energy. In Chapter 4 a systematic linear offset in the calibration was discussed. The correction parameters are used to modify the gaussian form:

$$\mathcal{P}_S(E_i; E_S, \alpha_E, E_0, \sigma_E) = \frac{1}{\sqrt{2\pi}\sigma_E}\text{Exp}\left(\frac{-(E_i - [E_S + \alpha_E(E_S - E_{\text{center}}) + E_0])^2}{2\sigma_E^2}\right) \quad (6.7)$$

where E_i is the energy measured for event i, E_S is the signal energy, α_E and E_0 are calibration correction parameters, $E_{\text{center}} = 95$ keV is the constant-valued center of the correction fit, and σ_E is the resolution (FWHM / 2.355) at energy E_S (equation 4.3). The nuisance parameters α_E, E_0, and σ_E are floated in the the fit while E_S is held constant.

Background Model

Three separate PDFs are generated for their respective model components: $\mathcal{P}_K$, $\mathcal{P}_T$, and $\mathcal{P}_B$. A gaussian with the same form of equation 6.7 was used to model ^{68}Ge K-shell peak PDF, $\mathcal{P}_K$, substituting the parameter E_S with 10.36 keV and σ_E with $\sigma_{10.36}$.

The tritium PDF, $\mathcal{P}_T$, was more complicated to model. Neglecting the electron neutrino mass in the decay, the energy distribution of the tritium decay is a continuous function below the 18.6 keV Q-value and is zero above:

$$\mathcal{P}_T(E_i; m_E, Q) = C \cdot F(E_i, Z = 2) \cdot p \cdot (E_i + m_E) \cdot (Q - E_i)^2 \quad (6.8)$$

where C is a normalization constant, $F(E_i, Z)$ is the Fermi function that accounts for

coulomb effects, p is the momentum of the beta particle, m_E is the electron mass, and E_i is the measured kinetic energy of the beta particle. For a more complete discussion, see [180].

It's not possible to write down a closed analytic form of beta decay spectrum because the Fermi function contains a complex-valued gamma function term. The complex valued gamma function is also not a standard function included in math libraries for C++. As a work-around, a collaborator [181] generated a finely binned (5 bins / keV) histogram that sampled the tritium spectrum using the Lanczos [182] approximation of the gamma function. RooFit is capable of converting a histogram into a PDF object. Linear interpolation was used to estimate the spectral value between the center of each bin.

Above 18.6 keV, the only component of the data model is the linear background. The linear model is a catch-all approximation that accounts for physics related events that have a continuous energy-spectral signature. Examples include beta decays, Compton Scattering events, two neutrino decays, and bremsstrahlung from naturally occurring radioactive materials present in the detector and shielding materials. The PDF is of the form:

$$\mathcal{P}_B(E_i;\vec{B}) = \frac{1}{B}\left[m(E_i - \bar{E}) + B\right] \tag{6.9}$$

where $\vec{B}$ is a vector of parameters, $(B, m, \bar{E})$. Here B is the linear background rate, m is the slope of the fit, and $\bar{E}$ is the center point of the distribution.

Energy Spectrum Model and Likelihood Function

The three components of the background model and the signal are summed in RooFit. Additional scaling terms are included for proper PDF normalization. The full spectral model is of the form:

$$\mathcal{P}_{\text{spec}}(E_i;\mathcal{S},\vec{\nu}) = \frac{\sum\limits_{n\,\epsilon\,\mathcal{S}} n \times \mathcal{P}_n(E_i;\vec{\nu})}{\sum\limits_{n\,\epsilon\,\mathcal{S}} n} \tag{6.10}$$

where $\mathcal{S}$ is the set $\{\eta_E S, K, T, B\}$ of component strengths in counts, and $\vec{\nu}$ is a vector that encapsulates all other nuisance parameters. The value η_E is the T/E efficiency function from chapter 5. In the likelihood fit, the T/E correction is applied to the signal parameter S, effectively adding a small penalty to the fit result to account for the acceptance uncertainty. The other parameters are essentially nuisance parameters that are fit out in the model. The spectral component of the likelihood function is then given by the product over the data points:

$$\mathcal{L}_{\text{spec}}(\mathcal{S}, \vec{\nu}) = \prod_i \mathcal{P}_{\text{spec}}(E_i; \mathcal{S}, \vec{\nu}) \ . \tag{6.11}$$

The extended likelihood constraint, equation 6.3, is also applied over the set $\mathcal{S}$. The extended likelihood term is multiplied by the spectral term:

$$\mathcal{L}_{\text{ext}}(\mathcal{S}) \times \mathcal{L}_{\text{spec}}(\mathcal{S}, \vec{\nu}) = \frac{(\eta_E S + K + T + B)^n}{n!} e^{(\eta_E S + K + T + B)} \times \prod_i \mathcal{P}_{\text{spec}}(E_i; \mathcal{S}, \vec{\nu}) \ . \tag{6.12}$$

It should be noted that RooFit takes care of most of the setup of the extended likelihood function as a back-end process. The user is responsible for creating PDF objects. Objects that handle PDF summing can be provided with either a fractional component PDF strength or an initial guess on the counts due to a PDF component. If a number of counts is provided, RooFit will automatically include the extended term.

Finally, a likelihood term that incorporates the constraints on the remaining nuisance parameters (see table 6.1) must be constructed. Since there are multiple parameters–not all of which are independent–a multivariate gaussian constraint term is necessary. The most compact form is:

$$\mathcal{L}_{\text{constraint}}(\vec{\nu}; \vec{\bar{\nu}}, \mathbf{\Sigma^2}) = \frac{1}{\sqrt{|2\pi\Sigma_{ij}^2|}} \text{Exp}\left(-\frac{1}{2}\left(\nu_i - \bar{\nu_i}\right) \Sigma_{ij}^2 \left(\nu_j - \bar{\nu_j}\right)\right) \tag{6.13}$$

where $\vec{\nu}$ is the vector $(\alpha_E, E_0, \sigma_E, \eta_E)$ of nuisance parameters that are constrained in the fit. Other nuisance parameters are either constant or allowed to float unconstrained. The $\vec{\bar{\nu}}$

values are the mean values of $\vec{\nu}$. Einstein summation notation is used to denote summing over the nuisance parameters, their corresponding mean values, and the covariance matrix, $\mathbf{\Sigma^2}$. The covariance matrix used in this analysis is:

$$\Sigma^2_{ij} = \begin{pmatrix} \sigma^2_{\alpha_E} & \mathrm{cov}(\alpha_E, E_0) & 0 & 0 \\ \mathrm{cov}(\alpha_E, E_0) & \sigma^2_{E_0} & 0 & 0 \\ 0 & 0 & \sigma^2_{\sigma_E} & 0 \\ 0 & 0 & 0 & \sigma^2_{\eta_E} \end{pmatrix} \tag{6.14}$$

with the variance terms on the diagonal. While both σ_E and η_E were the result of multi-parameter fit functions (see equations 4.3 and 5.3), their total variances as a function of energy was computed prior to the likelihood analysis to cut down on the number of nuisance parameters. The total likelihood function is the product of the spectral, extended, and constraint terms:

$$\mathcal{L}(\mathcal{S}, \vec{\nu}) = \mathcal{L}_{\mathrm{ext}}(\mathcal{S}) \times \mathcal{L}_{\mathrm{spec}}(\mathcal{S}, \vec{\nu}) \times \mathcal{L}_{\mathrm{constraint}}(\vec{\nu}) \; . \tag{6.15}$$

Table 6.1 summarizes the parameters in the likelihood analysis. While the systematic parameters were constrained by their uncertainties, some parameters had to be restricted so that MINUIT didn't explore parameter spaces that were qualitatively non-optimal, i.e. to avoid improper fits.

With the total likelihood function, a profile curve for S, equation 6.4, can be generated. The log of the likelihood function is minimized in RooFit, considering all of the parameters in table 6.1. Details of the results of the rare event searches are presented in section 6.2.

Section 6.2: Results

The results of the profile likelihood analysis are presented in this section. The 90% confidence limits on rare-event energy deposition in MJD DS0 data were computed following

Table 6.1: Likelihood Analysis Parameters

Parameter	**Description**	**Init. Value** $(\boldsymbol{\mathcal{S}}, \bar{\boldsymbol{\nu}})$	**Float Range** $(\boldsymbol{\sigma_{\bar{\nu}}})$	**Notes**
S	Dark Matter / Rare-Event signal counts	0.1	-5 - 10,000	Range limited in RooFit
T	Tritium counts	0.02	0 - 10,000	$''$
K	^{68}Ge K-shell x-ray counts	10	0 - 10,000	$''$
B	Linear background counts	20	0 - 10,000	$''$
α_E	Calibration gain correction	-0.0014	$\pm$0.0009	Constrained in likelihood
E_0	Calib. offset correction	-0.256 keV	$\pm$0.016	$''$
$\mathrm{cov}(\alpha_E, E_0)$	Covariance parameter	-3.0×10^{-6} keV	n/a	constant
E_S	Energy of rare-event signal	varies	n/a	Varies depending on signal of interest
E_{center}	Center of calib. correction fit	95 keV	n/a	constant
σ_E	Energy resolution (FWHM / 2.355 at E_S)	Eqn. 4.3	$\pm\sigma_{\sigma_E}$	Computed from fit parameters in Eqn. 4.3
m	Slope of the linear background	2×10^{-5}	-0.1 - 0.1	Range limited in RooFit
$\bar{E}$	Center of linear fit	52.5 keV	n/a	constant
η_E	T/E acceptance correction	Eqn. 5.3	$\pm\sigma_{\eta_E}$	Computed from fit parameters in Eqn. 5.3

Wilks' theorem, equation 6.5. For the pseudoscalar and vector dark matter searches, exclusion plots comparing the MAJORANA limits with other experiments are shown. For each rare event, a brief overview of the individual analyses is also discussed.

6.2.1: Search for keV-scale bosonic pseudoscalar DM

A psuedoscalar boson, or axion-like particle (ALP), may interact electronically with the detector, ejecting energetic electrons into the fiducial volume. This interaction is analogous to the photoelectric effect in germanium detectors. In this analysis, a search for events where the ALP is completely absorbed by the detector, imparting the total–rest mass plus kinetic–energy to the detector, is performed. The signature event produces a photo-like peak in the energy-spectrum with unexplained origin. While additional effects such as axio-electric Compton scattering may be possible, there would be virtually no chance of distinguishing such events from the continuum background in the energy spectrum.

To compare results of this analysis with other experiments, a couple of assumptions must

be made. Following EDELWEISS [78], it is assumed that axions constitute all of the galactic dark matter. Previously, experiments have cited a dark matter halo density within our solar system of $\rho_{DM} = 0.3$ GeV/cm^3. This value will also be used here, despite more recent results that estimate the local DM density to be closer to 0.4 GeV/cm^3 [42]. The dark matter density is necessary to compute the flux:

$$\Phi_{DM}(m_A) = \rho_{DM}\frac{v_A}{m_A} = 7.8 \times 10^{-4}\left(\frac{1}{m_A}\right) \cdot \beta \text{ [/barn/day]} , \tag{6.16}$$

where m_A is the mass of the ALP and v_A is the average DM velocity. From the halo model, the average DM velocity in the Milky Way is roughly 230 km/s [54]. Here, the value 0.001 is used for $\beta = v_A/c$, where c is the speed of light. Since this implies non-relativistic DM, the energy of a DM interaction with the detector would be $E = \sqrt{m_0^2 + \gamma^2 m_0^2 \beta^2} \sim m_0$.

In general, the strength of the expected signal in the energy spectrum is a product of the flux, Φ_{DM}, the axio-electric cross section, σ_{Ae} and the exposure, MT. Including the detector response, the differential ALP count rate is given by:

$$\begin{aligned}\frac{dN}{dE}(E; m_A) &= \Phi_{DM}(m_A)\sigma_{Ae}(m_A)\times \\ &\qquad \eta(E)\frac{1}{\sqrt{2\pi}\sigma_E(m_A)}\text{Exp}\left(-\frac{(E-m_A)^2}{2\sigma_E^2(m_A)}\right)\sum_i M_i T ,\end{aligned} \tag{6.17}$$

$$\sigma_{Ae}(m_A) = \sigma_{pe}(m_A)\frac{g_{Ae}^2}{\beta}\frac{3m_A^2}{16\pi\alpha m_e^2}\left(1 - \frac{\beta^{\frac{2}{3}}}{3}\right) . \tag{6.18}$$

The summation is over the 13 enriched detectors used in the analysis. Equation 6.18 is the form used in [183]. The axio-electric coupling constant, g_{Ae}, is the parameter of interest that is determined after finding the limit on the number of DM signal counts in the likelihood analysis; α is the fine structure constant, $\sim$1/137; m_e is the electron mass, 511 keV; and σ_{pe} is the photoelectric absorption cross section. The value of σ_{pe} as a function of energy is shown in figure 6.2 [184].

For the DS0 data set, no indication of a peak due to coupling of ALPs was discovered in

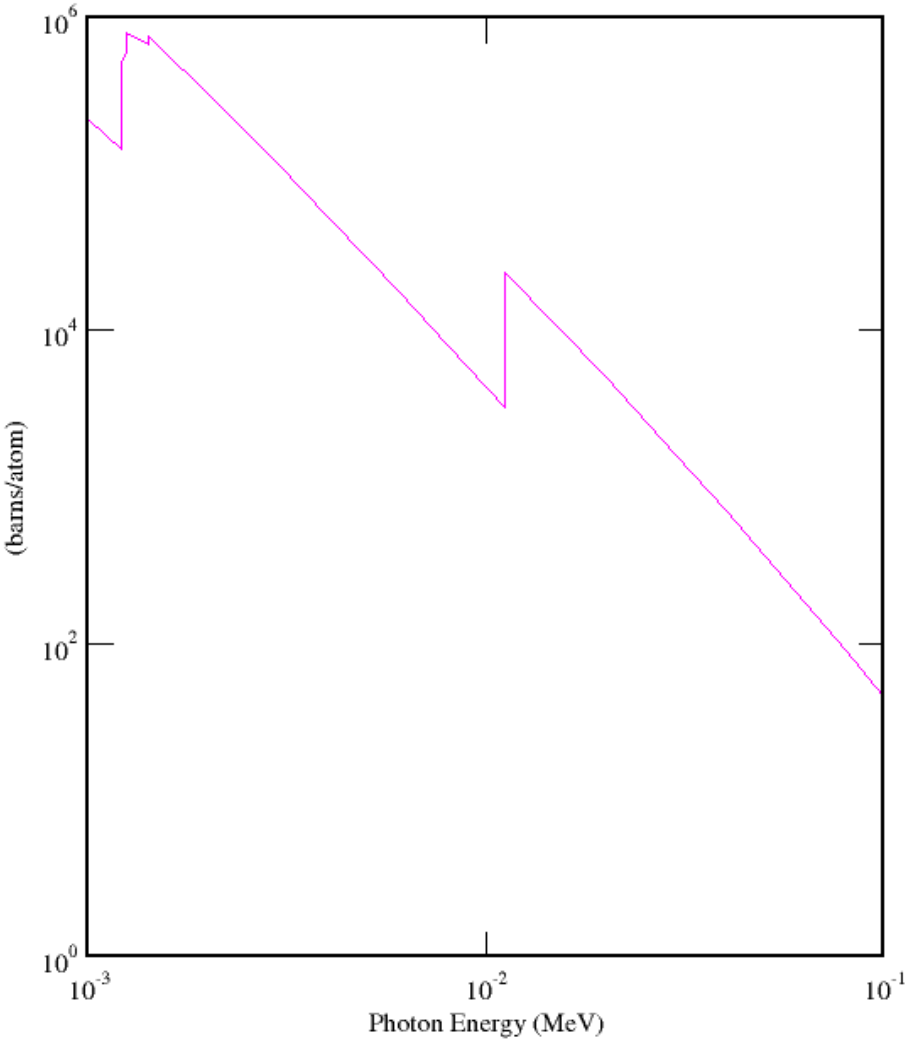

Figure 6.2: Photoelectric absorption cross section of germanium as a function of energy. The discontinuity at 10.36 keV is due to the K-shell resonance. Figure generated with a tool from [184].

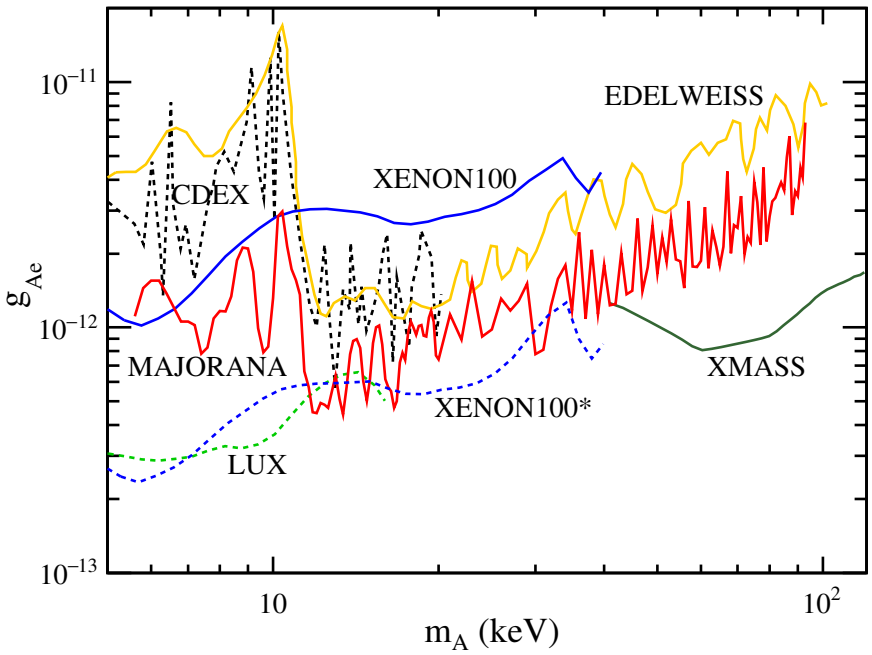

Figure 6.3: The 90% upper limit from the 90% confidence interval as a function of pseudoscalar mass, m_A. The MAJORANA limit (red) is compared to previous limits from EDELWEISS [78] (orange), XENON-100 [185] (blue), XENON-100 erratum [186] (dashed blue), XMASS [79] (green), CDEX (dashed black) [187], and LUX (dashed green) [188]. The most stringent MAJORANA limit is set at 11.8 keV, corresponding to a 90% UL of $< 4.4 \times 10^{-13}$ for g_{Ae}.

the energy spectrum. The 90% upper limit of the number of signal counts for a given ALP mass (m_A) was computed. Within the 5 - 20 keV range, the signal limit was determined at 0.2 keV increments. Above 20 keV, the limit was computed at 1 keV increments. The upper limit of the signal count was interpreted to be equivalent to the product of the DM flux, cross section, and exposure in equation 6.17. The resulting 90% upper limits on g_{Ae} along with comparisons to other experiments are shown in figure 6.3.

The MAJORANA pseudoscalar coupling results are competitive below 40 keV. Above 40 keV, XMASS [79] has the best limit due to their >7600 kg-y exposure compared to the 478±6 kg-d exposure of the DS0 data. The significant improvement over EDELWEISS [78] below the germanium k-ledge results from the effort taken by MAJORANA to reduce the cosmogenic exposure of the enriched detectors. While the DS0 background rate (figure 4.7)

above 18.6 keV (H^3 beta-decay endpoint energy) is roughly a factor of 10 better than what EDELWEISS presented, the coupling limit scales as the fourth root of the rate. The most stringent DS0 ALP limit of $< 4.5 \times 10^{-13}$ is set at $m_A = 11.8$ keV.

6.2.2: Vector bosonic dark matter results

The same analysis presented above for pseudoscalar dark matter can be applied to set limits on the coupling strength of vector bosonic dark matter to ordinary matter. As explained in section 1.2.3, unlike the pseuodscalar limits, the limits on vector-electric coupling that can be established by direct detection experiments are potentially more stringent than limits derived from cosmological and astronomical sources [76]. This is a result of the forbiddenness of the two gamma mode in vector-gamma decay (see figure 1.9). The dominant decay to three photons occurs at the loop level in the Feynman diagram.

Following the formalism presented by Pospelov et. al. [76], the product of the DM flux and the vector-electric cross-section is given by:

$$\Phi_{DM}(m_V)\sigma_{Ve}(m_V) = \frac{4 \times 10^{23}}{m_V} \left(\frac{\alpha'}{\alpha}\right) \frac{\sigma_{pe}(m_V)}{A} \text{ [/kg/d] .} \tag{6.19}$$

Here m_V is the vector mass in keV, σ_{Ve} is the vector-electric absorption cross-section, A is atomic mass of germanium enriched to 87% ^{76}Ge, and $\alpha' = (e\kappa)^2/4\pi$ is an analogue of the fine structure constant. The quantity $e\kappa$ is the coupling strength that appears in the interaction term of the vector DM Lagrange density. Note that the parameter of interest in equation 6.19, α'/α, is equivalent to κ^2. This yields a roughly factor of two difference in the order of magnitude of the limit when compared to ALP coupling.

To find the coupling parameter α'/α, the product of the flux and cross-section in equation 6.17 was replaced with equation 6.19. The computed 90% upper limit for DS0 is shown in figure 6.4. It is clear from the figure that the DS0 limit is more stringent than some of the astronomical limits (dashed lines), including limits associated with the gamma background

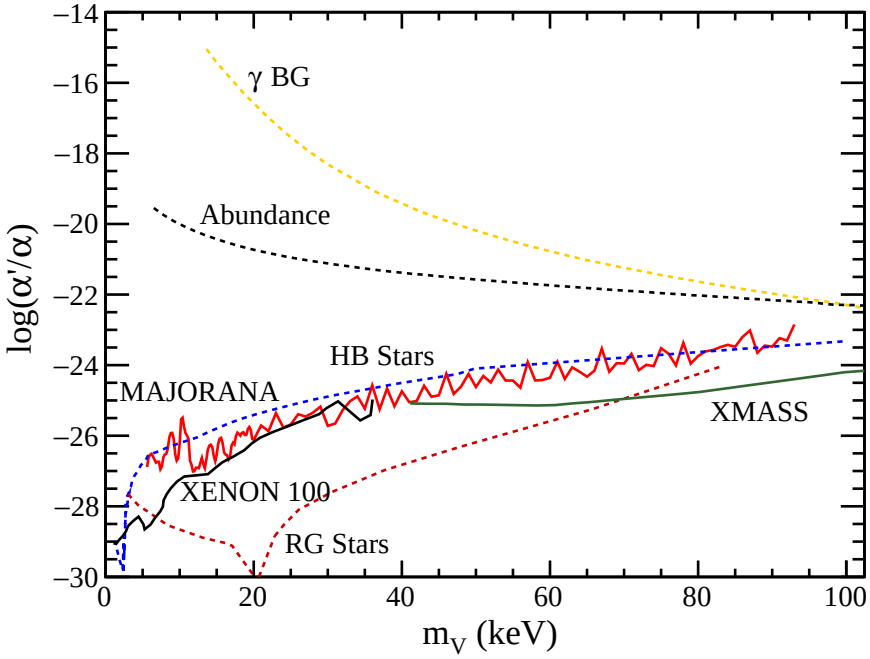

Figure 6.4: Fine-structure parameterization of the 90% vector-electric coupling upper limit as a function of vector mass (m_V). Dashed lines represent model dependent astrophysical or cosmological limits, including the gamma background (yellow), horizontal branch stars (blue), red giant stars (red), and dark matter abundance (black) [76, 189]. The solid curves show the MAJORANA limit (red), the XMASS limit [79] (green), and a limit computed in [189] from XENON 100 data.

from three gamma decays in the galaxy, helium burning in horizontal branch stars, and the thermal DM production abundance (assuming vectors account for 100% of DM). The vector-electric limit set from energy loss in red-giant stars is still stronger than the MAJORANA limit [76, 189]. The best MAJORANA limit was $\alpha'/\alpha < 9.7 \times 10^{-28}$ for $m_V = 11.8$ keV.

6.2.3: Solar axions produced in the ^{57}Fe $M1$ transition

The MAJORANA DEMONSTRATOR DS0 data was used to search for additional rare-event processes beyond the scope of halo dark matter. One particular candidate is the solar axion. These candidates are QCD axions produced in the sun with masses that depend on the Peccei-Quinn symmetry breaking scale, f_A, and should be distinguished from the more generic pseudoscalar particles discussed in section 6.2.1.

The core of the sun contains an abundance of iron. The isotope ^{57}Fe is stable with an abundance of 2.12%. The temperature at the solar core, kT ∼1.3 keV [190] is high enough to thermally excite ^{57}Fe into its first excited state at 14.4 keV. Since de-excitation of this state mainly occurs through a magnetic dipole (M1) transition, it may be possible for axion emission to compete with the conventional emission of either a photon or an internal-conversion electron. The effective Lagrange density that couples axions to nucleons is given by:

$$\mathcal{L} = i\bar{\psi}_N \gamma_5 (g^0_{AN} + g^3_{AN}\boldsymbol{\sigma}_3)\psi_N \phi_A \tag{6.20}$$

where ϕ_A is the axion field, ψ_N is the nucleon isospin doublet, and $\boldsymbol{\sigma}_3$ is a Pauli matrix. The isoscalar and isovector axio-nuclear coupling constants, g^0_{AN} and g^3_{AN} respectively, are model dependent parameters. Explicit parameterizations for KSVZ and DFSZ axions are given in Refs. [191, 192].

An axion model-independent analysis is presented here, which combines the product of the axio-nuclear (g_{AN}) and axio-electric (g_{Ae}) coupling to account for both solar production and electronic coupling in the detector. Solar axions fully absorbed by the detector would deposit 14.4 keV of energy, resulting in an absorption peak. The differential count rate due to the combined axion signal and background is nearly identical to equation 6.17. The ALP mass term is replaced by the axion energy, 14.4 keV, and the DM flux term is replaced by the axion flux, from [78]:

$$\Phi_{14.4} = \beta^3 \times 4.56 \times 10^{23} (g^{\text{eff}}_{AN})^2 \ [/\text{cm}^2/\text{s}] \ . \tag{6.21}$$

The effective nuclear coupling, g^{eff}_{AN} combines the isoscalar and isovector coupling terms in equation 6.20. Many axion models favor very small mass, $\sim 10^{-6}$ eV, suggesting that the reduced axion velocity, $\beta \sim 1$. To account for non-relativistic limit, the coupling product, $g^{\text{eff}}_{AN} \times g_{Ae}$ is presented as a function of mass in figure 6.5. The model fit to the data, allowing the signal counts to float, is shown in figure 6.6.

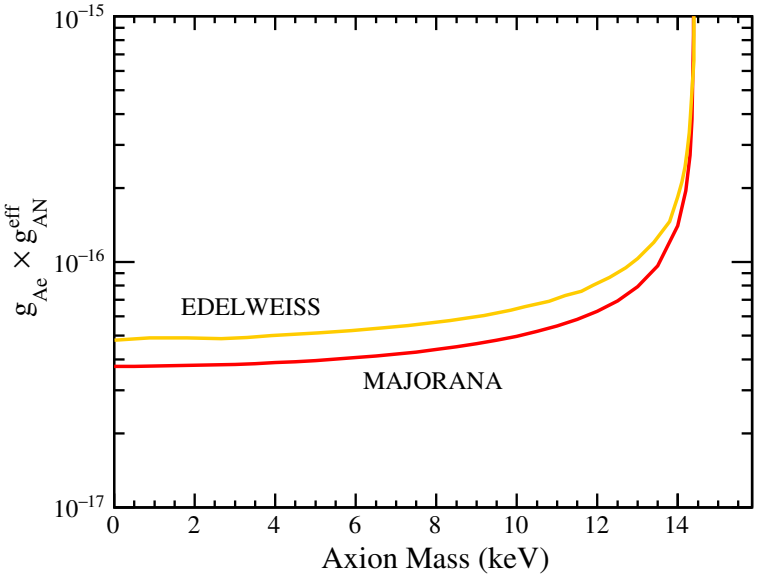

Figure 6.5: The 90% upper limit of the axio-nuclear and axio-electric coupling as a function of energy. The MAJORANA limit (red) is about 25% more stringent than the previous EDELWEISS [78] limt (orange). The limit blows up as the axion mass approaches 14.4 keV while β simultaneously approaches zero.

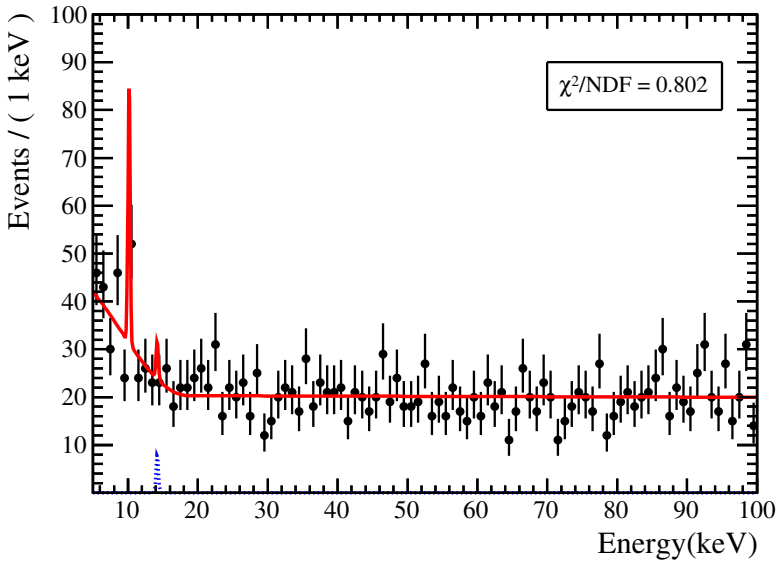

Figure 6.6: Best fit of the background data from 478±6 kg d of DS0 data assuming a signal peak at 14.4 keV (blue). The red curve also includes the tritium spectrum, the 10.36 keV ^{68}K-Shell peak, and the linear background.

Results of the solar axion search constrain the coupling product, $g_{AN}^{\text{eff}} \times g_{Ae}$, to $< 3.8 \times 10^{-17}$ for massless axions. As the axion mass approaches 14.4 keV, β approaches zero. This causes the limit to blow up since β appears in the denominator when solving for the coupling. The MAJORANA limit is roughly 25% better than the EDELWEISS limit. Statistical fluctuations in the background coupled with the fourth root dependence on the background elicit difficulties when trying to improve upon previous work.

6.2.4: Pauli Exclusion Violating Decay

The Pauli exclusion principle (PEP) is a fundamental law of physics that was originally proposed by Wolfgang Pauli in the 1920s [193]. The PEP states that no two identical fermions can occupy the same quantum state. In quantum field theory, the PEP is related to spin statistics and arises from the anti-commutativity of the fermion creation and annihilation operators.

Despite the fundamental nature of the PEP, its physical origin is not well understood. While it is successful in explaining phenomena from multiple branches of physics, including atomic and nuclear, the validity of some aspects of the principle can still be challenged. While particles tend to be classified as fermions (half-integer spin) or bosons (integer spin), QFT permits states that obey general spin statistics, i.e. mixed states. On a fundamental level, these states follow from a modified commutative algebra [194]:

$$a_i a_j^\dagger - q a_j^\dagger a_I = \delta_{ij}, \quad -1 \leq q \leq 1 \ , \tag{6.22}$$

where a_i is an annihilation operator and $a_j^\dagger$ is a creation operator. If $q = -1$ then equation 6.22 reverts to the fermionic anti-commutation relation. If instead, $q = -1 + \beta^2$ with $\beta^2 \ll 1$, then the algebra can describe particles with a small mixed symmetric component capable of violating PEP. The value $\beta^2/2$ gives the probability of measuring the mixed component, and is the parameter that is often quoted by experimental PEP violating searches.

The transition width of the decay, written in terms of $\beta^2/2$ is given by:

$$\Gamma = \frac{\beta^2}{2}\tilde{\Gamma}\,, \tag{6.23}$$

where $\tilde{\Gamma}$ is the transition width into the unoccupied state.

Theoretical considerations cast doubt on the motivation for PEP violating searches. In 1980, Amado and Primakoff [195] commented on the PEP tests, noting that even if there were some small mixed symmetry component in a primarily antisymmetric wave function, the symmetric hamiltonian would only connect mixed states with other mixed states. The physical effect is the restriction of PEP violating orbital decays in established atomic or nuclear systems even if PEP can be violated through other means.

Despite the theoretical setback, experiments have devised loopholes by introducing new fermions, (i.e. electrons) to further motivate searches for PEP violating decays. The Hamiltonian describing a system and a new electron would not have established symmetry and may relax into a PEP violating state. A summary by Elliott et. al [196] places experiments into three categories, type 1 - 3. Type I experiments involve fermions that have never interacted with other fermions, e.g fermions created just after the Big Bang. Type 2 experiments introduce new fermions into a system, either from β-decay or an electrical current. Type 3 experiments look for stable system transitions, contradictory to Amado and Primakoff.

The search presented here is a type 3 experiment. Taking advantage of the high resolution and low background of the MJD PPC Ge detectors, a search for PEP violating decays from the L-shell to the K-shell in Ge was performed. The energy of the x-ray emitted from the decay is slightly less than the Ge K_α energy due to the additional nuclear screening resulting from the full K-shell. M. Chen computed the energy value of this transition to be 9.543 keV [196]. The resulting cascade of electrons produce additional x-rays that would sum with the PEP violating K_α decay. X-rays produced by Ge transitions in the bulk of the detector have a virtually 100% detection efficiency. The total energy deposited in the

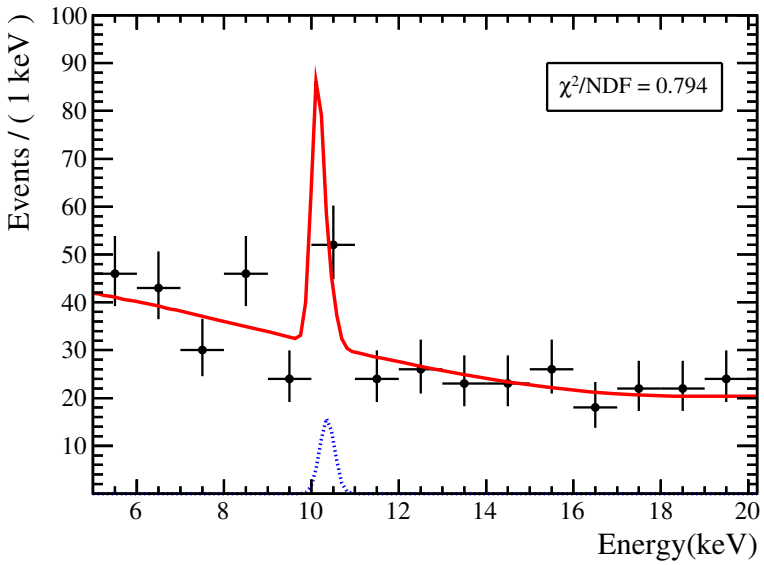

Figure 6.7: Best fit of the background + signal data (red) from 478±6 kg d of DS0 data assuming a signal peak at 10.6 keV (blue). The red curve also includes the tritium spectrum, the 10.36 keV ^{68}K-Shell peak, and the linear background.

detector from a PEP violating decay is then 10.6 keV, manifesting as a shoulder on the ^{68}Ge 10.36 keV cosmogenic peak. Figure 6.7 shows the best fit of a signal at 10.6 keV amongst the background for DS0 data.

Using the likelihood analysis presented in section 6.1.2, assuming a gaussian signal with energy 10.6 keV, a 90% UL was set on the number of signal counts due to a PEP violating decay into the K-shell. A limit of <0.03 counts/kg/d was estimated from the analysis. From this value, a lower limit on the PEP violating decay lifetime was determined, using the atomic mass of 88% enriched Ge, 75.23 g/mol, to be $\tau_{PEP\nu} = 2.0 \times 10^{31}$ s. The average lifetime of the standard Ge K-shell transition is 1.7×10^{-16} s. Using equation 6.23 with $\hbar/\Gamma \sim \tau$, it was found that $\beta^2/2 < 8.5 \times 10^{-48}$. This is roughly 35% better than the limit resulting from a PEP violating electron transition search in iodine by DAMA/LIBRA that determined $\beta^2/2 < 1.28 \times 10^{-47}$ [197].

6.2.5: Electron Decay

Finally, the DS0 data is used to probe the lifetime of the electron. The decay of the electron is a direct test of charge conservation since the electron is the lightest charged particle. Charge conservation corresponds with gauge symmetry in accordance with Noether's theorem. In classical electrodynamics, the vector and scalar potential can be shifted by the gradient or time derivative of an arbitrary scalar field without affecting physical observables of the underlying system. In QFT, this corresponds to an abelian U(1) gauge symmetry with an associated massless boson (i.e. the photon).

There are multiple channels through which the electron may be able to decay. Currently, the best experimental limits come from Borexino [198], which tested the decay mode:

$$e^- \rightarrow \nu + \gamma \ , \tag{6.24}$$

searching for a γ-ray of energy $m_e/2 = 255.5$ keV. Their results provide a lower limit (90% C.L) on the electron lifetime of $>6.6\times10^{28}$ years. It may also be possible for electrons to decay to three neutrinos,

$$e^- \rightarrow \nu\bar{\nu}\nu \ . \tag{6.25}$$

Lifetime limits measured from this process are less stringent. The best limit from this channel (90% C.L) is from P. Belli et. al. [199], with an electron lifetime $> 2.4 \times 10^{24}$ years.

Using the DS0 data, a search for electrons decaying to three neutrinos was performed. The method involves looking for a decay of the electron in the Ge K-shell. The three neutrinos would carry away the 511 keV rest mass energy, but the subsequent cascade of electrons relaxing from higher energy shells would deposit 11.1 keV in the detector. The likelihood analysis was used to determine the 90% U.L on the number of signal events in a gaussian peak centered at 11.1 keV. Less than 0.019 counts/kg/d were determined to be due to electron decay. This translates to a lower limit on the electron lifetime of $> 1.2 \times 10^{22}$ years.

CHAPTER 7: Conclusion

Section 7.1: Overview

The low energy region of the MAJORANA DEMONSTRATOR (MJD) energy spectrum was analyzed in search of rare-event interactions. The low threshold and high resolution of the PPC detectors proved to be a competitive technology for rare events depositing energy in the 5-100 keV range including bosonic dark matter searches, solar axion searches, Pauli Exclusion Principle violation, and electron decay.

The data that was presented represents only 478 kg d of exposure from Module 1 commissioning data. During commissioning, multiple issues were still being addressed, including the energy-scale calibration and electronic noise. Errors in the calibration offset parameter that were negligible at high energy produced significant peak-shifts in the low-energy spectrum. Additionally, the strict protocols that were followed to minimize the enriched detectors' exposure to cosmogenic activation resulted in a lack of peaks below 238 keV to use for calibration. Given the low individual detector count-rate, the spectra from each of the 13 enriched detectors were summed, which required that the calibration procedure was accurate and consistent enough to avoid smearing peaks during spectral summing. Noise issues also plagued the commissioning data. Detectors had to be cut from the analysis, penalizing the overall exposure. Waveform analysis cuts were developed to mitigate the noise issue in the analyzed detectors, but their efficiency dropped below 5 keV, setting a lower bound on the analysis threshold. This threshold is higher than the sub-keV thresholds attained by other PPC Ge detector experiments. Reducing the MJD analysis threshold is a topic of ongoing research by the collaboration.

Despite the setbacks, new limits were reported for bosonic dark matter searches, solar

Table 7.1: Summary of Results. The energy indicates the peak centroid in the signal model with the most stringent limit.

Parameter	Description	Energy	Limit (90% C.L.)
g_{Ae}	Axio-electric coupling constant	11.8 keV	$< 4.5 \times 10^{-13}$
α'/α	Scaled vector electric fine-structure analoge	11.8 keV	$< 9.7 \times 10^{-28}$
$g_{AN}^{\text{eff}} \times g_{Ae}$	Product of the axio-nuclear and axio-electric coupling of solar axions	14.4 keV	$< 3.8 \times 10^{-17}$
$\beta^2/2$	Pauli Exclusion Principle violating decay probability	10.6 keV	$< 8.5 \times 10^{-48}$
τ_{e^-}	Electron lifetime	11.1 keV	$> 1.2 \times 10^{24}$

axion searches, and Pauli Exclusion Principle violation. A factor of two separates the MAJORANA electron decay results from the best limit by P. Belli et. al. [199]. Table 7.1 summarizes the results.

Section 7.2: Outlook

Several improvements to these results are forthcoming. The inclusion of the inner electroformed copper shield has shown a reduced background rate in the low energy region. Preliminary results from data set 1 (DS1) show a roughly factor of 3 decrease in the event rate. Since commissioning, successful detector repairs have been completed, allowing the inclusion of additional detectors in subsequent data sets. Module 2 has since come online, roughly doubling the active mass of the detectors. Lower thresholds will permit additional rare-event searches, including low-mass WIMP searches. The analysis phase of MJD is well underway and many new results are expected to be published by late 2017.

BIBLIOGRAPHY

[1] G. Bertone and D. Hooper, "A History of Dark Matter," *Submitted to: Rev. Mod. Phys.* (2016) , arXiv:1605.04909 [astro-ph.CO].

[2] F. W. Bessel, "On the variations of the proper motions of Procyon and Sirius," *Monthly Notices of the Royal Astronomical Society* **6** (Dec, 1844) 136–141.

[3] J. G. Galle, "Account of the discovery of Le Verrier's planet Neptune, at Berlin, Sept. 23, 1846," *Monthly Notices of the Royal Astronomical Society* **7** (Nov, 1846) 153.

[4] S. Dodelson, "The Real Problem with MOND," *International Journal of Modern Physics D* **20** no. 14, (2011) 2749–2753. http://www.worldscientific.com/doi/abs/10.1142/S0218271811020561.

[5] Kelvin, W. Thomson, and Baron, *Baltimore Lectures on molecular dynamics and the wave theory of light*. Publication agency of the Johns Hopkins university, Baltimore, (1904) 534-535. https://archive.org/details/baltimorelecture00kelviala.

[6] H. Poincare, "The Milky Way and the Theory of Gases," *Popular Astronomy* **14** (Oct, 1906) 475–488.

[7] J. Kapteyn, "First Attempt at a Theory of the Arrangement and Motion of the Sidereal System," *ApJ* **55** (May, 1922) 302.

[8] J. H. Oort, "The force exerted by the stellar system in the direction perpendicular to the galactic plane and some related problems," *Bulletin of the Astronomical Institutes of the Netherlands* **6** (Aug, 1932) 249.

[9] E. Hubble and M. L. Humason, "The Velocity-Distance Relation among Extra-Galactic Nebulae," *Astrophysical Journal* **74** (Jul, 1931) 43.

[10] F. Zwicky, "Die Rotverschiebung von extragalaktischen Nebeln," *Helvetica Physica Acta* **6** (1933) 110–127.

[11] F. Zwicky, "On the Masses of Nebulae and of Clusters of Nebulae," *ApJ* **86** (Oct, 1937) 217.

[12] D. Merritt, "The distribution of dark matter in the coma cluster," *Astrophysical Journal* **313** (Feb, 1987) 121–135.

[13] H. Miyatake, S. More, M. Takada, D. N. Spergel, R. Mandelbaum, E. S. Rykoff, and E. Rozo, "Evidence of Halo Assembly Bias in Massive Clusters," *Phys. Rev. Lett.* **116** (Jan, 2016) 041301. http://link.aps.org/doi/10.1103/PhysRevLett.116.041301.

[14] V. M. Slipher, "The detection of nebular rotation," *Lowell Observatory Bulletin* **2**

(1914) 66.

[15] R. Buta, "The structure and dynamics of ringed galaxies. III - Surface photometry and kinematics of the ringed nonbarred spiral NGC 7531," *Astrophysical Journal Supplement Series* **64** (May, 1987) 1–37.

[16] E. P. Hubble, "Extragalactic nebulae.," *Astrophysical Journal* **64** (Dec, 1926) .

[17] H. W. Babcock, "The rotation of the Andromeda Nebula," *Lick Observatory Bulletin* **19** (1939) 41–51.

[18] H. C. van de Hulst, E. Raimond, and H. van Woerden, "Rotation and density distribution of the Andromeda nebula derived from observations of the 21-cm line," *Bulletin of the Astronomical Institute of the Netherlands* **14** (Nov, 1957) 1.

[19] F. D. Kahn and L. Woltjer, "Intergalactic Matter and the Galaxy.," *Astrophysical Journal* **130** (Nov, 1959) 705.

[20] V. C. Rubin and W. K. Ford, Jr., "Rotation of the Andromeda Nebula from a Spectroscopic Survey of Emission Regions," *Astrophysica Journal* **159** (Feb, 1970) 379.

[21] M. S. Roberts, "A High-Resolution 21-CM Hydrogen-Line Survey of the Andromeda Nebula," *Astrophysical Journal* **144** (May, 1966) 639.

[22] K. G. Begeman, A. H. Broeils, and R. H. Sanders, "Extended rotation curves of spiral galaxies - Dark haloes and modified dynamics," *MNRAS* **249** (1991) 523.

[23] J. F. Navarro, C. S. Frenk, and S. D. M. White, "The Structure of Cold Dark Matter Halos," *Astrophysical Journal* **462** (May, 1996) 563, `astro-ph/9508025`.

[24] A. Einstein, "Lens-Like Action of a Star by the Deviation of Light in the Gravitational Field," *Science* **84** (Dec, 1936) 506–507.

[25] R. Massey, T. Kitching, and J. Richard, "The dark matter of gravitational lensing," *Reports on Progress in Physics* **73** no. 8, (2010) 086901. `http://stacks.iop.org/0034-4885/73/i=8/a=086901`.

[26] Freese, K., "Review of Observational Evidence for Dark Matter in the Universe and in upcoming searches for Dark Stars," *EAS Publications Series* **36** (2009) 113–126. `http://dx.doi.org/10.1051/eas/0936016`.

[27] A. Kravtsov and S. Borgani, "Formation of Galaxy Clusters," *Annual Review of Astronomy and Astrophysics* **50** no. 1, (2012) 353–409, `http://dx.doi.org/10.1146/annurev-astro-081811-125502`. `http://dx.doi.org/10.1146/annurev-astro-081811-125502`.

[28] D. Clowe, M. Bradač, A. H. Gonzalez, M. Markevitch, S. W. Randall, C. Jones, and D. Zaritsky, "A Direct Empirical Proof of the Existence of Dark Matter," *The Astrophysical Journal Letters* **648** no. 2, (2006) L109. http://stacks.iop.org/1538-4357/648/i=2/a=L109.

[29] A. H. G. Peter, M. Rocha, J. S. Bullock, and M. Kaplinghat, "Cosmological simulations with self-interacting dark matter II. Halo shapes versus observations," *Monthly Notices of the Royal Astronomical Society* **430** no. 1, (2013) 105–120, http://mnras.oxfordjournals.org/content/430/1/105.full.pdf+html. http://mnras.oxfordjournals.org/content/430/1/105.abstract.

[30] S. Y. Kim, A. H. G. Peter, and D. Wittman, "In the Wake of Dark Giants: New Signatures of Dark Matter Self Interactions in Equal Mass Mergers of Galaxy Clusters," arXiv:1608.08630 [astro-ph.CO].

[31] S. Dodelson, *Modern cosmology*. Academic Press, An Imprint of Elsevier, San Diego, California, 2003.

[32] A. Liddle, *An introduction to modern cosmology*. Wiley, Chichester, West Sussex, 2015.

[33] **Planck** Collaboration, P. A. R. Ade *et al.*, "Planck 2015 results," *A&A* **594** (2016) A13. http://dx.doi.org/10.1051/0004-6361/201525830.

[34] M. J. Mortonson, D. H. Weinberg, and M. White, "Dark Energy: A Short Review," *ArXiv e-prints* (Dec, 2014) , arXiv:1401.0046 [astro-ph.CO].

[35] D. Samtleben, S. Staggs, and B. Winstein, "The Cosmic Microwave Background for Pedestrians: A Review for Particle and Nuclear Physicists," *Annual Review of Nuclear and Particle Science* **57** no. 1, (2007) 245–283. http://dx.doi.org/10.1146/annurev.nucl.54.070103.181232.

[36] I. A. Strukov, A. A. Brukhanov, D. P. Skulachev, and M. V. Sazhin, "Anisotropy of the microwave background radiation," *Soviet Astronomy Letters* **18** (May, 1992) 153.

[37] I. A. Strukov, A. A. Brukhanov, D. P. Skulachev, and M. V. Sazhin, "The Relikt-1 experiment - New results," *Monthly Notices of the Royal Astronomical Society* **258** (Sep, 1992) 37P–40P.

[38] J. C. Mather *et al.*, "Measurement of the Cosmic Microwave Background spectrum by the COBE FIRAS instrument," *Astrophys. J.* **420** (1994) 439–444.

[39] C. L. Bennett *et al.*, "Preliminary separation of galactic and cosmic microwave emission for the COBE Differential Microwave Radiometer," *Astrophysical Journal, Part2 - Letters* **396** (Sep, 1992) L7–L12.

[40] **WMAP** Collaboration, D. N. Spergel *et al.*, "First year Wilkinson Microwave

Anisotropy Probe (WMAP) observations: Determination of cosmological parameters," *Astrophys. J. Suppl.* **148** (2003) 175–194, arXiv:astro-ph/0302209 [astro-ph].

[41] **Planck** Collaboration, J. M. Lamarre *et al.*, "The Planck High Frequency Instrument, a third generation CMB experiment, and a full sky submillimeter survey," *New Astronomy Reviews* **47** (Dec, 2003) 1017–1024, astro-ph/0308075.

[42] **Planck** Collaboration, Adam, R. *et al.*, "Planck 2015 results," *A&A* **594** (2016) A9. http://dx.doi.org/10.1051/0004-6361/201525936.

[43] D. Scott, D. Contreras, A. Narimani, and Y.-Z. Ma, "The information content of cosmic microwave background anisotropies," *Journal of Cosmology and Astroparticle Physics* **6** (Jun, 2016) 046, arXiv:1603.03550.

[44] W. Hu, "An introduction to the CMB." http://background.uchicago.edu/~whu/beginners/introduction.html, 1996.

[45] R. H. Cyburt, B. D. Fields, K. A. Olive, and T.-H. Yeh, "Big bang nucleosynthesis: Present status," *Rev. Mod. Phys.* **88** (Feb, 2016) 015004. http://link.aps.org/doi/10.1103/RevModPhys.88.015004.

[46] S. Sarkar, "Big bang nucleosynthesis and physics beyond the standard model," *Reports on Progress in Physics* **59** no. 12, (1996) 1493. http://stacks.iop.org/0034-4885/59/i=12/a=001.

[47] M. White, "Big Bang Nucleosynthesis." http://w.astro.berkeley.edu/~mwhite/darkmatter/bbn.html.

[48] **Particle Data Group** Collaboration, K. A. Olive *et al.*, "Review of Particle Physics," *Chin. Phys.* **C38** (2014) 090001.

[49] G. Bertone, D. Hooper, and J. Silk, "Particle dark matter: evidence, candidates and constraints," *Physics Reports* **405** no. 56, (2005) 279 – 390. http://www.sciencedirect.com/science/article/pii/S0370157304003515.

[50] B. Moore and J. Silk, "Dynamical and observable constraints on RAMBOs: Robust associations of massive baryonic objects," *Astrophysical Journal Pt.2 Letters* **442** (Mar, 1995) L5–L8, astro-ph/9407023.

[51] B. Carr, F. Kühnel, and M. Sandstad, "Primordial black holes as dark matter," *Physical Review D* **94** no. 8, (Oct, 2016) 083504, arXiv:1607.06077.

[52] M. Marino, *Dark Matter Physics with P-type Point-contact Germanium Detectors: Extending the Physics Reach of the* Majorana *Experiment*. PhD thesis, University of Washington, 2010.

[53] P. Finnerty, *A Direct Dark Matter Search with the Majorana Low-Background Broad Energy Germanium Detector*. PhD thesis, UNC-Chapel Hill, 2013.

[54] J. D. Lewin and P. F. Smith, "Review of mathematics, numerical factors, and corrections for dark matter experiments based on elastic nuclear recoil," *Astropart. Phys.* **6** (1996) 87–112.

[55] M. Marino, "pyWIMP." `https://github.com/mgmarino/pyWIMP`.

[56] L. Baudis, "WIMP Dark Matter Direct-Detection Searches in Noble Gases," *Phys. Dark Univ.* **4** (2014) 50–59, `arXiv:1408.4371 [astro-ph.IM]`.

[57] S. J. Asztalos, L. J. Rosenberg, K. van Bibber, P. Sikivie, and K. Zioutas, "Searches for Astrophysical and Cosmological Axions," *Annual Review of Nuclear and Particle Science* **56** no. 1, (2006) 293–326. `http://dx.doi.org/10.1146/annurev.nucl.56.080805.140513`.

[58] J. H. Christenson, J. W. Cronin, V. L. Fitch, and R. Turlay, "Evidence for the 2π Decay of the K_2^0 Meson," *Phys. Rev. Lett.* **13** (Jul, 1964) 138–140. `http://link.aps.org/doi/10.1103/PhysRevLett.13.138`.

[59] **BaBar** Collaboration, A. P. Perez, "Recent Results on T and CP Violation at BABAR," in *Proceedings, 21st International Workshop on Deep-Inelastic Scattering and Related Subjects (DIS 2013): Marseilles, France, April 22-26, 2013*. 2013. `arXiv:1307.2759`. `https://inspirehep.net/record/1242125/files/arXiv:1307.2759.pdf`.

[60] R. D. Peccei, "The Strong CP Problem and Axions," in *Axions*, M. Kuster, G. Raffelt, and B. Beltrán, eds., vol. 741 of *Lecture Notes in Physics, Berlin Springer Verlag*, p. 3. 2008. `hep-ph/0607268`.

[61] C. A. Baker, D. D. Doyle, P. Geltenbort, K. Green, M. G. D. van der Grinten, P. G. Harris, P. Iaydjiev, S. N. Ivanov, D. J. R. May, J. M. Pendlebury, J. D. Richardson, D. Shiers, and K. F. Smith, "Improved Experimental Limit on the Electric Dipole Moment of the Neutron," *Phys. Rev. Lett.* **97** (Sep, 2006) 131801. `http://link.aps.org/doi/10.1103/PhysRevLett.97.131801`.

[62] R. D. Peccei and H. R. Quinn, "Constraints imposed by CP conservation in the presence of pseudoparticles," *Phys. Rev. D* **16** (Sep, 1977) 1791–1797.

[63] R. D. Peccei and H. R. Quinn, "CP conservation in the presence of pseudoparticles," *Physical Review Letters* **38** (Jun, 1977) 1440–1443.

[64] D. A. Dicus, E. W. Kolb, V. L. Teplitz, and R. V. Wagoner, "Astrophysical bounds on the masses of axions and Higgs particles," *Phys. Rev. D* **18** (Sep, 1978) 1829–1834. `http://link.aps.org/doi/10.1103/PhysRevD.18.1829`.

[65] P. Sikivie, "Experimental Tests of the "Invisible" Axion," *Phys. Rev. Lett.* **51** (Oct, 1983) 1415–1417. http://link.aps.org/doi/10.1103/PhysRevLett.51.1415.

[66] S. J. Asztalos, G. Carosi, C. Hagmann, D. Kinion, K. van Bibber, M. Hotz, L. J. Rosenberg, G. Rybka, J. Hoskins, J. Hwang, P. Sikivie, D. B. Tanner, R. Bradley, and J. Clarke, "SQUID-Based Microwave Cavity Search for Dark-Matter Axions," *Phys. Rev. Lett.* **104** (Jan, 2010) 041301. http://link.aps.org/doi/10.1103/PhysRevLett.104.041301.

[67] **OSQAR** Collaboration, P. Pugnat, L. Duvillaret, R. Jost, G. Vitrant, D. Romanini, A. Siemko, R. Ballou, B. Barbara, M. Finger, M. Finger, J. Hošek, M. Král, K. A. Meissner, M. Šulc, and J. Zicha, "Results from the OSQAR photon-regeneration experiment: No light shining through a wall," *Phys. Rev. D* **78** (Nov, 2008) 092003. http://link.aps.org/doi/10.1103/PhysRevD.78.092003.

[68] **IAXO, CAST** Collaboration, T. Dafni and F. J. Iguaz, "Axion helioscopes update: the status of CAST & IAXO," *PoS* **TIPP2014** (2014) 130, arXiv:1501.01456 [physics.ins-det].

[69] **Particle Data Group** Collaboration, N. K. *et al.*, "Axions and Other Similar Particles," *JPG* **37** (2010) .

[70] T. W. Donnelly, S. J. Freedman, R. S. Lytel, R. D. Peccei, and M. Schwartz, "Do axions exist?," *Phys. Rev. D* **18** (Sep, 1978) 1607–1620. http://link.aps.org/doi/10.1103/PhysRevD.18.1607.

[71] S. Barshay, H. Faissner, R. Rodenberg, and H. De Witt, "Coherent Conversion of Very Light Pseudoscalar Bosons," *Phys. Rev. Lett.* **46** (1981) 1361–1364.

[72] A. Zhitnitsky, "On Possible Suppression of the Axion Hadron Interactions," *Sov. J. Nucl. Phys* **31** no. 260, (1980) .

[73] M. Dine, W. Fischler, and M. Srednicki, "A simple solution to the strong CP problem with a harmless axion," *Physics Letters B* **104** no. 3, (1981) 199 – 202. http://www.sciencedirect.com/science/article/pii/0370269381905906.

[74] J. E. Kim, "Weak-Interaction Singlet and Strong CP Invariance," *Phys. Rev. Lett.* **43** (Jul, 1979) 103–107. http://link.aps.org/doi/10.1103/PhysRevLett.43.103.

[75] M. Shifman, A. Vainshtein, and V. Zakharov, "Can confinement ensure natural CP invariance of strong interactions?," *Nuclear Physics B* **166** no. 3, (1980) 493 – 506. http://www.sciencedirect.com/science/article/pii/0550321380902096.

[76] M. Pospelov, A. Ritz, and M. Voloshin, "Bosonic super-WIMPs as keV-scale dark matter," *Phys. Rev. D* **78** (Dec, 2008) 115012. http://link.aps.org/doi/10.1103/PhysRevD.78.115012.

[77] J. Jaeckel, J. Redondo, and A. Ringwald, "Signatures of a Hidden Cosmic Microwave Background," *Phys. Rev. Lett.* **101** (Sep, 2008) 131801. http://link.aps.org/doi/10.1103/PhysRevLett.101.131801.

[78] **EDELWEISS** Collaboration, E. Armengaud *et al.*, "Axion searches with the EDELWEISS-II experiment," *Journal of Cosmology and Astroparticle Physics* **2013** no. 11, (2013) 067. http://stacks.iop.org/1475-7516/2013/i=11/a=067.

[79] **XMASS** Collaboration, K. Abe *et al.*, "Search for Bosonic Superweakly Interacting Massive Dark Matter Particles with the XMASS-I Detector," *Phys. Rev. Lett.* **113** (Sep, 2014) 121301. http://link.aps.org/doi/10.1103/PhysRevLett.113.121301.

[80] H. Becquerel, "Sur les radiations émises par phosphorescence," *Comptus Rendus* **122** (1896) 420–421.

[81] G. Bertolini and A. Coche, *Semiconductor detectors, ed.* Elsevier-North Holland, Amsterdam, 1968.

[82] G. Knoll, *Radiation detection and measurement.* John Wiley, Hoboken, N.J, 2010.

[83] G. Gilmore, *Practical Gamma-ray Spectroscopy.* Wiley, 2008.

[84] I. Akkurt, K. Gunoglu, and S. S. Arda, "Detection Efficiency of NaI(Tl) Detector in 5111332keV Energy Range," *Science and Technology of Nuclear Installations* **2014** (2014) 1–5.

[85] Canberra, "Germanium Detectors." http://www.canberra.com/products/detectors/pdf/Germanium-Det-SS-C39606.pdf, 2014.

[86] C. R. Nave, "HyperPhysics." http://hyperphysics.phy-astr.gsu.edu/hbase/hframe.html, 2012.

[87] ORTEC, "ORTEC." http://www.ortec-online.com/aboutus/index.aspx, 2016.

[88] B. Whipple, "Unusual Metals," *The Michigan Technic* **79** no. 6, (March, 1961) 13 – 15.

[89] P. Tomaszewski, *Jan Czochralski i jego metoda = Jan Czochralski and his method.* Atut Instytut Niskich Temperatur i Bada Strukturalnych PAN Urzd Gminy i Miasta, Wrocaw Kcynia, 2003.

[90] Canberra, "Broad Energy Germanium Detectors (BEGe)." http://www.canberra.com/products/detectors/pdf/BEGe-SS-C40426.pdf, 2013.

[91] D. Allard *et al.*, "IEEE Standard Test Procedures for Germanium Gamma-Ray

Detectors," *IEEE Std 325-1996* (October, 1996) 1–64.

[92] P. Barbeau, *Neutrino and Astroparticle Physics with P-Type Point Contact High Purity Germanium Detectors*. PhD thesis, University of Chicago, 2009.

[93] G. K. Giovanetti, *P-Type Point Contact Germanium Detectors and their Application In Rare-Event Searches*. PhD thesis, UNC-Chapel Hill, 2015.

[94] G. Bertucci and A. Pullia, "A method for the determination of the noise parameters in preamplifying systems for semiconductor radiation detectors," *Rev. Sci. Instrum.* **64** (September, 1993) 3294–3298.

[95] E. Gatti, P. Manfredi, M. Sampietro, and V. Speziali, "Suboptimal filtering of 1/-noise in detector charge measurements," *Nuclear Instruments and Methods in Physics Research Section A: Accelerators, Spectrometers, Detectors and Associated Equipment* **297** no. 3, (1990) 467 – 478. http://www.sciencedirect.com/science/article/pii/0168900290913315.

[96] P. Chu, "Detailed Information of Energy Estimation on the Module 1 of the Majorana Demonstrator," tech. rep., Los Alamos National Laboratory, 2016.

[97] A. Poon, "Detectors." Presentation, Aug, 2012. Status update of MJ research PPC detectors at LBNL.

[98] V. Radeka, "Low-Noise Techniques in Detectors," *Annual Review of Nuclear and Particle Science* **38** no. 1, (1988) 217–277, http://dx.doi.org/10.1146/annurev.ns.38.120188.001245.

[99] P. Luke, F. Goulding, N. Madden, and R. H. Pehl, "Low Capacitance Large Volume Shaped-Field Germanium Detector," *IEEE Transactions on Nuclear Science* **36** no. 1, (February, 1999) 926–930.

[100] P. J. Statham, "Pile-up rejection: Limitations and corrections for residual errors in energy-dispersive spectrometers," *X-Ray Spectrometry* **6** no. 2, (1977) 94–103. http://dx.doi.org/10.1002/xrs.1300060211.

[101] Canberra, "Standard Electrod Coaxial Ge Detectors (SEGe)." http://www.canberra.com/products/detectors/pdf/SEGe-detectors-C40021.pdf, 2013.

[102] H. R. Bilger, "Fano Factor in Germanium at 77 K," *Phys. Rev.* **163** (Nov, 1967) 238–253. http://link.aps.org/doi/10.1103/PhysRev.163.238.

[103] N. Strokan, V. Ajdacic, and B. Lalovic, "Measurements of the Fano factor in germanium," *Nuclear Instruments and Methods* **94** no. 1, (1971) 147 – 149. http://www.sciencedirect.com/science/article/pii/0029554X71903521.

[104] M. Agostini *et al.*, "Pulse shape discrimination for Gerda Phase I data," *European Physical Journal C* **73** (Oct, 2013) 2583, arXiv:1307.2610 [physics.ins-det].

[105] W. Shockley, "Currents to Conductors Induced by a Moving Point Charge," *Journal of Applied Physics* **9** (Oct, 1938) 635–636.

[106] S. Ramo, "Currents Induced by Electron Motion," *Proceedings of the IRE* **27** no. 9, (Sept, 1939) 584–585.

[107] D. C. Radford *et al.*, "RadWare." http://radware.phy.ornl.gov/, 2014.

[108] **CoGeNT Collaboration** Collaboration, C. E. Aalseth and others., "Results from a Search for Light-Mass Dark Matter with a p-Type Point Contact Germanium Detector," *Phys. Rev. Lett.* **106** (Mar, 2011) 131301. http://link.aps.org/doi/10.1103/PhysRevLett.106.131301.

[109] **MAJORANA** Collaboration, E. Aguayo *et al.*, "Characteristics of Signals Originating Near the Lithium-Diffused N+ Contact of High Purity Germanium P-Type Point Contact Detectors," *ArXiv e-prints* (Jul, 2012) , arXiv:1207.6716 [physics.ins-det].

[110] N. Abgrall *et al.*, "The MAJORANA DEMONSTRATOR Neutrinoless Double-Beta Decay Experiment," *AHEP* **2014** (2014) 18.

[111] Sanford Lab, "Sanford Underground Research Facility." http://www.sanfordlab.org, 2017.

[112] S. R. Elliott, A. A. Hahn, and M. K. Moe, "Direct evidence for two-neutrino double-beta decay in ^{82}Se," *Phys. Rev. Lett.* **59** (Nov, 1987) 2020–2023. http://link.aps.org/doi/10.1103/PhysRevLett.59.2020.

[113] L. Ekstrom and R. Firestone, "WWW Table of Radioactive Isotopes." http://ie.lbl.gov/toi/index.htm.

[114] **EXO** Collaboration, J. B. Albert *et al.*, "Improved measurement of the $2\nu\beta\beta$ half-life of ^{136}Xe with the EXO-200 detector," *Phys. Rev. C* **89** (Jan, 2014) 015502. http://link.aps.org/doi/10.1103/PhysRevC.89.015502.

[115] **GERDA** Collaboration, M. Agostini *et al.*, "Measurement of the half-life of the two-neutrino double beta decay of 76Ge with the GERDA experiment," *J. Phys. G: Nucl. Part. Phys.* **40** no. 3, (2013) 035110.

[116] **NEMO** Collaboration, R. Arnold *et al.*, "Measurement of the $\beta\beta$ Decay Half-Life of ^{130}Te with the NEMO-3 Detector," *Phys. Rev. Lett.* **107** (Aug, 2011) 062504. http://link.aps.org/doi/10.1103/PhysRevLett.107.062504.

[117] A. Barabash and V. Brudanin, "Investigation of double-beta decay with the NEMO-3

detector," *Physics of Atomic Nuclei* **74** no. 2, (2011) 312–317. http://dx.doi.org/10.1134/S1063778811020062.

[118] **NEMO** Collaboration, J. Argyriades *et al.*, "Measurement of the two neutrino double beta decay half-life of Zr-96 with the NEMO-3 detector," *Nuclear Physics A* **847** no. 3–4, (2010) 168 – 179. http://www.sciencedirect.com/science/article/pii/S0375947410006238.

[119] **NEMO** Collaboration, J. Argyriades *et al.*, "Measurement of the double-β decay half-life of ^{150}Nd and search for neutrinoless decay modes with the NEMO-3 detector," *Phys. Rev. C* **80** (Sep, 2009) 032501. http://link.aps.org/doi/10.1103/PhysRevC.80.032501.

[120] **NEMO** Collaboration, R. Arnold *et al.*, "First Results of the Search for Neutrinoless Double-Beta Decay with the NEMO 3 Detector," *Phys. Rev. Lett.* **95** (Oct, 2005) 182302. http://link.aps.org/doi/10.1103/PhysRevLett.95.182302.

[121] R. Henning, "Current status of neutrinoless double-beta decay searches," *Reviews in Physics* **1** (2016) 29 – 35. http://www.sciencedirect.com/science/article/pii/S2405428316000034.

[122] **Particle Data Group** Collaboration, C. Patrignani *et al.*, "Review of Particle Physics," *Chin. Phys.* **C40** no. 10, (2016) 100001.

[123] F. T. Avignone, S. R. Elliott, and J. Engel, "Double beta decay, Majorana neutrinos, and neutrino mass," *Rev. Mod. Phys.* **80** (Apr, 2008) 481–516. http://link.aps.org/doi/10.1103/RevModPhys.80.481.

[124] J. Schechter and J. W. F. Valle, "Neutrinoless double-β decay in SU(2)xU(1) theories," *Phys. Rev. D* **25** (Jun, 1982) 2951–2954. http://link.aps.org/doi/10.1103/PhysRevD.25.2951.

[125] E. Paschos, "Leptogenesis with Majorana neutrinos," *Nuclear Physics B - Proceedings Supplements* **112** no. 1, (2002) 36 – 41. http://www.sciencedirect.com/science/article/pii/S0920563202017589.

[126] B. Kayser, "Majorana Masses, the See-Saw Mechanism, and Leptogenesis." Presentation, Nov, 2012. http://nucla.physics.ucla.edu/sites/default/files/Kayser_UCLA1211.pdf.

[127] H. V. Klapdor-Kleingrothaus, H. Päs, and A. Y. Smirnov, "Neutrino mass spectrum and neutrinoless double beta decay," *Phys. Rev. D* **63** (Mar, 2001) 073005. http://link.aps.org/doi/10.1103/PhysRevD.63.073005.

[128] B. A. Brown, D. L. Fang, and M. Horoi, "Evaluation of the theoretical nuclear matrix elements for $\beta\beta$ decay of ^{76}Ge," *Phys. Rev. C* **92** (Oct, 2015) 041301.

https://link.aps.org/doi/10.1103/PhysRevC.92.041301.

[129] E. Caurier, G. Martínez-Pinedo, F. Nowacki, A. Poves, and A. P. Zuker, "The shell model as a unified view of nuclear structure," *Rev. Mod. Phys.* **77** (Jun, 2005) 427–488. https://link.aps.org/doi/10.1103/RevModPhys.77.427.

[130] J. P. Elliott, "The interacting boson model of nuclear structure," *Reports on Progress in Physics* **48** no. 2, (1985) 171. http://stacks.iop.org/0034-4885/48/i=2/a=001.

[131] T. R. Rodríguez and G. Martínez-Pinedo, "Energy Density Functional Study of Nuclear Matrix Elements for Neutrinoless $\beta\beta$ Decay," *Phys. Rev. Lett.* **105** (Dec, 2010) 252503. https://link.aps.org/doi/10.1103/PhysRevLett.105.252503.

[132] **GERDA** Collaboration, K. o. Ackermann, "The Gerda experiment for the search of $0\nu\beta\beta$ decay in ^{76}Ge," *The European Physical Journal C* **73** no. 3, (2013) . http://dx.doi.org/10.1140/epjc/s10052-013-2330-0.

[133] **LUX** Collaboration, D. S. Akerib *et al.*, "First Results from the LUX Dark Matter Experiment at the Sanford Underground Research Facility," *Phys. Rev. Lett.* **112** (Mar, 2014) 091303. http://link.aps.org/doi/10.1103/PhysRevLett.112.091303.

[134] E. Paschos and K. Zioutas, "A proposal for solar axion detection via Bragg scattering," *Physics Letters B* **323** (1994) 367–372.

[135] N. Abgrall *et al.*, "Muon Flux Measurements at the Davis Campus of the Sanford Underground Research Facility with the Majorana Demonstrator Veto System," *ArXiv e-prints* (Feb, 2016) , arXiv:1602.07742 [nucl-ex].

[136] B. T. Cleveland, T. Daily, J. Raymond Davis, J. R. Distel, K. Lande, C. K. Lee, P. S. Wildenhain, and J. Ullman, "Measurement of the Solar Electron Neutrino Flux with the Homestake Chlorine Detector," *The Astrophysical Journal* **496** no. 1, (1998) 505. http://stacks.iop.org/0004-637X/496/i=1/a=505.

[137] **LZ** Collaboration, D. S. Akerib *et al.*, "LUX-ZEPLIN (LZ) Conceptual Design Report," *ArXiv e-prints* (Sep, 2015) , arXiv:1509.02910 [physics.ins-det].

[138] R. Acciarri *et al.*, "Long-Baseline Neutrino Facility (LBNF) and Deep Underground Neutrino Experiment (DUNE) Conceptual Design Report Volume 1: The LBNF and DUNE Projects," *ArXiv e-prints* (Jan, 2016) , arXiv:1601.05471 [physics.ins-det].

[139] N. R. Overman *et al.*, "MAJORANA Electroformed Copper Analysis," tech. rep., PNNL, 2012.

[140] **MAJORANA** Collaboration, N. Abgrall *et al.*, "The Majorana Parts Tracking

Database," *Nucl. Instrum. Meth. in Physics* **779** (2015) 52 – 62.

[141] Axon-Cable, "Pico Coax Miniature Cables." http://www.axon-cable.com/publications/PICOCOAX-GB.pdf, 2016.

[142] E. Aguayo, M. Busch, R. Daniels, J. Fast, M. Green, and D. Reid, "The design of an ultra-low background thermosyphon for the Majorana Demonstrator," *Nuclear Instruments and Methods in Physics Research Section A: Accelerators, Spectrometers, Detectors and Associated Equipment* **709** (2013) 17 – 21. http://www.sciencedirect.com/science/article/pii/S0168900213000557.

[143] H. Systems, "Hovair's Air Handling Systems." http://hovair.com/, 2017.

[144] C. Wiseman, "Performance of the Majorana Demonstrator Muon Veto System [abstract]," in *Fall Meeting of the APS Division of Nuclear Physics*. 2015.

[145] ISOFLEX, "ISOFLEX: Isotopes for Science, Medicine, and Industry." http://www.isoflex.com/, 2017.

[146] N. Abgrall *et al.*, "The Majorana Low-noise Low-background Front-end Electronics," *Physics Procedia* **61** (2015) 654 – 657. http://www.sciencedirect.com/science/article/pii/S1875389214006798.

[147] M. Howe, "Object-oriented Real-time Control and Acquisition (ORCA)." http://orca.physics.unc.edu/.

[148] M. Howe, M. Marino, and J. Wilkerson, "Integration of embedded single board computers into an object-oriented software bus DAQ application," in *Nuclear Science Symposium Conference Record, 2008. NSS '08. IEEE*, pp. 3562–3567. Oct, 2008.

[149] M. Howe *et al.*, "Sudbury Neutrino Observatory neutral current detector acquisition software overview," in *Nuclear Science Symposium Conference Record, 2003 IEEE*, vol. 1, pp. 169–173 Vol.1. Oct, 2003.

[150] M. Schumaker *et al.*, "Data acquisition for the Helium and Lead Observatory," in *Nuclear Science Symposium Conference Record (NSS/MIC), 2010 IEEE*, pp. 1860–1865. Oct, 2010.

[151] D. Phillips, II, "An Overview of the Data Acquisition System in the KATRIN Experiment," in *APS April Meeting Abstracts*. Feb., 2010.

[152] D. Doering *et al.*, "GRETINA Digitizer Specification," tech. rep., LBNL, 2008. http://orca.physics.unc.edu/VME/Gretina4M_files/Gretina4Manual.pdf.

[153] VITA, "VMEbus Technology FAQ." http://www.vita.com/page-1855175, 2017.

[154] CAEN, "CAEN." http://www.caen.it/, 2017.

[155] NERSC, "PDSF." http://www.nersc.gov/users/computational-systems/pdsf/, 2016.

[156] M. Boswell *et al.*, "MaGe-a Geant4-based Monte Carlo Application Framework for Low-background Germanium Experiments," *IEEE Trans. Nucl. Sci.* **58** (2011) 1212–1220, arXiv:1011.3827 [nucl-ex].

[157] S. Agostinelli *et al.*, "Geant4—a simulation toolkit," *Nuclear Instruments and Methods in Physics Research Section A: Accelerators, Spectrometers, Detectors and Associated Equipment* **506** no. 3, (2003) 250 – 303. http://www.sciencedirect.com/science/article/pii/S0168900203013688.

[158] J. Allison *et al.*, "Geant4 developments and applications," *Nuclear Science, IEEE Transactions on* **53** no. 1, (Feb, 2006) 270–278.

[159] C. Cuesta, "Run Selection and Data Cleaning of P3JDY," tech. rep., University of Washington, 2016.

[160] S. Meijer, "DS0 Livetime estimation summary," tech. rep., University of North Carolina at Chapel Hill, 2016.

[161] Starrett, "Starrett Precision Measuring Tools." http://www.starrett.com/metrology/metrology-products/precision-measuring-tools, 2015. Online; accessed 11 October 2016.

[162] M. Buuck, "Calculating the Active Mass of the MJ M1 Detectors," tech. rep., University of Washington, 2016.

[163] R. Brun and F. Rademakers, "ROOT: An object oriented data analysis framework," *Nucl. Instrum. Meth.* **A389** (1997) 81–86.

[164] M. Agostini *et al.*, "The MGDO software library for data analysis in Ge neutrinoless double-beta decay experiments," *J. Phys. Conf. Ser.* **375** (2012) 042027, arXiv:1111.7260 [physics.data-an].

[165] V. T. Jordanov and G. F. Knoll, "Digital synthesis of pulse shapes in real time for high resolution radiation spectroscopy," *Nuclear Instruments and Methods in Physics Research Section A: Accelerators, Spectrometers, Detectors and Associated Equipment* **345** no. 2, (1994) 337 – 345. http://www.sciencedirect.com/science/article/pii/0168900294910111.

[166] NNDC, "National Nuclear Data Center Chart of Nuclides." http://www.nndc.bnl.gov/chart/, 2016. Online; accessed 12 October 2016.

[167] S. Mertens, "Gretina Non-Linearites," tech. rep., Lawrence Berkeley National Lab, 2015.

[168] A. Haar, "Zur Theorie der orthogonalen Funktionensysteme," *Mathematische Annalen* **69** no. 3, (1910) 331–371. http://dx.doi.org/10.1007/BF01456326.

[169] C. Cuesta, "PSA A/E optimization," tech. rep., University of Washington, 2014. http://mjwiki.npl.washington.edu/pub/Majorana/AnalysisReports/PSA_141208.pdf.

[170] Agilent, "Agilent 33220 20 MHz Waveform Generator," tech. rep., Agilent Technologies, Inc., 2007. http://cp.literature.agilent.com/litweb/pdf/33220-90002.pdf.

[171] F. James, *Statistical Methods in Experimental Physics*. World Scientific Publishing, 2006. https://books.google.com/books?id=S8N_QgAACAAJ.

[172] W. A. Rolke, A. M. Lpez, and J. Conrad, "Limits and confidence intervals in the presence of nuisance parameters," *Nuclear Instruments and Methods in Physics Research Section A: Accelerators, Spectrometers, Detectors and Associated Equipment* **551** no. 23, (2005) 493 – 503. http://www.sciencedirect.com/science/article/pii/S016890020501291X.

[173] S. S. Wilks, "The Large-Sample Distribution of the Likelihood Ratio for Testing Composite Hypotheses," *Ann. Math. Statist.* **9** no. 1, (03, 1938) 60–62. http://dx.doi.org/10.1214/aoms/1177732360.

[174] W. Verkerke and D. P. Kirkby, "The RooFit toolkit for data modeling," *eConf* **C0303241** (2003) MOLT007, arXiv:physics/0306116 [physics].

[175] L. Moneta *et al.*, "MINUT." http://seal.web.cern.ch/seal/snapshot/work-packages/mathlibs/minuit/.

[176] "TMinuit Class Reference." https://root.cern.ch/doc/master/classTMinuit.html.

[177] **ATLAS** Collaboration, G. Aad *et al.*, "Measurements of Higgs boson production and couplings in diboson final states with the ATLAS detector at the LHC," *Phys. Lett.* **B726** (2013) 88–119, arXiv:1307.1427 [hep-ex]. [Erratum: Phys. Lett.B734,406(2014)].

[178] **EDELWEISS** Collaboration, L. Hehn *et al.*, "Improved EDELWEISS-III sensitivity for low-mass WIMPs using a profile likelihood approach," *Eur. Phys. J.* **C76** no. 10, (2016) 548, arXiv:1607.03367 [astro-ph.CO].

[179] **Fermi-LAT** Collaboration, A. Albert, G. A. Gomez-Vargas, M. Grefe, C. Munoz, C. Weniger, E. D. Bloom, E. Charles, M. N. Mazziotta, and A. Morselli, "Search for 100 MeV to 10 GeV γ-ray lines in the Fermi-LAT data and implications for gravitino dark matter in $\mu\nu$SSM," *JCAP* **1410** no. 10, (2014) 023, arXiv:1406.3430

[astro-ph.HE].

[180] S. Mertens, T. Lasserre, S. Groh, G. Drexlin, F. Glck, A. Huber, A. Poon, M. Steidl, N. Steinbrink, and C. Weinheimer, "Sensitivity of next-generation tritium beta-decay experiments for keV-scale sterile neutrinos," *Journal of Cosmology and Astroparticle Physics* **2015** no. 02, (2015) 020. http://stacks.iop.org/1475-7516/2015/i=02/a=020.

[181] B. White. Private communication.

[182] C. Lanczos, "A Precision Approximation of the Gamma Function," *Journal of the Society for Industrial and Applied Mathematics: Series B, Numerical Analysis* **1** (1964) 86–96. http://www.jstor.org/stable/2949767.

[183] F. Alessandria *et al.*, "Search for 14.4 keV solar axions from M1 transition of Fe-57 with CUORE crystals," *JCAP* **05** (2013) 007, arXiv:1209.2800.

[184] NIST, "XCOM." http://physics.nist.gov/PhysRefData/Xcom/html/xcom1.html, 2013.

[185] E. Aprile *et al.*, "First axion results from the XENON100 experiment," *Phys. Rev. D* **90** (Sep, 2014) 062009. http://link.aps.org/doi/10.1103/PhysRevD.90.062009.

[186] E. Aprile *et al.*, "Erratum: First axion results from the XENON100 experiment [Phys. Rev. D 90, 062009 (2014)]," *Phys. Rev. D* **95** (Jan, 2017) 029904. http://link.aps.org/doi/10.1103/PhysRevD.95.029904.

[187] S. K. Liu *et al.*, "Constraints on Axion couplings from the CDEX-1 experiment at the China Jinping Underground Laboratory," arXiv:1610.07521 [hep-ex].

[188] "IDM2016 Identification of Dark Matter 2016." https://idm2016.shef.ac.uk/, 2016. last checked 10/10/16.

[189] H. An, M. Pospelov, J. Pradler, and A. Ritz, "Direct detection constraints on dark photon dark matter," *Physics Letters B* **747** (2015) 331 – 338. http://www.sciencedirect.com/science/article/pii/S0370269315004402.

[190] S. Moriyama, "Proposal to search for a monochromatic component of solar axions using ^{57}Fe," *Nuclear Physics B - Proceedings Supplements* **72** (1999) 183 – 186. http://www.sciencedirect.com/science/article/pii/S0920563298005222.

[191] D. B. Kaplan, "Opening the axion window," *Nuclear Physics B* **260** no. 1, (1985) 215 – 226. http://www.sciencedirect.com/science/article/pii/0550321385903190.

[192] F. T. Avignone III, C. Baktash, W. C. Barker, F. P. Calaprice, R. W. Dunford, W. C. Haxton, D. Kahana, R. T. Kouzes, H. S. Miley, and D. M. Moltz, "Search for axions from the 1115-keV transition of ^{65}Cu," *Phys. Rev. D* **37** (Feb, 1988) 618–630.

http://link.aps.org/doi/10.1103/PhysRevD.37.618.

[193] W. Pauli, "Exclusion Principle and Quantum Mechanics." https://www.nobelprize.org/nobel_prizes/physics/laureates/1945/pauli-lecture.pdf, Dec, 1946.

[194] O. W. Greenberg and R. C. Hilborn, "Quon Statistics for Composite Systems and a Limit on the Violation of the Pauli Principle for Nucleons and Quarks," *Phys. Rev. Lett.* **83** (Nov, 1999) 4460–4463. http://link.aps.org/doi/10.1103/PhysRevLett.83.4460.

[195] R. D. Amado and H. Primakoff, "Comments on testing the Pauli principle," *Phys. Rev. C* **22** (Sep, 1980) 1338–1340. http://link.aps.org/doi/10.1103/PhysRevC.22.1338.

[196] S. R. Elliott, B. H. LaRoque, V. M. Gehman, M. F. Kidd, and M. Chen, "An Improved Limit on Pauli-Exclusion-Principle Forbidden Atomic Transitions," *Foundations of Physics* **42** no. 8, (2012) 1015–1030. http://dx.doi.org/10.1007/s10701-012-9643-y.

[197] R. Bernabei *et al.*, "New search for processes violating the Pauli exclusion principle in sodium and in iodine," *Eur. Phys. J. C* **62** no. 2, (2009) 327–332. http://dx.doi.org/10.1140/epjc/s10052-009-1068-1.

[198] **Borexino** Collaboration, M. Agostini *et al.*, "Test of Electric Charge Conservation with Borexino," *Phys. Rev. Lett.* **115** (Dec, 2015) 231802. http://link.aps.org/doi/10.1103/PhysRevLett.115.231802.

[199] P. Belli *et al.*, "New experimental limit on the electron stability and non-paulian transitions in Iodine atoms," *Phys. Lett. B* **460** (1999) 236.